ABSTRACT

Title of Dissertation: Quad Tilt Rotor Simulations in Helicopter Mode using Computational Fluid Dynamics

Vinit Gupta, Doctor of Philosophy, 2005

Dissertation directed by: Associate Professor James D. Baeder
Department of Aerospace Engineering

The flow field around a simplified Quad Tilt Rotor (QTR) vehicle is simulated using computational fluid dynamics (CFD) for various low speed flight conditions in helicopter mode. A time-averaged rotor model is utilized, where the velocity field computed by CFD is coupled to blade element theory and a trim model to provide an equivalent time-averaged body force term in the compressible Navier-Stokes equations, instead of moving overset meshes; reducing the computational time while capturing the essential physics. Overset meshes are used to model the complicated geometry of the simplified aircraft fuselage and wings in order to ensure good resolution of viscous effects. The solution of the compressible Navier-Stokes equations are suitably modified using low Mach number preconditioning to properly scale the dissipation and enhance convergence. This approach is validated for the current work by comparison with experimental data for the downwash velocity underneath an isolated tilt rotor system as well as for the pressure distribution resulting on the surface of a single wing placed underneath such a tilt rotor system. A total of 8 grids with approximately 5.2 million grid points is then employed to simulate half of a simplified QTR geometry for a range of flight conditions. A high download (9% of thrust) is obtained in hover, as expected, when the

QTR operates Out of Ground Effect (OGE), primarily from a strong download on the front and rear wings. A detailed analysis of the calculated flow field, along with chordwise pressure distributions and spanwise loadings on the wings, is performed to explain the observed decay in download on the vehicle with an increase in the forward flight speed. The high download obtained OGE in hover, becomes a strong upload (9% of thrust) when the vehicle operates In Ground Effect (IGE) with the wheels placed on the ground; primarily from a strong upload on the fuselage and inner portion of the rear wing. Upload observed IGE in hover gradually fades away with an increases in forward flight. An increase in forward flight speed eventually results in the flow along the ground unable to travel far upstream; the simulation shows the expected horseshoe shape of the wake near the ground. The simulations suggest that the uploads obtained IGE persist for high enough forward flight speed such that a significant increase in payload should be feasible for rolling takeoffs.

Quad Tilt Rotor Simulations in Helicopter Mode using Computational Fluid Dynamics

by

Vinit Gupta

Dissertation submitted to the Faculty of the Graduate School of the
University of Maryland, College Park in partial fulfillment
of the requirements for the degree of
Doctor of Philosophy
2005

Advisory Committee:

Associate Professor James D. Baeder, Chairman/Advisor
Professor I. Chopra
Assistant Professor C. Cadou
Professor F. Schmitz
Professor J. Wallace

TABLE OF CONTENTS

LIST OF TABLES

LIST OF FIGURES

List of Symbols

Re	Reynolds Number
c	Chord
M_∞	Free-stream Mach number
U_∞	Free-stream velocity
M_{tip}	Tip mach number of the rotor blade
U_{tip}	Tip speed of the rotor blade
Ω	Angular velocity of blade rotation
α	Angle of attack
R	Spanwise distance from axis of rotation to blade tip
N_b	Number of blades
V_i	Induced Velocity
θ_o	Collective pitch of blade
θ_{1c}	Longitudinal cyclic pitch of blade
θ_{1s}	Lateral cyclic pitch of blade
C_L	Lift coefficient
C_D	Drag coefficient
C_T	Thrust coefficient
x, y, z	Cartesian coordinates
ξ, η, ζ	Transformed coordinates
u, v, w	Velocity components in the Cartesian directions
f_x, f_y, f_z	Body forces in the Cartesian directions
ψ	Azimuthal angle ($\psi = 0$) at the trailing edge of wing tip
ρ	Density
β	Preconditioning parameter
λ	Eigenvalues

M	Mach number
P	Preconditioning matrix
H	Stagnation enthalpy
e	Internal energy
J	Jacobian of cell volume
ν	Kinematic viscosity
ν_t	Turbulent eddy viscosity
$\bar{\nu}$	Working variable in Spalart Allmaras turbulence model
τ_w	Wall shear stress
p	Pressure
T	Rotor Thrust
A	Area of rotor disk
p_∞	Ambient Pressure
C_p	$= \frac{p-p_\infty}{\frac{1}{2}\rho_\infty U_\infty^2}$ Pressure coefficient
C_{pDL}	$= \frac{p-p_\infty}{T/A}$ Pressure coefficient with respect to disk loading

Chapter 1

Introduction

The ability of tilt rotor vehicles to vertically take off like a helicopter and then propel forward at high speeds like an airplane provides a promising unique capability. This transition from helicopter mode to propeller mode involves a change in orientation of the rotor systems, mounted at the wing tips, from a horizontal plane to a vertical plane. This process of transition for the V-22 aircraft is shown in Figure 1.1. As a result, the rotors which predominantly provide the lifting force in helicopter mode gradually transition to provide aircraft thrust in propeller mode. The wings provide the dominant lifting force in propeller mode in order to make up for the loss of lift from the rotors. High forward speeds should be attainable since the inefficiency for a pure helicopter of having the rotors remain nearly horizontal and provide both propulsive and lift forces is avoided for the tilt rotor. The tilt rotor concept has been investigated for more than half of a century by numerous researchers. The first tilt rotor aircraft, the XV-3, was built by Bell Helicopters Inc. in 1954 and is shown in Figure 1.2. Although the XV-3 itself never achieved the promised high forward speeds, it did prove that the rotor system could be tilted independent of the wings. The XV-3 demonstrated the basic practicality and technical advantages of the tilt rotor concept for use on a VTOL (Vertical Take-Off and Landing) transport aircraft. It also provided a firm data base with invaluable information for the eventual XV-15 and V-22 programs.

During the XV-15 and V-22 programs, conflicting design requirements on tilt rotor components were well understood, resulting in a choice of compromised design solutions on various

(a) Helicopter Mode

(b) Transitioning

(c) Propeller Mode

Figure 1.1: Conversion of V-22 from helicopter mode to propeller mode [1].

fronts: primarily the twist and length of the rotor blades. For instance, the blades on the tilt rotor are moderately twisted, which is a design compromise between highly twisted blades on a typical propeller and blades with a low twist on a typical helicopter rotor. The driving factor for the choice of blade twist is the efficiency of the rotor performance. Low twist blades are more efficient for hovering flight, whereas highly twisted blade improve the efficiency in high speed axial flight. Similarly, the length of the blades are long compared to those on

Figure 1.2: Picture of first tilt rotor, XV-3, in forward flight [2].

a typical prop-rotor but short compared to those on a typical helicopter. Disk loading of the rotor, defined as the ratio of thrust to the disk area, affects the efficiency of the rotor in hover. High disk loading, which is a consequence of smaller disk area is observed to be inefficient in hover, but beneficial in high speed axial flight. This criterion of disk loading dictates the length of the rotor blades. Hence, the efficiency in both modes of operation is lost, yet a compromise is adopted to achieve an expected unparalleled advantage of a large flight envelope with unique capabilities. Furthermore, the wing section is chosen to be a cambered airfoil with flaps. The choice of the wing section is dictated by a requirement to maximize lift in the propeller mode and to minimize the download in the helicopter mode. The download resulting from the downwash impingement from the rotor on the wing, in the helicopter mode.

The payload capability of tilt rotor aircraft is limited by the lifting capability of the vehicle in helicopter mode (associated with engine power), since the engines are equipped with ample power to cruise at higher speeds in the propellor mode. The wings can produce more lifting

force at these higher speeds than the hovering rotors. Hence, the reduction in the payload capability as a consequence of the rotor downwash impingement on the wing, is of extreme importance. The small size of the rotors increases the disk loading required to carry the mission governed payloads. The high disk loading on the rotors leads to an increment in the rotor downwash velocity further exacerbating the download experienced by the wing. A desire to better understand the interaction between the rotor downwash and the rest of the vehicle led to the initiation of the current research. Therefore, this work mainly concentrates on the helicopter mode of tilt rotors and attempts at understanding the flow physics in this mode of flight.

1.1 Motivation for Quad Tilt Rotor

The Department of Defense in 1998 identified a need for a yet higher payload VTOL aircraft for a global rescue mission. The capability to fly to any hostile global location and carry out an evacuation process for a large number of personnel was desired. To satisfy the demands of the Department of Defense, Bell Helicopters Inc. proposed the development of a high payload VTOL aircraft known as the Quad Tilt Rotor (QTR) [4]. A proposed design of the QTR is shown in Figure 1.3. This design shares many components with the V-22, for example the T406 engines, nacelles, drive systems and power plants. In addition, a large part of the wing structure and systems would be common between the V-22 and the QTR, including the fuel system and the conversion mechanism. Additional lifting capability in forward flight and hovering flight is gained by the augmented aft wing and rotor systems, resulting in a total of four rotor systems. Furthermore, the fuselage would be suitably enlarged to that of a C-130 class aircraft (Figure 1.4), theoretically enabling the transport of up to 100 passengers or a 40,000 pound payload at a maximum cruise speed of 280 knots. Along with the capability of global rescue mission, the QTR is proposed to be able to transport a 20 ton payload to a destination with in a 500 miles radius.

The QTR would share many components with the V-22 and simplify the design process,

Figure 1.3: Proposed design of the Quad Tilt Rotor (QTR) [3].

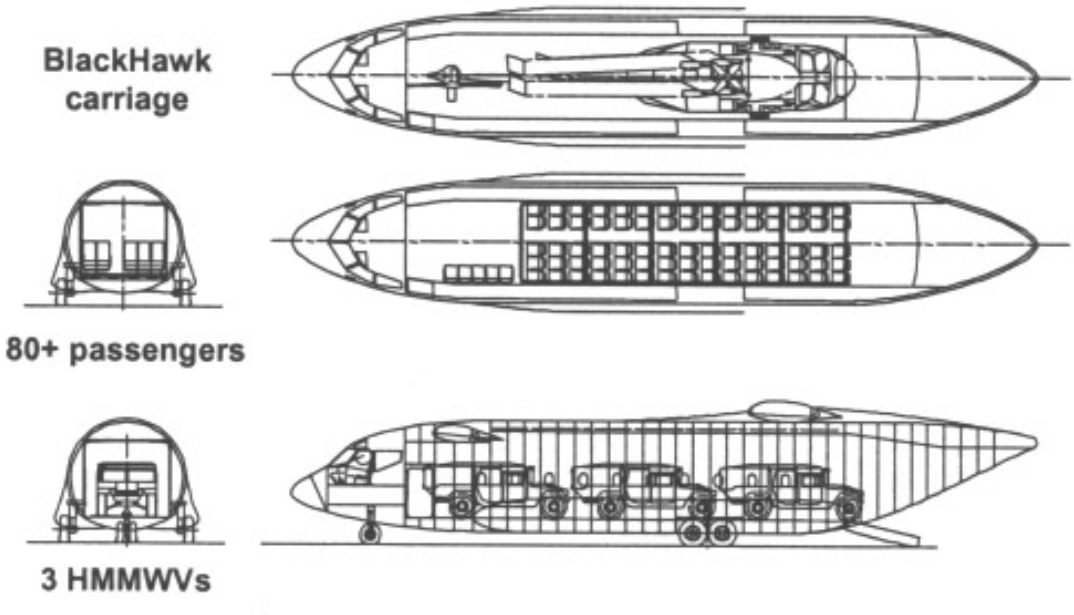

Figure 1.4: Payload Configuration of the Quad Tilt Rotor [4].

yet the aerodynamic issues involved in the development of the QTR are worsened because of the presence of an additional wing and set of rotors. For instance, in forward flight the operation of the aft wing and rotor systems in the wake of the front wing, nacelles, pylons, and rotors may lead to a change in performance, increased vibration and decreases controllability. Similarly, the tip vortex structures of the front propellers will interfere with the QTR components (front wing, rear rotor, rear wing) downstream of them. However, the aerodynamic interference issues in the propeller mode are expected to be of lower significance than the download penalty in the helicopter mode.

In hover, the download problem mentioned earlier for conventional tilt rotors may become much more complicated for the QTR because of the additional interactions between the front and aft rotor systems and wings. The download is observed to fade away with forward speed for the V-22 [17]. This decay of download with forward speed is shown in Figure 1.5. In this experiment, the fuselage was given an angle of attack of -10^o and the flap was set at -75^o and the download was measured at three different thrust coefficients (C_T). The forward speed is normalized with respect to the induced velocity (w_o). The figure shows a steep drop in download beyond the normalized forward velocity of 0.5. For the QTR the interaction between the front and rear rotor systems would be even stronger in slow forward flight conditions in helicopter mode, because the downwash of the front rotor would be skewed backward in forward flight interfering with the rear rotor and rear wing. The presence of the rear wing and rear rotor may cause the download to persist until higher forward speeds on the QTR than for the V-22.

There may be a requirement for even higher payload capabilities, depending on the mission requirement. Some relief in the download on the aircraft, as a result of downwash impinging on the wing, is observed for the V-22 In Ground Effect (IGE) operation [18]. Tilt rotor vehicles may be able to perform rolling takeoffs with higher payload, taking advantage of the ground effect. This relief is a consequence of an upward force experienced by the fuselage and inner sections of the wing when they are located very close to the ground. Understanding the behavior of the QTR IGE operation is a difficult task that needs careful attention.

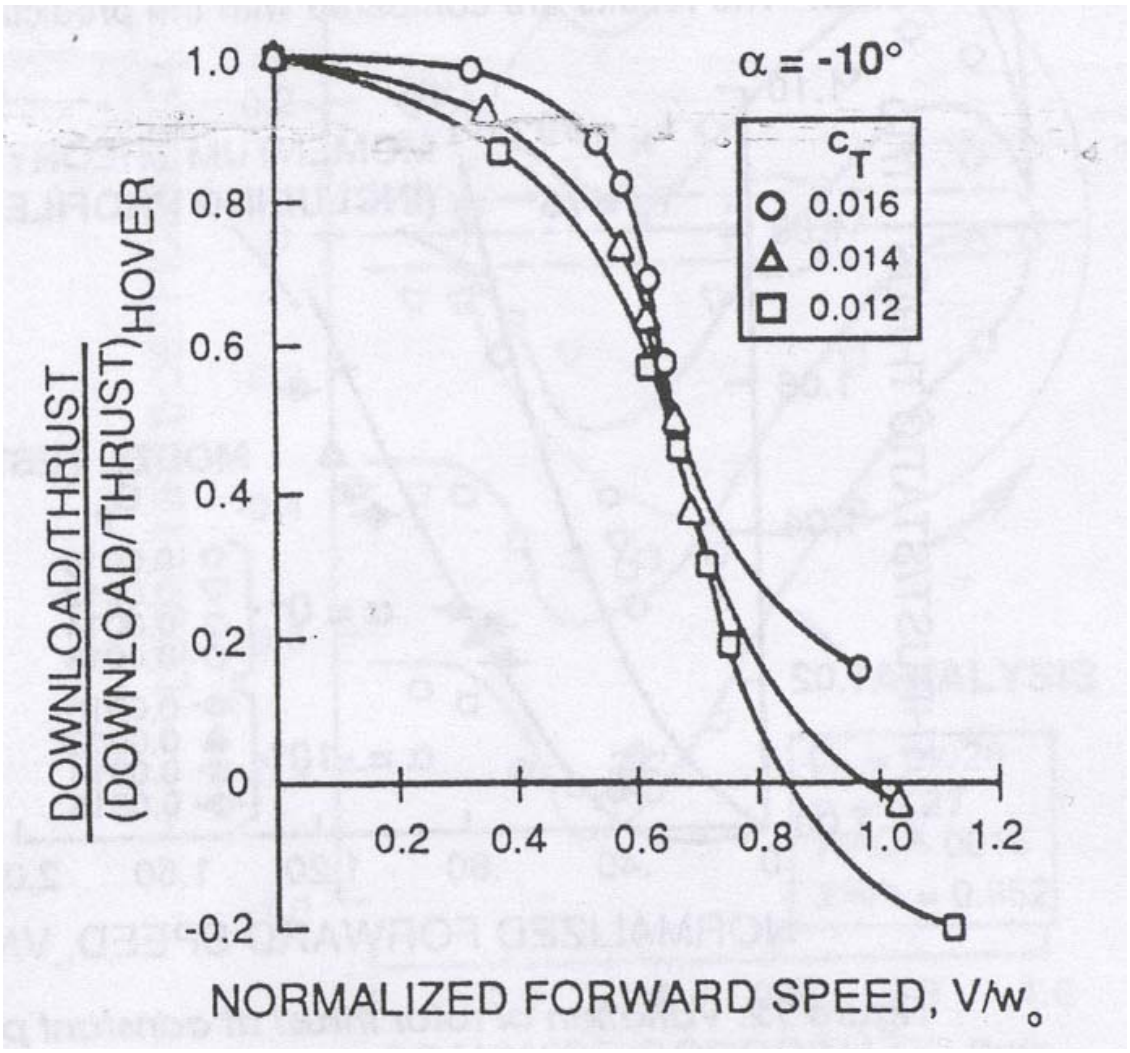

Figure 1.5: Decay of download for a model scale V-22 with forward speed for different thrust coefficients (C_T) [17].

The interactions among the various components are of extreme importance and need to be accurately modeled to quantify the download on the QTR with adequate accuracy. This download clearly determines the payload capability of the aircraft. Since, high payload capability is the driving force behind the initiation of the QTR program, sufficiently accurate prediction of the download both in and out of ground effect is of great significance in the design process. Therefore, such benefits need to be better quantified, especially as the forward velocity is increased and the vehicle accelerates in or out of ground effect.

In summary, the focus of this dissertation is to study the download on the wings and fuselage in hover and low speed helicopter mode, both in and out of ground effect to better quantify the possible benefits and determine the physical mechanisms responsible leading to an increase in payload capability for a Quad Tilt Rotor vehicle.

1.2 Flow Mechanism Causing Download on Tilt Rotors

Numerous experiments have been conducted to investigate the download on the wing for a hovering tilt rotor configuration and quantify the overall reduction in thrust for the whole aircraft. The flow patterns involved in the proximity of the wing and the rotor in hovering conditions are very complex and need careful analysis.

In a typical tilt rotor configuration, the downwash from the rotor impinges upon the top surface of the wing and splays in the chord wise and span wise directions. The chord wise flow separates as it tries to go around the leading and trailing edges to the bottom surface of the wing, resulting in a large region of separated flow with a large pressure difference between the top and bottom surfaces of the wing. This pressure difference between the top and bottom surfaces of the wing results in a downward force [7], reducing the payload capability of the aircraft. The span wise flow moves on the top surface inwards until it reaches the centerline. There it encounters the flow from the other side of the vehicle and is deflected upward, resulting in a fountain flow at the center of the vehicle. This upward flow is re-ingested into the rotor system leading to a possible unsteadiness in the inflow of the rotor and a possible degradation of the rotor performance. These complex flow patterns are conceptually sketched on a longitudinal plane through the wing in Figure 1.6.

The flow features In Ground Effect (IGE) operation (also shown in Figure 1.6) are further complicated by the presence of the ground plane in the rotor downwash and have not been investigated in as much detail. The rotor downwash outside the wing tips which flows down for Out of Ground Effect (OGE) hover is obstructed by the ground plane. Similar to the top surface of the wing, the flow splays in the longitudinal and lateral directions after impinging

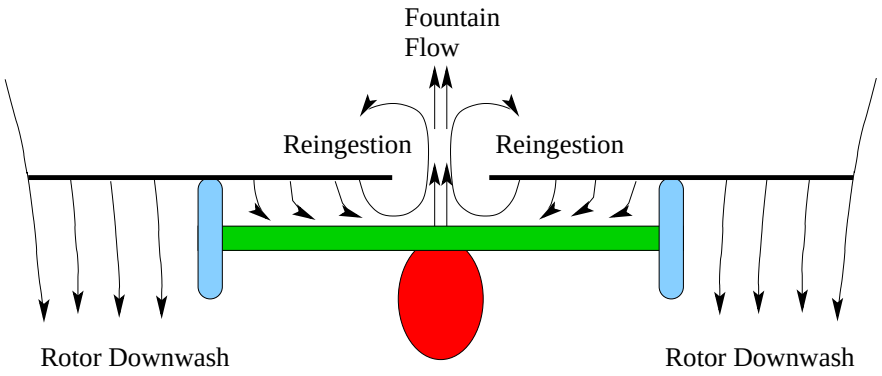

(a) Out of Ground Effect (OGE)

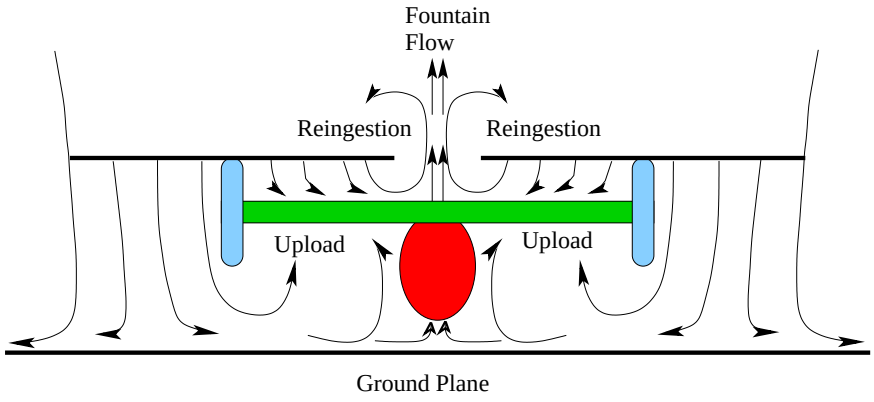

(b) In Ground Effect (IGE)

Figure 1.6: Flow pattern on a longitudinal plane through the wing in hovering conditions(Front View).

onto the ground plane. The lateral flow meets its counterpart at the centerline below the fuselage surface and results in an upward flow causing an upward force on the fuselage and inner sections of the wing [18]. In some situations, this upward force on the inner sections of the wing and the bottom surface of the fuselage might balance the downward force on the outer sections of the wing, leading to an increase in the payload capability of the aircraft in this condition. Furthermore, the rotors are more efficient operating IGE; with decreased power required for the same thrust.

The higher lifting capability of the aircraft in hover IGE (for the same engine power) will only be of benefit if it can also be maintained in slow forward flight, such that the vehicle could obtain the benefits of reduced download on the aircraft in slow forward flight before rising to operate out of ground effect. Exploring the loading pattern on the aircraft in slow forward flight, yet in the helicopter mode, is of great significance in realizing the benefit of the upload/lower download IGE operation.

1.3 Experimental Work on Tilt Rotors

Various experimentalists have studied the tilt rotor vehicles as a whole and its components in isolation to aid in a better and efficient design of a tilt rotor vehicle. Significant investigations involving the helicopter mode of tilt rotor aircraft are elaborated in this section.

1.3.1 Isolated Rotor

Experiments have been conducted on tilt rotor components since the 1950's. Tung and Branum [5] conducted experiments to study the performance of a small three bladed model isolated tilt rotor (solidity 0.1194 and non-linear blade twist 32 degrees) in hover. They studied the effect of various parameters on the performance of a hovering rotor and also investigated the pressure distribution on the blades as a function of collective pitch and rotational speed. This study was carried out for an isolated rotor system. There was no sign of flow separation near the leading edge of the rotor blade even at high collective pitch angles, hence no loss of thrust was observed, which was contrary to the expectations. The consistency in thrust at these high collective pitch angles was attributed to three dimensional effects, which prevented separation. Wake measurements of an isolated tilt rotor were also conducted by Yamauchi and Burley [6]. This study was not aimed at performance analysis of the rotor, but at reducing the BVI noise, which was observed to be a dominant source of noise during various operating conditions for tilt rotors. This study still is a good source of data for velocity measurements in the rotor wake.

The repercussions of the wing lying below the rotors in a helicopter configuration were not examined in the investigations conducted by Tung and Branum and Yamauchi and Burley. It is necessary to analyze the interaction between the rotor and the wing to better predict its ramifications on the performance of the tilt rotor aircraft.

1.3.2 Rotor Wing Interaction

Felker and Light [7] studied the aerodynamic interaction between the rotor system and the wing. They varied geometric parameters including the vertical distance between the rotor and the wing, wing incidence angle, wing flap angle, rotor rotation direction and configuration with rotor at the tip of the wing and with the rotor axis at the center of the wing and analyzed their effect on the download on the wing and the variation of rotor thrust. The effect of these geometrical variations was studied on a small scale (0.16 scaled) model. They also conducted experiments on a configuration of a 0.658 scale model of a V-22 wing and rotor. Pressures were measured at several locations on the wing to investigate the variation of the loading along the span of the wing. Felker [8] studied the effect of these geometrical variations on a full scale model later to avoid the Reynolds number inconsistency that is inherent while conducting experiments on a small scale model. Although the lower Reynolds number in this case would not make significant difference, because the flow separation is driven by the topology and not by the Reynolds number. The wing download and surface pressures were measured for a wide range of thrust coefficients with five different flap angles, and for both directions of rotor rotation. The wing flap was shown to produce a substantial upload in some cases without significant alterations to the pressure distribution on the rest of the wing. The lift produced by the flap led to an overall reduction in the download on the flap wing combination. The download to thrust ratio was observed to slightly decrease with increasing thrust coefficient of the rotor. However, the magnitude of the download was observed to be close to 10% of rotor thrust in all the configurations. This study involved an exhaustive investigation of different geometrical parameters and provided a large database of information which was quite beneficial in the design process of the V-22.

Matos et al. [9] studied the rotor wake/fixed wing interactions with varying flap deflections. As observed by previous studies, the download on the wing reduced with increasing flap deflection angle until 67 degrees. This work was a follow up of a study conducted by Funk and Komerath [10] to analyze rotor wake interaction with a lifting surface. They observed a strong N_b per rev variation of loading on the wing because of the pressure loading on the blades of the rotor.

1.3.3 Effect of Image Plane

In the studies mentioned above, an image plane was used to study the "fountain flow", which was evident near the fuselage and wing intersection. High velocity span wise flow was observed near the root of the wing. The image plane forced this span wise flow to move up towards the rotor and hence increased the intensity of the fountain flow. Similar observations were made by Polak et al. [11] in their attempt to study the effect of the image plane on the tilt rotor fountain flow. They employed 0.08-scale model of the XV-15 tilt rotor. Flow fields were visualized using surface tufts and helium bubbles. The magnitude of fountain flow was determined by measuring the vertical velocity using a hot wire anemometer just above the rotor close to the symmetry wall. As expected, the fountain flow was observed to be higher in the semi span model as compared to the full span model, as expected. Lateral aperiodic shifting of the fountain flow was observed on either side of the fuselage in the full span model, which was prevented because of the symmetry constraint in the semi span model. The upward velocities are forced to be zero on the symmetry plane, which will not be the case in the full span case. A boundary layer is also developed on the symmetry plane.

1.3.4 Download Reduction Strategies

Realizing the magnitude of the download, Woods and Peryea [12] investigated various download reduction devices by mounting them on the XV-15 models. The download reduction devices employed in this study consisted of fences and prisms installed over the wing upper surface in various configurations. They observed favorable effects and were able to increase

the lifting capability of the aircraft by 2-3%, which enabled the aircraft to carry higher payloads. All the devices employed by Woods and Peryea were passive download reduction devices and set a firm background for the development of active flow control devices.

Active download reduction methods like surface blowing were implemented by Matos and Komerath [13], Lee [14] and Felker [15]. Lee investigated the use of a surface blowing technique on an airfoil and reduced the download by slightly displacing the separation point in the chord wise direction, as a result modifying the pressure distribution on the upper surface. Felker conducted experiments on a small scale model and studied the effect of boundary layer control, as a result of surface blowing, on download reduction. They achieved significant reduction in download (between 25 % and 55 %). Matos and Komerath analyzed the effect of surface blowing along with the deflection of flaps as a means of reducing the download on the wing. No benefits were observed in low speed forward flight as a result of surface blowing.

Liu et al. [16] also conducted experiments on model and full-scale tilt rotors and quantified the download on the wing, and investigated the applicability of download reduction devices, in hovering flight condition. They utilized a "Butterfly" device, which bifurcated the span wise flow into two chord wise streams and hence reduced the fountain flow. This lead to a significant improvement in power requirements for a given thrust of the rotor.

1.3.5 Tilt Rotors in Forward Flight

All the studies discussed previously concentrated on hovering flight. McVeigh et al. [17] conducted experiments in a wind tunnel analyzing the effect of forward speed on the V-22 and XV-15 wing download as a result of the rotor downwash. They observed that the download on the wing remains almost constant (around 12% of the rotor thrust) until 13 knots (corresponds to skewing of the rotor downwash by 22 degrees) and then drops significantly with forward speed, reaching a value of zero download at around 30 knots (skewing of rotor downwash by 40 degrees). The forward speed causes the flow through the rotor to skew backwards, modifying the angle of impingement onto the wing and hence reducing the download

on the wing. The skewing of the flow is approximately equivalent to tilting the rotor by that angle, which is observed to reduce the download on the wing in other experiments. This experiment clearly illustrated the disappearance of the download on the aircraft with low forward speed, although still in helicopter mode of flight.

1.3.6 Effect of Ground on Tilt Rotors

Desopper et al. [18] for the first time published results analyzing the effect of the ground on the performance of a tilt rotor. This work was conducted in Europe on a representative tilt rotor. They also developed semi empirical analytical models to predict low speed characteristics of the tilt rotor based on experiments conducted for different configurations. They employed a semi span model of the tilt rotor to investigate the effect of flap setting and thrust levels on the download on the model. This was a comprehensive study involving the variation of several parameters that lead to modifications in flow patterns and loading on the aircraft. They demonstrated the reduction in download on the tilt rotor with forward speed, similar to McVeigh [17], although the rate of reduction was much lower than that shown by McVeigh. The download on the tilt rotor was observed to reduce to a value only 20% of the OGE download in hovering flight when the rotor was 1.115 rotor radii above the ground. This configuration was equivalent to simulating the tilt rotor vehicle with wheels on the ground. The download IGE increased initially with forward speed, but started to decrease around 30 knots. This exhaustive experimental investigation will be very helpful in comparing trends in download on a tilt rotor with the corresponding variation for the QTR.

1.3.7 Quad Tilt Rotor

Very few experiments have been conducted to investigate the QTR. As a result an experimental approach was initiated at the University of Maryland, in parallel with the computational work performed for this dissertation, in order to experimentally quantify the download on a simplified model of the QTR. This work was conducted by Radhakrishnan and Schmitz [19]. They fabricated a small scale simplified, yet representative model of the QTR and measured

the download on the model as a consequence of the rotor downwash. A parametric study of the download variation with height from the ground was also conducted.

Later, they also conducted experiments in forward flight [20] by moving the small scale QTR model set up using a golf cart. A moving golf cart accurately simulates the boundary layer on the ground as experienced by the QTR in flight, which would not be the case in a wind tunnel. In other words, in the wind tunnel differential velocity between the QTR and the ground is not modeled. This accurate boundary layer modeling is very important while investigating the download on the QTR close to the ground. They observed a reduction in download with an increase in forward speed as seen in other experiments on tilt rotor models. This work is an invaluable source of information of the download measurements on the QTR for several flight conditions and can be utilized for validation of numerical techniques.

1.4 Computational Work on Tilt Rotors

Various numerical methods have been applied to study the tilt rotor flow field in the helicopter mode. Clark and McVeigh [21] solved Laplace Equations in two dimensions using panel methods. They could only predict the overall features of the flow, because of the nature of equations solved. Assumption of irrotational flow (inviscid) in potential equations is violated in this problem. Although, the separation cannot be predicted using this method, it was a beginning for computational methods applied to the current problem.

Raghavan et al. [22] performed unsteady two dimensional Reynolds Averaged Navier-Stokes (RANS) computations on the XV-15 airfoil at -90 degree angle of incidence in a low Mach number and low Reynolds Number free stream conditions. This would emulate the flow environment experienced by an airfoil section of the XV-15. This was a novel approach, but could not correctly predict the download, because of its inability to predict the base pressure accurately. This inability can be attributed to the two-dimensional assumption which neglects any cross flow. This assumption leads to a lot of discrepancy when the flow separates and is inherently three-dimensional.

1.4.1 Actuator Disk Approach

Fejtek et al. [23] took the state-of-the-art further and solved the Reynolds Average Navier Stokes equations in three dimensions to analyze the wing/rotor interaction for a hovering tilt rotor. They anticipated the flow field to be less constrained in three dimensions as compared to the two dimensional study conducted by Raghavan et al. and hoped for more accurate predictions, because of the reduced strength of vortex shedding and turbulence in the wing wake. They used an actuator disk to model the rotor, across which pressure and swirl velocity were varied, depending on the blade characteristics. They studied the effect of introducing the wing (flap deflection of 67 degrees) below an isolated rotor (C_T =0.0164). They used a single wing conforming mesh to study the wing rotor interaction. The mesh utilized in this approach conformed with the wing surface and not the actuator disk. Hence, the pressure jump predicted by the actuator disk model was not incorporated at exact locations and is an inherent source of inaccuracy.

The inability to easily model the complex interfering aircraft components led to a more general Cartesian grid method developed by Poling, Rosenstein and Rajagopalan [24]. They solved the incompressible Navier Stokes equations on a Cartesian grid and modeled the rotor as a similar actuator disk and the solid body surfaces using source terms. They did not model the viscous effects accurately on the wing surface and other components. Furthermore, although a RANS approach was used it is unlikely, due to the coarse mesh spacing, that turbulent effects were correctly modeled. This approach is very general and ideal in providing a good overview of the flow field. However, inaccurate modeling of viscous effects causes loss of fidelity of the approach, especially for this problem, where accurate prediction of the point where the flow separates is of extreme significance.

A study using a multi-block Navier Stokes method was also conducted by Tai and Vorwald [25]. They simulated the flow over the fuselage, wing and the rotor-nacelle assembly tilted at 90 degrees. They applied a rotor actuator disk model, although with momentum theory, to simulate the flow field induced by the rotor. Unfortunately, the use of simple momentum theory eliminated any variation in the rotor induced velocity in the azimuthal or radial

direction. They simulated the flow field around the V-22 aircraft in ground effect. They did not quantify the download on the wing and fuselage as a result of the impinging rotor downwash, but qualitatively illuminated the flow features around the aircraft surface.

A preliminary study of flow field characteristics of the QTR in hover was performed by Lestari, Niazi and Rajagopalan [34], using an incompressible Navier Stokes solver. They studied the hover characteristics IGE and OGE, using a Cartesian grid. They modeled the aircraft geometry by adding source terms in the Navier Stokes solver and also modeled the rotor as a disk across which the source term changed depending on the lift and drag produced by the rotor, which was modeled using blade element theory. The download on the QTR was calculated to be 9.1% OGE. This download OGE transformed into an upload of 0.5% IGE. This was an extension of the earlier work on the V-22 aircraft, now applied to the QTR. Thus, there were inaccuracies involved in the prediction of the separation point on the wing surface because of the inaccurate modeling of the viscous terms. Lack of body conforming meshes in this approach leads to inaccurate modeling of the boundary layer.

1.4.2 Moving Mesh Approach

The rotor was modeled in the previous approaches using an actuator disk, ignoring the effect of individual blades and attempting to capture the overall effect of the rotor flow field. Meakin [27] conducted a more complete study of a V-22 rotor system in hover, by accurately modeling all the components, including individual blades. A moving body overset grid technique was used to capture the unsteady effects introduced from the rotation of the blades. In this approach, individual blades were modeled with their own meshes and these meshes were rotated relative to the background mesh. The rotation of blade meshes relative to the background mesh forced the calculation of new connectivity information between the grids at every time step. A compressible RANS solver was used because of the compressibility effects in the tip regions of the blades. The effect of fountain flow can be clearly seen in the time histories of thrust and torque. A symmetry boundary condition was used in this simulation. Thus, flow unsteadiness in the span wise direction as observed by Polak [11] in the

experiments conducted on the full scale model cannot be captured because of the application of the symmetry boundary condition. The method adopted by Meakin requires tremendous computational resources, on the order of 10,000 processor hours. A similar approach was adopted by Potsdam and Strawn [28] to simulate a tilt rotor in various configurations in hover; they simulated the isolated rotor and installed half span and full span models. They compared the results with experiments and obtained a good comparison. Similar to Polak [11], Potsdam and Strawn [28] also observed a lower download for the full span model than the semi span model. These simulations were run at a constant collective setting without any flap dynamics.

1.4.3 Comparison of Actuator Disk and Moving Mesh Approaches

The two approaches to model the rotor employed previously are the actuator disk approach and the moving (overset) mesh approach. The actuator disk approach ignores the effect of individual blades, but captures the overall effect of the rotor flow field. The moving overset mesh approach is a high fidelity approach, but is computationally intensive. The Cartesian grid approach, which along with simplifying of the modeling of rotor as an actuator disk, further simplifies the modeling of solid surfaces as source terms. These two approaches, namely the Cartesian grid approach and moving overset mesh approach, are compared in a work by Potsdam et. al [29]. The Cartesian approach is utilized as a good design tool, while high fidelity solutions are obtained using the moving overset mesh approach. Various flight conditions of the V-22 were simulated in this work and the download on the aircraft was compared with McVeigh's experiment [17] for forward flight as well as flight test data.

1.5 Current Approach

As stated earlier, the payload capability of tilt rotor aircraft is limited primarily by their lifting capability in the helicopter mode. Thus, the primary objective of this research is to investigate the various aerodynamic interference effects in hover and low speed forward

flight. The major research tasks performed are the following :

- Computational investigation of download from rotor systems on the wings and fuselage in hover.
- Quantitative assessment of possible benefits and deficits both in and out of ground effect.
- Investigation of the key physical mechanisms of aerodynamic interference affects.

Exploring the loading pattern on the aircraft for a wide range of conditions in slow forward flight, yet in the helicopter mode, is of great significance in realizing the benefit of the upload/lower download IGE operation. This requires a high fidelity approach along with use of an efficient computational algorithm.

In the current work, a compromise between the two previously mentioned computational approaches is established. The actuator disk rotor model is adopted from the Cartesian grid approach and overset meshes are taken from the moving overset mesh approach to accurately model the stationary components of the aircraft (the wings and the fuselage). This approach does not require calculation of connectivity information after every time step, because there are no moving components, but it does resolve the viscous derivatives at the surfaces of the solid boundaries by employing body conforming meshes accurately and also captures the overall effect of the rotor. Since the effects of the rotor blades in the actuator disk model are time-averaged one can use acceleration techniques, such as preconditioning to obtain a steady state solution. In addition, the use of overset meshes allows for the geometry of the wings and fuselage to be handled accurately and efficiently.

The velocities in the proximity of the wing in the helicopter mode are observed to be small. Furthermore, the application of the rotor model reduces the velocities in the vicinity of the rotor blade tips since the rotor model does not rotate the blades, instead it only includes the induced planar and normal velocities across the rotor disk. However, it is not known whether the velocities are of such a small magnitude that an incompressible assumption will always remain valid. Therefore, in this work the governing equation to be solved is chosen

as the compressible Reynolds Averaged Navier-Stokes equations (with a turbulence model for closure). Spalart Allmaras turbulence model is used in this work. This model has been extensively used in the past to model external flows accurately. Traditional compressible solvers are observed to be inaccurate and inefficient for low Mach number flows. Therefore, the algorithm for the numerical solution of the compressible solver is modified to ensure accurate solutions at a faster rate than for traditional compressible solvers. This modification of the solver is known as low Mach number preconditioning. This modifies the wave speeds of the hyperbolic Euler equations and also the dissipation terms associated with upwinding. These modifications are explained in later chapters.

In the hovering condition, separation of the boundary layer will occur at the leading and trailing edges of the wings, but as the aircraft moves forward, the point of separation will move downstream on the bottom surface of the wing. This movement of the point of separation cannot be predicted without the inclusion of viscosity in the solver. Although, the effect of this movement of point of separation will not be large on the download experienced by the QTR. More importantly, it is essential to predict the pressure at the bottom surface of the wing accurately, which will be different from free stream pressure. Accurate modeling of the turbulent wake below the wing will lead to accurate prediction of the pressure below the wing. Spalart Allmaras turbulence model, used in current work, has been implemented to model separated flows accurately [38, 40–42] in the past and is the most appropriate choice. More details about the selection criteria is provided in later chapters.

When the aircraft operates in ground effect, the boundary layer prediction on the ground is very important. In this regime of operation, the ground forces the rotor downwash to turn in a direction parallel to the ground. This turning of flow can also alter the viscous effects near the ground. The current approach with Spalart Allmaras turbulence model aids in predicting the viscous effects properly and capturing the highly turbulent flow in the wake of the wings. This highly turbulent flow goes through the downstream boundary for out of ground effect operation, but this flow interacts with the ground plane in close to the ground plane operation and is fed back into the region of interest. It is very essential to model the

turbulence appropriately to predict this feedback accurately.

When the QTR operates close to the ground, there is a relative velocity between the QTR and the ground (absent in wind tunnel testing). In a CFD approach, forward flight of an airplane is modeled by keeping the airplane stationary and providing relative velocity to the wind. If the ground plane is modeled as a stationary surface, there will be relative velocity between the approaching wind and the stationary ground plane, which is not the case in true flight. To model it correctly, the ground plane is forced to translate with the free stream velocity to obtain the relative velocity between the QTR and the ground plane and no relative velocity between the wind and the ground plane. This moving wall implementation is equivalent to using a conveyor belt at the bottom surface of the wind tunnel moving with the wind velocity where as the aircraft is held stationary. This moving viscous wall model modifies the shear fluxes on the boundary to obtain such a condition.

The validity of the chosen mesh system and governing equations are first verified for simplified model problems relevant to tilt rotors operating in helicopter mode. Once sufficient confidence is demonstrated for these simple cases the more complex quad tilt rotor system is examined for a wide range of conditions both in and out of ground effect. Quantitative information is extracted to determine the benefits of IGE operation as well as understand the physical mechanisms responsible.

1.6 Organization of Thesis

This Chapter provides an overview of the previous work and the underlying problems to be investigated. Chapter 2 describes in detail the methodology adopted to address the aforementioned issues. Specifically it begins with a discussion of structured curvilinear meshes and overset grid techniques. It is followed by a detailed description of the governing equations chosen (RANS, turbulence model and rotor model), and the algorithms adopted to solve the equations. Specifically, low Mach preconditioning will be explained, which was deemed necessary to simulate these low Mach number flows using a compressible solver.

Chapter 3 is concerned with verifications and validations. Initially, the effectiveness of low Mach number preconditioning is illuminated by its application for simulating low Mach number flows over airfoils. A model rotor-wing interaction problem is simulated, which along with building confidence in the current algorithm, also estimates the magnitude of the the free stream velocity, which is sufficient to approximate hovering flight. Representative experiments modeling an isolated rotor and rotor-wing interaction are selected and similar conditions are simulated using CFD. This comparison with results obtained by tilt rotor experiments will be beneficial in building more confidence in accuracy and consistency of the solution procedure.

This will be followed in Chapter 4 by a discussion of the grids employed to model the complicated geometry of the QTR with sufficient accuracy. Overset meshing issues as applied to the current problem is also discussed in detail. Various parameters used in the solution procedure are also highlighted here. The results and discussion of the application of the methodology to the problem of the Quad Tilt Rotor operating in helicopter mode, both OGE and IGE are contained in Chapters 5 through 7. Chapter 5 deals exclusively with hovering flight while Chapter 6 is concerned with forward flight. In Chapter 7 a brief comparison is made between computational simulations and the only QTR experimental results currently available.

Chapter 8 provides closure with a summary of the work along with key conclusions and recommendations for future work.

Chapter 2

Methodology

Solving the complex problem of simulating flow around the Quad Tilt Rotor (QTR) is a daunting challenge and an accurate but not elaborate method is desired to obtain an engineering solution. Flow below the wing is highly separated and a mesh that would capture this flow separation accurately is required. Structured curvilinear meshes around the solid bodies are employed in this work to ensure accurate modeling of viscous effects and are discussed in this chapter. An overset grid (overlapping structured grids) based method is used to model the complicated geometry of the QTR to study its performance in various configurations and flight conditions. This approach involves modeling of different components utilizing simple structured grids that are aligned with the solid boundaries for better resolution of the viscous effects. Exchange of information is an essential component of the overset mesh technique and is discussed subsequently. The governing equations are the Reynolds Averaged form of the Navier-Stokes (RANS) with Spalart Allmaras turbulence model for closure. The formulation of RANS equations is presented next in this chapter. The stationary components are modeled using body conforming curvilinear meshes, but the rotor is modeled as a circular disk using body forces in the Navier Stokes equations. This rotor model which calculates these body forces and appropriately appends them to the Navier Stokes equations is discussed next. The discretization and solution algorithm for the compressible RANS equations on the overset structured curvilinear grids is described next. The low Mach number region around the wings limits the use of a compressible flow

solver. Therefore, a few modifications to the existing flow solving technique are necessary. A preconditioning technique, which aids in generation of a more accurate solutions at faster rates is described towards the end of the chapter.

2.1 Structured Curvilinear Meshes

For simulating the flow around the Quad Tilt Rotor, it is necessary to generate a grid around the solid surfaces of the QTR geometry. Body conforming structured curvilinear meshes are chosen in the current methodology. Structured curvilinear meshes are aimed at capturing the viscous effects accurately by modeling the boundary layer in an appropriate manner. Separate structured meshes are generated around different components and communication techniques are developed between the these individual component grids to model the QTR as a single entity.

A structured mesh can be mapped (one to one) to a Cartesian mesh. For instance, a structured C topology mesh around an airfoil (shown in Figure 2.1) can be unraveled along the wake cut to generate a Cartesian mesh. Another property of a structured mesh is that any grid point in a structured mesh can be uniquely defined by a set of indices (ξ, η, ζ). The two properties are synonymous, because any grid point in a Cartesian mesh (it is a structured mesh) can also be uniquely defined by a set of indices. These indices signify the grid lines of a structured mesh and a grid point in three dimensions is defined by an intersection of three grid lines. Hence, the three indices denote the three grid lines which intersect at that grid point. The dimensions of a structured mesh can be written as a product of three numbers. Each number depicts the number of grid point along the three grid lines.

Another advantage of using a structured mesh is the ease of solving the governing equations on them. A curvilinear structured physical mesh can be mapped to the Cartesian equally spaced computational domain. Once this transformation is obtained, the governing equations can be discretized in the equally spaced Cartesian computational domain. The governing equations can be easily formulated on a Cartesian mesh and this approach reduces a lot of

complexities.

The computational domain is discretized into a generalized curvilinear co-ordinates defined by ($\xi = \xi(x, y, z)$, $\eta = \eta(x, y, z)$, $\zeta = \zeta(x, y, z)$). The transformation of the governing equations to the computational co-ordinates (ξ, η, ζ) is defined by the inverse of the space metrics K, which is defined below (The space metrics K transform the computational domain to the physical domain).

$$K = \begin{Bmatrix} \frac{\partial x}{\partial \xi} & \frac{\partial x}{\partial \eta} & \frac{\partial x}{\partial \zeta} \\ \frac{\partial y}{\partial \xi} & \frac{\partial y}{\partial \eta} & \frac{\partial y}{\partial \zeta} \\ \frac{\partial z}{\partial \xi} & \frac{\partial z}{\partial \eta} & \frac{\partial z}{\partial \zeta} \end{Bmatrix}, \qquad J = det(K)$$

This transformation simplifies the equations and the final representation is equivalent to solving the Navier Stokes equations on a uniformly spaced Cartesian mesh.

Hyperbolic and algebraic grids are generated in this work for the various components. While generating a hyperbolic mesh, the grid distribution is specified at the solid surface. Hyperbolic equations are then solved and the solution is marched outward from the surface in the normal direction. It is implied that there is no need to specify the outer boundary of this mesh, as it comes out as a solution. This is a very efficient means of grid generation. Finer grids are maintained close to the solid surfaces for capturing viscous effects accurately. Algebraic grids are even simpler to generate, where grid distribution at the solid surface is specified and the same plane is moved radially outward from the surface, using the normal spacing that is specified at the surface. However, it is difficult to generate orthonormal grids, which are preferred while simulating highly viscous flows, at the solid surface while using algebraic grids.

As discussed earlier, separate structured curvilinear meshes are generated around each solid surface. Hence, communication strategies are necessary for transferring information between different structured meshes to solve the problem consistently. This method of employing several structured meshes with non-matching interfaces and means of communication between the meshes, also called the overset mesh technique, is necessary in the current work because of the complicated geometry of the QTR that involves various components.

2.2 Overset Technique

Overset meshes are quite helpful in simulating flows over complicated geometries and capturing the significant flow features accurately. There are many benefits of using this technique. A complex geometry can be reduced to a set of simple structured grids. These structured grids can be arbitrarily moved in response to various loads. This technique is of great use in rotorcraft applications, because the relative motion of the blades with respect to the fuselage and other components can be effectively modeled using this method, although not done in this research. Parallel processing can also be easily implemented in this technique by solving the governing equations on these grids on different processors and transferring the desired information across the boundaries. Load sharing is very important while using parallel processing, which means number of grid points on the grids should be of the same order for optimal performance, if one grid is distributed to each processor. Accurate preprocessing of grids is very important, while using overset grids. Preprocessing of the grid mainly involves two steps: hole cutting and finding the interpolation factors [55–57]. These terms are descbribed in detail in subsequent sections.

Post processing of grids can also be complicated in overset mesh technique. A surface may be divided among several overlapping grids in this approach, hence evaluating the forces on such surfaces becomes non trivial. In such cases, overlap on the surface is removed and zipper grids which connect the grids on the surface (consisting of triangles) are generated. The solution is then interpolated onto the points on the zipper grids. This process uniquely defines the surface on which forces are calculated by integration of momentum fluxes.

2.2.1 Hole Cutting

Hole cutting of grid points is necessary to avoid contamination of flow solution due to the presence of invalid points in a grid. Definition of invalid points will be more evident after this example. In this example, overset technique is employed to simulate flow over an airfoil. A C mesh is generated around the airfoil and is shown in Figure 2.1. A background Cartesian

mesh is generated to define the far field free stream boundary condition and both overlapping meshes are shown in Figure 2.2. It is evident from Figure 2.2 that points on the Cartesian grid which lie inside the airfoil body are non-physical. Hole cutting is also referred to as blanking. It is achieved by creating an array of integers corresponding to the grid points with values 0 and 1 and multiplying the flux contributions from invalid points by 0 and valid points by 1. If these points are not blanked (hole cut), they would contaminate the solution, because the inaccuracies at these points will propagate in all directions. Hence, it is essential to nullify the contribution of these points in the flow solution. Also near the surface of the airfoil mesh, the Cartesian mesh is relatively coarse and will not be able to resolve the small scale phenomena in the boundary layer or close to the wall of the airfoil. Hence, a hole should be generated in the Cartesian mesh such that the hole not only encompasses the solid boundary of the airfoil, but also the fine cells close to the wall in the airfoil (C mesh) grid. An appropriate hole cut Cartesian mesh is shown in Figure 2.3. Various methods have been successfully used for hole cutting in the past [51–53]. A few of them are listed below :

- **Surface Normal Method :** If a point lies in the same direction to any surface normal pointing outward from the cutting surface, then the point is not blanked. The outward normal direction is defined by the grid lines around the cutting surface. This methods is robust, unless there are concave corners.

- **Ray Casting Method :** An arbitrary ray is cast from the point and depending on the number of intersections with the surface, the point is blanked. This method is extremely robust, but choosing an arbitrary ray is not trivial. This ray could follow the grid lines in blanking domain or the principal axis. If there are even number of intersections with the surface, the region in the middle of every alternate pair is blanked.

- **Hole Map Method [58] :** A hole map is constructed around the cutting surface using a Cartesian mesh. Using this Cartesian hole map, blanking for points is determined. Spacing in the Cartesian mesh used for generating the hole map is very important and

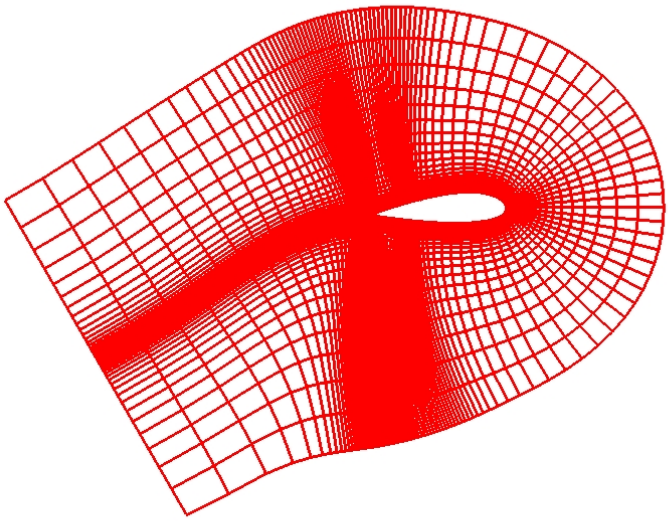

Figure 2.1: C mesh generated around an airfoil.

determines the accuracy of the method.

- **Object X-ray Method [53]:** This method borrows the ideas from both the Hole map method and the ray casting method. In this method a hole map is generated by casting rays in the vertical direction. So arbitrariness of the choice of the ray direction is no longer an issue and also spacing of the Cartesian mesh is not critical in the vertical direction, but is still important in the horizontal plane.

In the present work, surface normal vector method is used for hole cutting. All the hole cutting surfaces should be convex, in order to use this method. All the solid bodies simulated in this work were convex and were well suited for application of surface normal methodology.

The previous example is revisited to better elucidate the overset technique. In the example, the outer boundary of the airfoil grid gets the information from the Cartesian grid, which acts as a boundary condition for the airfoil grid, necessary for obtaining a unique solution of

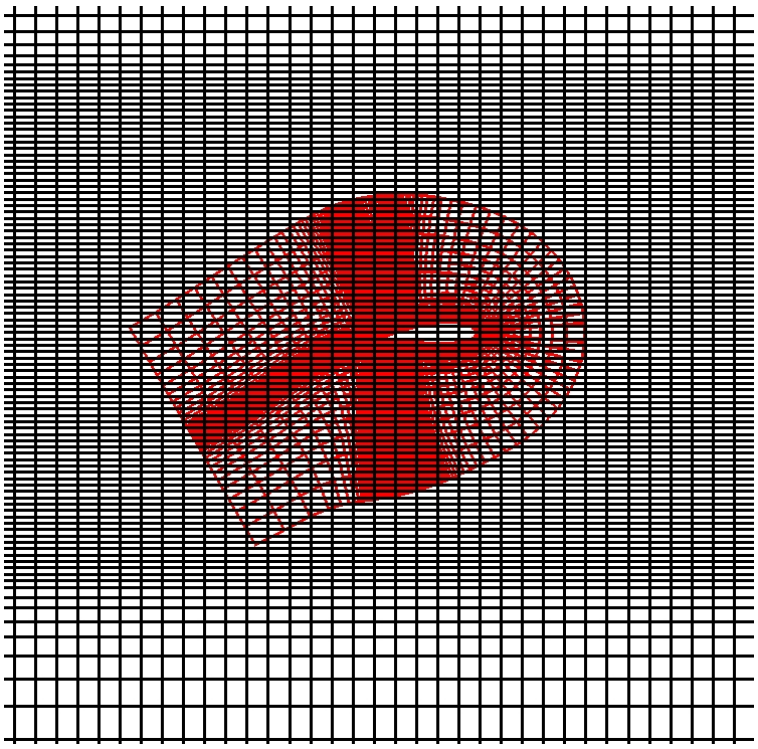

Figure 2.2: C mesh around an airfoil overlapping with background Cartesian mesh.

the governing equations. A hole is cut in the Cartesian grid in the region where the finer near body mesh (airfoil mesh) is available. Since this hole is cut in the Cartesian grid, an inner boundary is generated in the Cartesian mesh, so the points on this inner boundary need to obtain the information necessary for solving the governing equations. These points receive information from the airfoil mesh. There is an overlapping region between the Cartesian mesh and the airfoil mesh, which ensures smooth transfer of information among them. A minimum of two cell overlap is maintained in the present work, although five cell overlap is shown in this example. Special terms have been coined for these boundary points. The boundary points on the outer surface of the airfoil mesh are called chimera boundary points [52, 53] and the newly generated inner boundary points as a result of hole cutting on the Cartesian mesh are called hole fringe points. Accurate computation of the hole fringe points is very important in this technique in order to prevent any contamination of the solution.

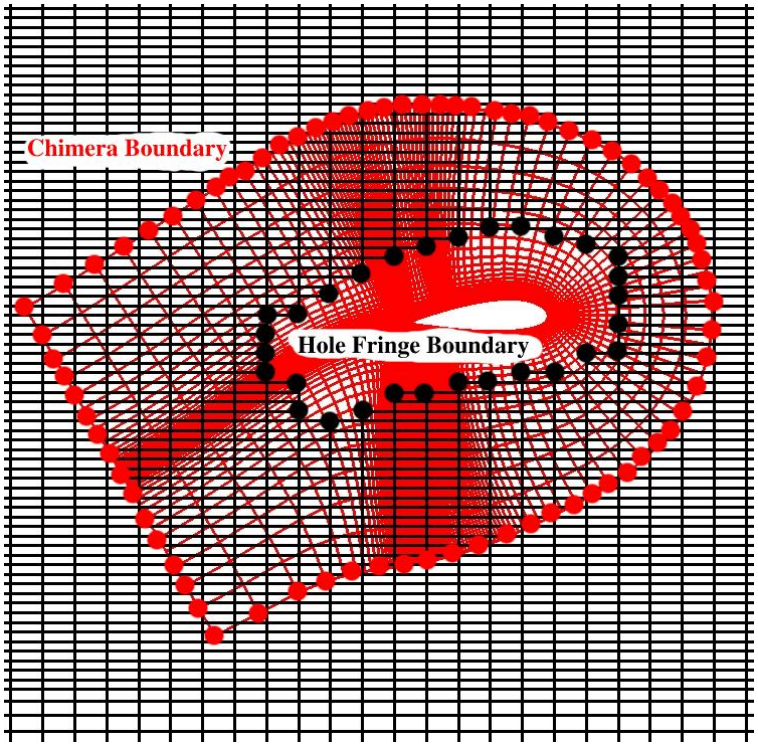

Figure 2.3: Close up of the hole cut in the background Cartesian mesh with the overlapping airfoil mesh.

In the surface normal vector method, adopted for hole cutting, a Cartesian box is generated around each cutting surface depending on the minimum and maximum spatial locations of the points on the cutting surface and only points in this box are tested for hole cutting. The algorithm adopted for hole cutting is shown in Figure 2.4. The test done on each point inside the Cartesian box is better described in Figure 2.5. The test to check whether a point lies inside or outside a cutting surface is based on the dot product of the outward surface normal and the vector joining the point to be tested and a point on the surface (a-b from Figure 2.5). This test should be conducted for all the points which need to be tested for hole cutting. It can be shown that the computational time required for this method is proportional to the product of total number of points tested and number of points that define the cutting surface.

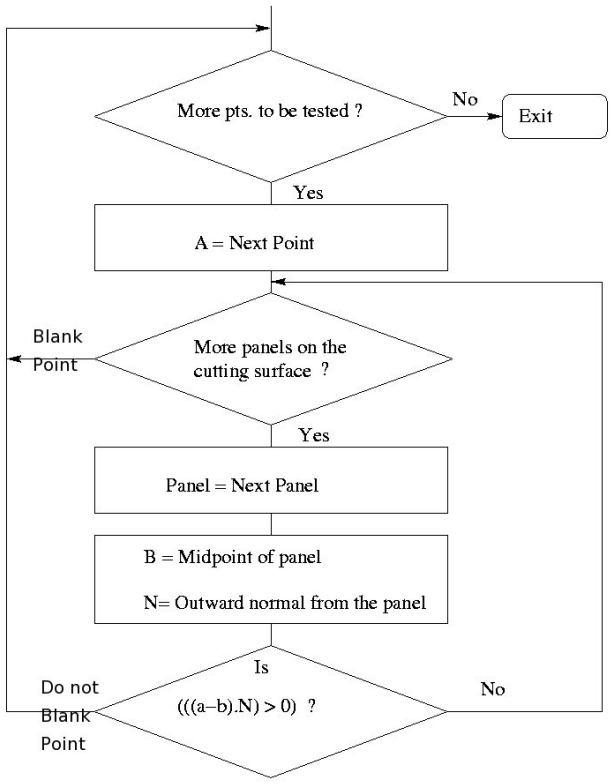

Figure 2.4: Flowchart showing the algorithm adopted for hole cutting.

The above example only illustrates the case with two overlapping grids. More complicated strategies are required in the case of multiple grid overlap. In the present work, the grids are arranged in a priority list, depending on the average cell volumes of the grids. The finest grid is chosen for the calculations done by the flow solver and the rest of the grids in that region are blanked out. An iblank array is constructed, with values 0 or 1 for each point depending on the status of the point, whether it is blanked or not.

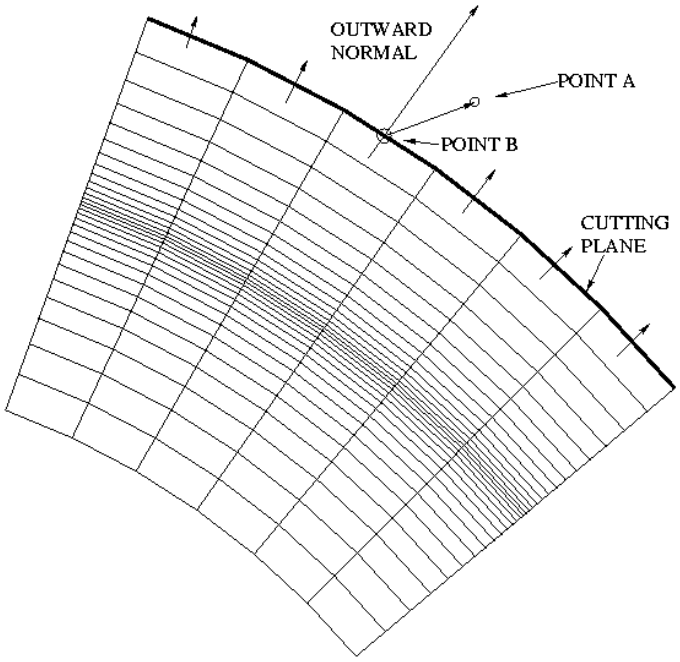

Figure 2.5: Test for a point A, whether inside or outside the hole.

2.2.2 Donor Cell Search

After hole cutting, the next task is to find the donor cells for the chimera boundary points in the near body meshes and hole fringe points on the background mesh. Conservative state variables and turbulent viscosity are interpolated from these donor cells on to the chimera boundary points or hole fringe points depending on the location of the chimera boundary point in the donor cell. A smart searching technique is used to search the donor cells for these boundary points. An arbitrary donor cell is selected, and then the next guess for the donor cell is made based on the direction in which the chimera boundary point lies, finally ending at the correct donor cell. The direction in which the chimera point lies can be easily

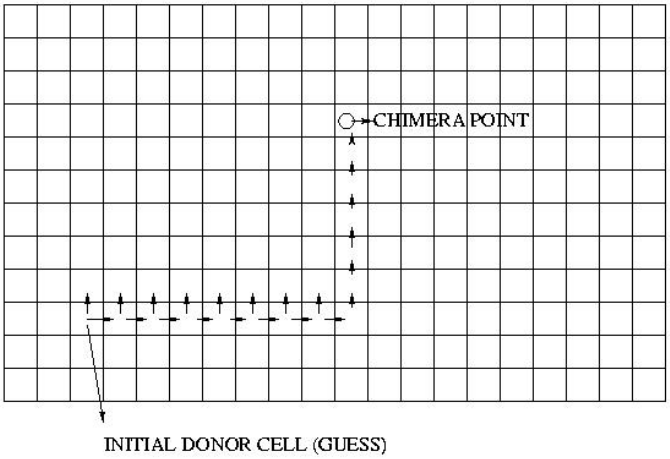

Figure 2.6: A typical search path adopted to find the donor cell for a chimera boundary point.

found out by taking the dot product of the vector joining the midpoint of the face to the chimera point and the surface normal of the face (similar to surface normal method). If the dot product is positive, the direction of search is the direction of the outward norm l from the face. A typical search path adopted is shown in Figure 2.6. This search ensures fast convergence, because an orthogonal search path is followed. This search technique can be accelerated if cell jumping is followed instead of cell walking. The terms cell jumping and cell walking are self explanatory. Special care should be taken when the donor grid is not a Cartesian grid, but a periodic or a C grid. In such cases, relations have to developed in the preprocessor between the boundaries at the overlapping C section or periodic boundary.

Linear interpolation factors are then calculated by solving tri-linear polynomials to interpolate the conservative variables using the donor cell points. Cubic interpolation between the grids will be incorporated in the future, which will enable information transfer with higher accuracy [59]. The cubic interpolation is observed to improve the solution in flows which involve shocks running across the chimera boundary. Such sharp gradients are not present in the current problem. The spatial co-ordinates of the chimera boundary point are expressed as a linear combination of the spatial co-ordinates of the corners of the donor cell. The tri-linear polynomials thus achieved are given below in Equation 2.1. The location of the chimera boundary point inside donor cell is shown in Figure 2.7. These represent three equations for the three spatial co-ordinates. The solution for the interpolation factors, ξ, η and ζ, is obtained using modified Newton Raphson Method on these 3 equations, which is described below in Figure 2.8. Newton Raphson method is a gradient based method and is very sensitive to the initial condition. In the modified Newton Raphson method a relaxation is applied to the corrections. This under relaxation prevents the corrections from increasing in an unbounded manner and divergence of Newton Raphson method. The initial guess required for Newton Raphson method is provided by computing the volumes of the parallelopips enclosed by the interpolated point and the faces along the three principal directions. The ratios of these volumes with the total volume of cell are used as initial guesses for ξ, η and ζ. The conservative variables and turbulent viscosity are interpolated on the chimera boundary points using these interpolation factors. This interpolation is expressed in equation 2.2. This is exactly the same as the interpolation of the spatial co-ordinates.

$$\begin{aligned} x_i(P) = {} & x_{1i} + (x_{2i} - x_{1i})\xi + (x_{4i} - x_{1i})\eta + (x_{5i} - x_{1i})\zeta \\ & + (x_{1i} - x_{2i} + x_{3i} - x_{4i})\zeta\eta \\ & + (x_{1i} - x_{2i} - x_{5i} + x_{6i})\xi\zeta + (x_{1i} - x_{4i} - x_{5i} + x_{8i})\eta\zeta \\ & + (x_{2i} - x_{1i} - x_{3i} + x_{4i} + x_{5i} - x_{6i} + x_{7i} - x_{8i})\xi\eta\zeta \end{aligned} \tag{2.1}$$

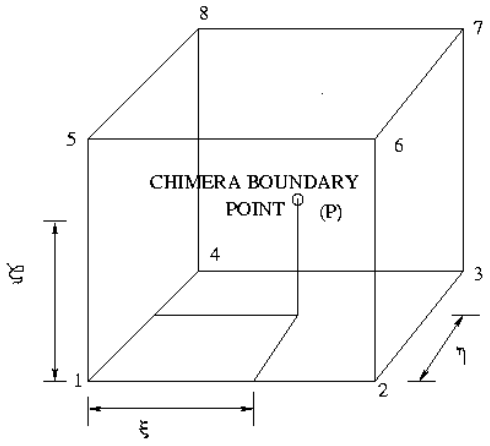

Figure 2.7: Interpolation factors for a chimera boundary point.

$$
\begin{aligned}
Q_i(P) = {} & Q_{1i} + (Q_{2i} - Q_{1i})\xi + (Q_{4i} - Q_{1i})\eta + (Q_{5i} - Q_{1i})\zeta \\
& + (Q_{1i} - Q_{2i} + Q_{3i} - Q_{4i})\zeta\eta \\
& + (Q_{1i} - Q_{2i} - Q_{5i} + Q_{6i})\xi\zeta + (Q_{1i} - Q_{4i} - Q_{5i} + Q_{8i})\eta\zeta \\
& + (Q_{2i} - Q_{1i} - Q_{3i} + Q_{4i} + Q_{5i} - Q_{6i} + Q_{7i} - Q_{8i})\xi\eta\zeta
\end{aligned} \tag{2.2}
$$

This discussion clearly defines the communication strategy employed between grids to obtain a consistent solution for several meshes. The steps involved to obtain connectivity information were explained and will be used to obtain such connectivity information for the QTR.

2.3 Navier Stokes Equations

The flow around a QTR is predominantly at low speeds and is highly separated below the wings. The highly viscous nature of flow separation necessitates the need for solving Navier

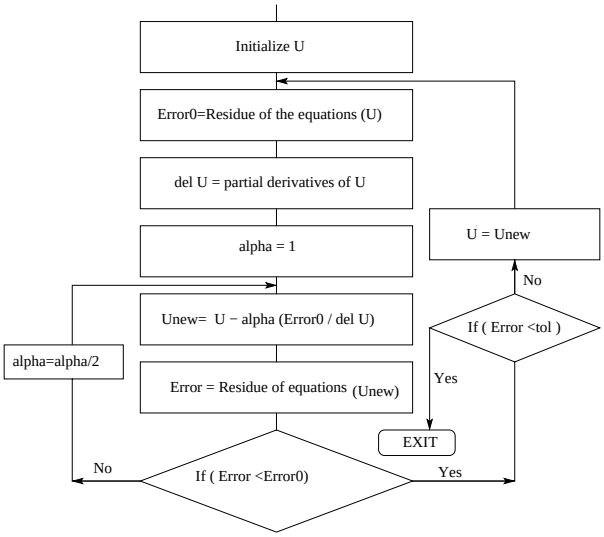

Figure 2.8: Flow chart showing modified Newton Raphson Method.

Stokes equations. In the current framework, the rotor is not modeled as a set of rotating blades, but as body forces acting across the rotor plane. These body forces account for the axial and tangential acceleration imparted to the fluid across the rotor plane. The compressible Navier Stokes equations with body forces in Cartesian co-ordinates are employed to solve the current problem and are given by:

$$\frac{\partial Q}{\partial t} + \frac{\partial E}{\partial x} + \frac{\partial F}{\partial y} + \frac{\partial G}{\partial z} = S \qquad \text{in } \Omega \tag{2.3}$$

where Q is the state vector, E, F and G are the flux vectors, and S is the source term vector. These vectors are given below:

$$Q = \left\{ \begin{array}{c} \rho \\ \rho u \\ \rho v \\ \rho w \\ e \end{array} \right\} \tag{2.4}$$

$$E = \left\{ \begin{array}{c} \rho u \\ \rho u^2 + p - \tau_{xx} \\ \rho uv - \tau_{xy} \\ \rho uw - \tau_{xz} \\ uH - u\tau_{xx} - v\tau_{xy} - w\tau_{xz} + k\frac{\partial T}{\partial x} \end{array} \right\} \tag{2.5}$$

$$F = \left\{ \begin{array}{c} \rho v \\ \rho uv - \tau_{xy} \\ \rho v^2 + p - \tau_{yy} \\ \rho uw - \tau_{yz} \\ vH - u\tau_{xy} - v\tau_{yy} - w\tau_{yz} + k\frac{\partial T}{\partial y} \end{array} \right\} \tag{2.6}$$

$$G = \left\{ \begin{array}{c} \rho w \\ \rho uw - \tau_{zx} \\ \rho vw - \tau_{zy} \\ \rho w^2 + p - \tau_{zz} \\ wH - u\tau_{xx} - v\tau_{xy} - w\tau_{xz} + k\frac{\partial T}{\partial z} \end{array} \right\} \tag{2.7}$$

$$S = \left\{ \begin{array}{c} 0 \\ f_x \\ f_y \\ f_z \\ uf_x + vf_y + wf_z \end{array} \right\} \tag{2.8}$$

In these definitions, ρ is the density, (u, v, w) and (f_x, f_y, f_z) are the Cartesian velocity and body force components in the directions (x, y, z), respectively. The quantity e is the total energy per unit volume, τ_{ij} are the stress terms and H is the stagnation enthalpy per unit volume. The quantity k is the coefficient of thermal conductivity and T is the static temperature. The pressure (p) is determined by the equation of state given by:

$$p = (\gamma - 1)\left\{ e - \frac{1}{2}\rho(u^2 + v^2 + w^2) \right\} \tag{2.9}$$

and the stagnation enthalpy is given by

$$H = e + p \tag{2.10}$$

where γ is the ratio of specific heats. Huge resources are required to solve the Navier Stokes equations. An averaging over time as suggested by Reynolds, leads to Reynolds Averaged Navier Stokes equations. A further approximation suggested by Boussinesq, which relates the turbulent viscosity to the Reynolds stresses was also applied. The resulting expression for shear stress (τ_{xy}) after these two approximations can be written as :

$$\tau_{xy} = (\frac{\mu + \mu_t}{2})(\frac{\partial u}{\partial y} + \frac{\partial v}{\partial x}) \tag{2.11}$$

where μ is the laminar viscosity and μ_t is the turbulent viscosity. The product of turbulent viscosity with the velocity gradients represent the Reynolds stresses. Laminar viscosity can be evaluated using simple algebraic Sutherland's Law [35], but the evaluation of turbulent viscosity is not trivial. Various turbulence models, which aim at obtaining the turbulent viscosity field have been developed in the past. They will be discussed in the next section.

The Navier Stokes equations are transformed from the physical generalized curvilinear domain to a uniformly spaced Cartesian domain. This transformation was discussed previously. After transforming, the Navier Stokes equations can be written in the computational space as:

$$\frac{\partial \hat{Q}}{\partial \tau} + \frac{\partial \hat{E}}{\partial \xi} + \frac{\partial \hat{F}}{\partial \eta} + \frac{\partial \hat{G}}{\partial \zeta} = \hat{S} \qquad \text{in } \Omega \tag{2.12}$$

where the vector of conservative quantities $\hat{Q} = \frac{1}{J}Q$ (J was defined previously as the Jacobian of the transformation) and the flux contributions are now defined with respect to the computational cell faces by :

$$\hat{E} = \frac{1}{J}\left(\frac{\partial \xi}{\partial x}E + \frac{\partial \xi}{\partial y}F + \frac{\partial \xi}{\partial z}G\right) \tag{2.13}$$

$$\hat{F} = \frac{1}{J}\left(\frac{\partial \eta}{\partial x}E + \frac{\partial \eta}{\partial y}F + \frac{\partial \eta}{\partial z}G\right) \tag{2.14}$$

$$\hat{G} = \frac{1}{J}\left(\frac{\partial \zeta}{\partial x}E + \frac{\partial \zeta}{\partial y}F + \frac{\partial \zeta}{\partial z}G\right) \tag{2.15}$$

$$\hat{S} = \frac{1}{J}S \tag{2.16}$$

These partial differential equations are solved for the conservative variables, $\hat{Q}$, in the given discretized domain using a compressible Reynolds Averaged Navier Stokes solver. These partial differential equations are solved on the curvilinear structured meshes and it is necessary to specify a set of boundary conditions in order to obtain a unique solution on the structured mesh system. This specification of boundary conditions was described in detail in the overset technique section.

2.4 Turbulence Modeling

For closure of the Navier Stokes Equations, it is necessary to calculate the turbulent viscosity in addition to the conservative variables. Various models have been developed to obtain the solution of turbulent viscosity. The models range from zero equation algebraic turbulence models (Baldwin Lomax [36]), four equation turbulence models ($v^2 - f$ model [37]) to Reynolds Stress models. The zero equation model developed by Baldwin and Lomax calculates the turbulent viscosity as an algebraic function of the conservative variables. On the other hand, $v^2 - f$ model by Durbin [37] solves four differential equations to obtain four scalar field variables (k, ϵ, v^2 and f). The turbulent viscosity is obtained as an algebraic function of these four variables. The computational time to obtain the turbulent viscosity will be considerably higher for the four equation model as opposed to the zero equation algebraic model.

2.4.1 Choice of Turbulence Model

It was fairly trivial to choose a turbulence model apt for the current application. Algebraic models like Baldwin Lomax turbulence model are essentially valid for attached flows and are boundary layer models in spirit. These models have poor accuracy while modeling massive separated flows which is an integral part of the current problem. The flow in the wake of the wings is highly separated and cannot be accurately modeled using algebraic models. In hover out of ground effect, the point of separation will be predicted accurately using this model, but the base pressure (at the bottom surface) will not be correct, because of incorrect turbulent viscosity in the turbulent wake below the wing, resulting in incorrect download prediction. The second option of using two equation $k - \epsilon$ model was also declined because of their applications. These models are much more difficult to use and require even finer grids, because of the strong production terms added in the boundary layer. They are more suited for wall-bounded flows, where the production terms (turbulence) are not too large and have not been extensively used for external flows. Modeling of massively separated flow is questionable using these models. The solution is highly dependent on the turbulence levels present in the free stream and is also observed to diffuse rapidly if a fine grid is not used even in the far-field. The four equation model (v^2-f) was declined because of extra equations being solved. Among the one equation turbulence models Spalart Allmaras Turbulence model [38] is the most widely used completely validated model available. This model was built with several applications in mind and each term in the model has been calibrated. This model has been used to model flow past solid bodies and suitable comparisons have been obtained with experiments [38]. It has been used in simulating separated external flows accurately in different numerical codes [40, 42]. The ability of this mature turbulence model to accurately model separated flows with low overhead costs was the driving force for choosing this turbulence model.

This model is a simplified version of the commonly used 2 equation $k - \epsilon$ model and is given by:

$$\frac{D\nu_t}{Dt} = c_{b1}S\nu_t + \frac{1}{\sigma}[\bigtriangledown.(\nu_t \bigtriangledown \nu_t + c_{b2}(\bigtriangledown\nu_t)^2)] - c_{w1}f_w[\frac{\nu_t}{d}]^2 \tag{2.17}$$

where ν_t is the turbulent eddy viscosity, c_{b1}, c_{b2} and c_{w1} are constants, d is the distance from the wall and f_w is a function of distance from the wall. This differential equation is solved independently and the additional field variable turbulent viscosity (ν_t) is obtained as a solution. The shear stress in the momentum and energy equations is evaluated once turbulent viscosity is calculated and hence closure is achieved. Characteristic boundary condition is applied at the far field and turbulent viscosity is set to zero at the wall. More details about the turbulence model can be found in original work by Spalart and Allmaras[38]. This model was implemented in the code and several validations were obtained by Eric Schroeder [41].

2.5 Rotor Model

Each rotor system is modeled by adding source terms (body forces) to the momentum and energy equations similar to the modifications to OVERFLOW [54] by Chaffin and Berry [60]. Similar rotor models have also been developed by Rajagopalan et al. [61] and Tadghighi [63]. The model developed by Tadghighi is not time averaged and can be applied to simulate unsteady phenomena in the rotor wake. The ambitious goals of this model are foiled by the inaccuracies involved in the evaluation of the aerodynamic coefficients at various span wise locations which do not account for three dimensional effects.

In the current model, the rotors are treated as actuator disks (axial plane in the cylindrical grid), across which lift and drag forces are calculated as a function of radial and azimuthal locations, using blade element theory and augmented as source terms in the Navier Stokes equations, described in equation 2.8.

2.5.1 Blade Element Theory

The blade element theory provides accurate estimate of the radial and azimuthal distribution of blade loading using simple quasi steady two dimensional lift and drag information.

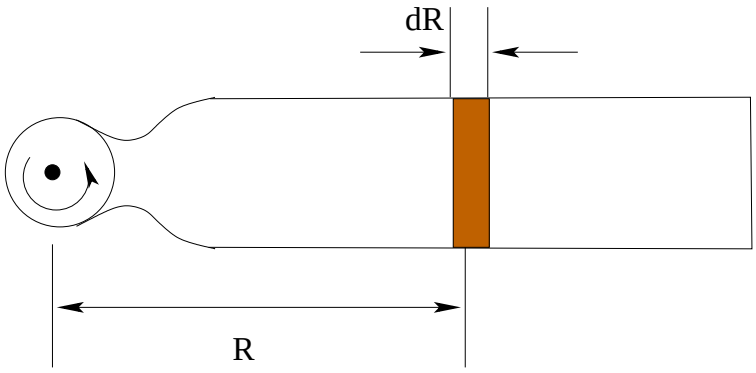

Figure 2.9: Blade discretization along the radius.

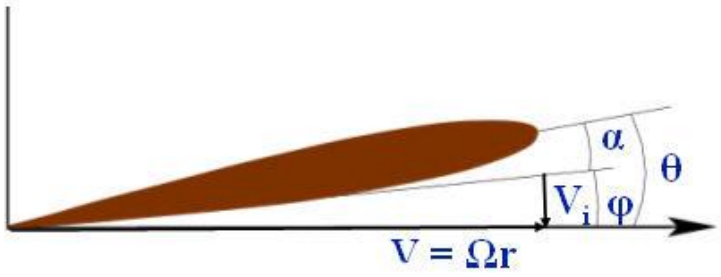

Figure 2.10: Sectional forces on an airfoil.

Along with a mapping of two dimensional force coefficients from effective angles of attack, blade element analysis requires the variation of induced velocity in the rotor plane for calculating the effective angles of attack. The forces on the blades can be calculated using two dimensional airfoil aerodynamics. These forces, then can be integrated to obtain thrust and moments on the rotor.

In this approach, the blade is discretized along the span and forces are calculated on each span wise location. The discretization along the span is shown in Figure 2.9. The aerodynamic lift and drag at these discretized span wise locations are computed using simple analytical models given in equations 2.18 and 2.19.

$$dL = \frac{1}{2}\rho v^2 C_l c dR \tag{2.18}$$

$$dD = \frac{1}{2}\rho v^2 C_d c dR \tag{2.19}$$

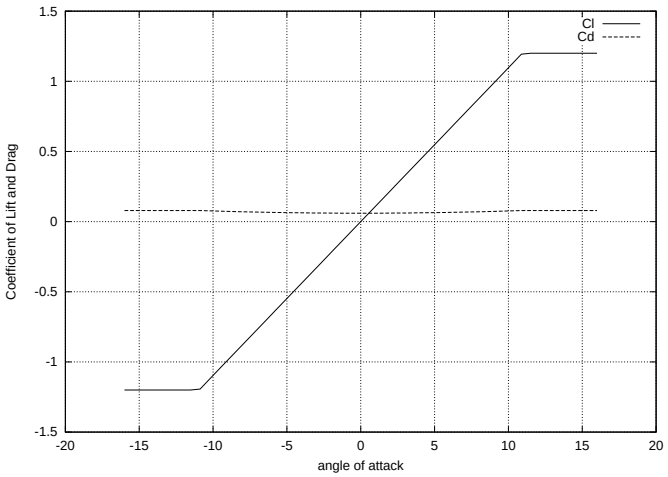

Figure 2.11: Variation of lift and drag coefficients with angle of attack.

where v is the in-plane velocity, c is the chord length, dR is the span wise length of the cell, and C_l and C_d are the coefficients of lift and drag, respectively.

Coefficient of lift and drag are approximated using the angle of attack of the section, which is better illustrated in Figure 2.10, using a simple thin airfoil model. It can be noted from the figure that the angle of attack for a section is given by the difference between the geometric angle of attack (θ) and induced angle of attack (ϕ). The induced angle of attack is calculated as the arc tangent of (V_i/V) and the geometric angle of attack is specified by the twist of the blade. Glauert correction is then applied to account for the compressibility effects due to Mach number at all the span wise locations.

As already mentioned, some approximation for the lift and drag coefficients is necessary in this approach in order to calculate the thrust and moments produced by the rotor. The variation of lift and drag coefficients is shown in Figure 2.11. The airfoil section was assumed be that of NACA-0012 airfoil. A linear variation of lift coefficient with angle of attack is assumed until the airfoil stalls, after which the stalling C_l is maintained. Drag coefficient only represents the profile drag contribution (C_{do}). More accurate models could be incorporated using airfoil test data, but this simple model is deemed sufficient at this stage.

Once, the lift and drag distributions are calculated using quasi two dimensional analysis, the lift and drag on each blade can be integrated to calculate the thrust and power of the rotor. Thrust and power are given by the following expressions.

$$Thrust = N_b \int_0^R dL \tag{2.20}$$

$$Power = N_b \int_0^R r dD \tag{2.21}$$

It can be inferred from the discussion above that if velocities in the plane of the rotor are provided to blade element theory along with simplified lift and drag coefficient variation with angle of attack and geometrical properties of the blade, lift and drag distribution can be calculated using blade element theory. Among the inputs to blade element theory, geometrical properties of the blades and airfoil characteristics are a property of the rotor and are available with the rotor. Approximation of velocities at the rotor plane is more involved. Momentum theory can be employed to find the induced velocity, which assumes a constant downward velocity through out the rotor plane as a function of rotor disk loading. CFD is employed in the current methodology to obtain the velocity distribution at the rotor plane.

2.5.2 BET Coupling with CFD

Another alternative for modeling the velocities in the plane of the rotor is CFD. In this approach, blade element theory receives the velocity distribution from CFD and calculates the force distribution at the rotor plane. This force distribution is defined for individual blades and varies with the azimuthal location, because of the variation of the induced velocities at the rotor plane.

The rotor is not modeled as a set of blades rotating in the rotor plane, but instead as a disk in a cylindrical mesh and ignores the effect of individual blades. Hence, these aerodynamic forces on the blade sections are scaled in the azimuthal direction by multiplying them by the solidity of rotor. This averaging scales down the forces on each azimuthal section, but

still preserves the variation of forces along the azimuth. The rotor model is a time averaged model, because it ignores the position of the blades at a particlar time, and instead averages the forces over time.

From the CFD perspective, the flow field around a rotor is three dimensional and hence a three dimensional grid is necessary to simulate the rotor flow field. A cylindrical grid is employed to model the rotor, in which part of an axial plane is represents the rotor. The rotor plane is discretized in the radial and the azimuth direction for CFD. The rotor plane in a cylindrical boundary along with representative velocity vectors is shown in Figure 2.12. Once, the time averaging of forces is done, each cell on the rotor plane experiences the aerodynamic forces. These lift and drag forces on the cells are appropriately transformed to F_x, F_y and F_z, and augmented as source terms in the Momentum and Energy Equations for corresponding cells (Finite Volume Approach), by accurately accounting for twist, collective and cyclic pitch of the blades. Blades are assumed to be rigid with no flapping in this model, so errors in the transformation of lift and drag to F_x, F_y and F_z, due to the flexible nature of the blades are ignored. There is no need for non-dimensionalization of the source terms F_x, F_y and F_z, because all the quantities (density and velocities) used to calculate these forces are non-dimensionalized. After 10 iterations of CFD, the flow field is modified based on the aerodynamic forces experienced by the finite volumes in the grid. The velocity field calculated as a result is again given back to blade element theory, which calculates the forces on the blades and hence completing the coupling loop.

The rotor model algorithm is shown in Figure 2.13. The flow chart shows two loops in the algorithm. The right side loop is the coupling loop between blade element theory and CFD, where as the left side loop is the trim loop. This trim loop adjusts the collective pitch if a particular thrust is desired by the rotor. It can also adjust the cyclic pitch if zero longitudinal and lateral moments are desired at the rotor hub. Constant collective and cyclic pitch condition can also be simulated in which case the trim loop is not encountered.

The sectional forces in the normal direction, thus computed at different radial and azimuthal locations, are integrated over the whole disk to obtain the resulting thrust. Inte-

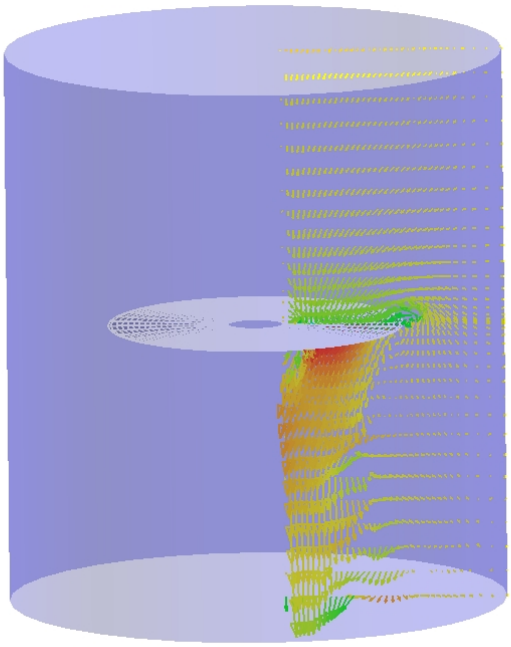

Figure 2.12: An axial plane in the cylindrical grid which represents the rotor disk.

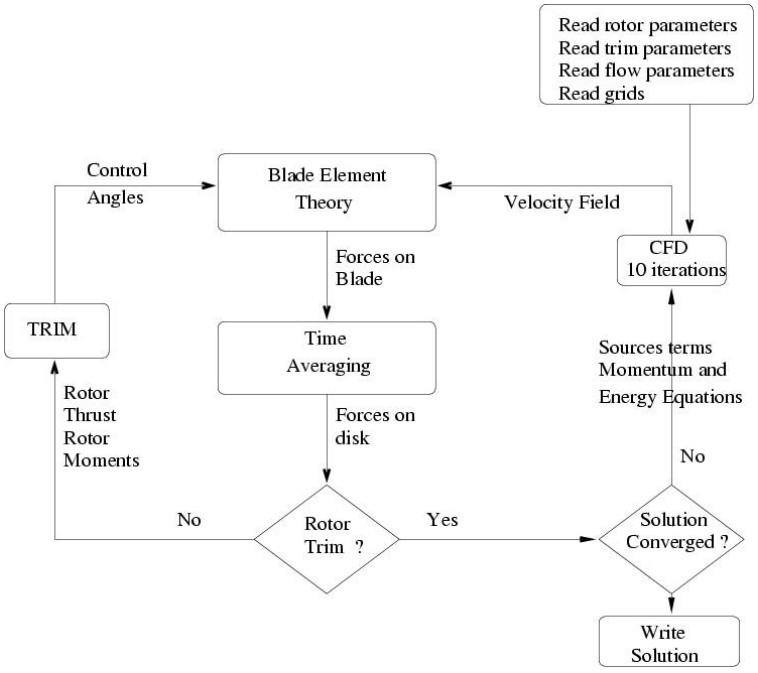

Figure 2.13: Flow chart of rotor model algorithm.

grating the moment of the drag forces over the disk gives the profile power for the rotor. Appropriate non-dimensionalization is done to arrive at the thrust and power coefficients.

2.5.3 Rotor Trim

The most important benefit of the rotor model is its ability to obtain rigid trim for the rotor without modifying the grids during run time. Thrust produced by the rotor is directly proportional to the collective pitch introduced in the rotor. Hence, to simulate the rotor operating at a constant thrust and tip speed, collective pitch is iterated to obtain the appropriate collective setting.

Zero lateral and longitudinal moments at the rotor hub can also be obtained using the rotor model. This is done by dividing the rotor disk into four quadrants and calculating the thrust contributions from these quadrants. These contributions to thrust can be seen in Figure 2.14. Both lateral (θ_{1c}) and longitudinal (θ_{1s}) cyclic pitch control is necessary to cancel the moments at the rotor hub. In the current model, longitudinal moment imbalance, resulting from (T2+T3-T1-T4) is balanced by introducing longitudinal cyclic pitch (θ_{1s}), which would aim at reducing (T2+T3-T1-T4). Similarly, lateral moment imbalance, resulting from (T1+T2-T3-T4) is balanced by lateral cyclic pitch (θ_{1c}). To obtain longitudinal trim, θ_{1s} is iterated until (T2+T3-T1-T4) is reduced below the tolerance. Similarly, lateral trim is obtained by iterating θ_{1c} until (T1+T2-T3-T4) reduces below the tolerance.

The corrections in control angles for the iterative trim loop are obtained using gradient method (Newton Raphson).

$$\theta_{new} = \theta_{old} - f(\theta_{old}) / \frac{\partial f(\theta_{old})}{\partial \theta_{old}} \tag{2.22}$$

where f = (T2+T3-T1-T4) and $\theta = \theta_{1s}$ for longitudinal trim and f = (T1+T2-T3-T4) and $\theta = \theta_{1c}$ for lateral trim. The derivative of the function is obtained numerically using finite difference method.

This trimming loop is applied in all flight conditions. It balances the longitudinal and lateral moments for each rotor and aids in obtaining a symmetric inflow profile over the four

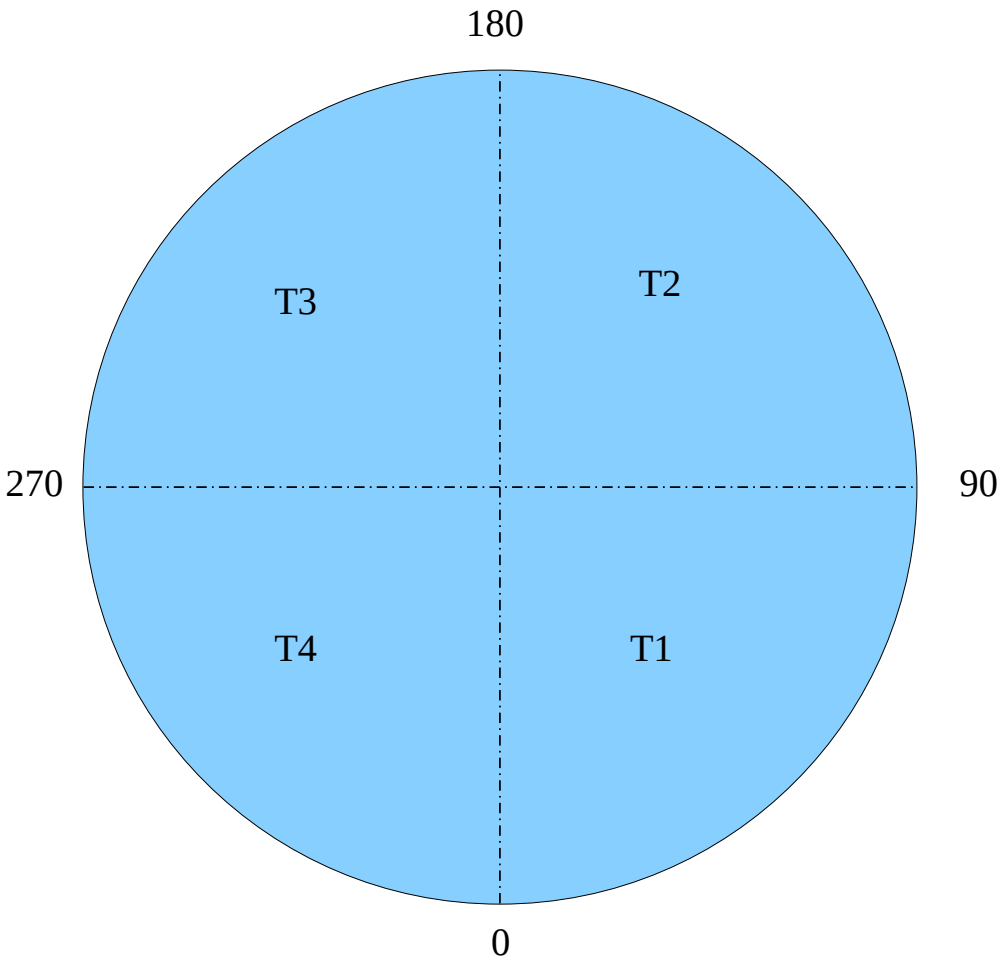

Figure 2.14: Contributions to thrust by different quadrants.

quadrants (induced velocity proportional to thrust). For such a configuration, the flapping of the rotor blades will be very small and can be neglected. This completes the discussion on the rotor model employed in the compressible solver sufficient to model the four rotors of the Quad Tilt Rotor in various flight conditions.

2.6 Solution Algorithm

Various algorithms have been utilized in the past to solve the Navier Stokes equations. The flux terms, E, F and G in the Navier Stokes equations are a combination of inviscid and

viscous fluxes, which are completely different in nature (hyperbolic versus elliptic). As a consequence, the inviscid and viscous fluxes are modeled differently. In the current work, the baseline code Transonic Unsteady Rotor Navier Stokes (TURNS) flow solver is modified to simulate the flow over the QTR.

2.6.1 TURNS

This flow solver was originally written by Srinivasan and Baeder [73]. This code was tailored to simulate flow over a wing or a hovering rotor using Field Velocity approach [74]. This code solves the governing equations on a single structured grid. It employs a finite volume approach, which is described next.

The differential equation 2.12 can be discretized in space and time in a finite volume approach. In this approach, fictitious volumes are created around each grid point. A fictitious volume is created around a point indexed by (j, k, l) using the midpoints of the lines joining the adjacent grid points to the grid point (j, k, l). This fictitious volume around point (j, k, l) is shown in Figure 2.15. The faces of this new volume lie exactly in the middle of two grid points. This volume is treated as a control volume and fluxes are evaluated at the faces of the volume, resulting in conservation equations for the volume. Calculation of only inviscid fluxes is described here. The viscous fluxes are calculated using a central difference discretization and are presented in Appendix A. Since, the faces of the control volume do not coincide with the grid points, where the conservative variables are stored or calculated, some interpolation scheme (reconstruction) is required to provide a mapping from the conservative variables stored at grid points to fluxes at the cell faces. Extensive research has been done on these reconstruction procedures. These reconstruction schemes are desired to have some special properties for better numerical accuracy without generation of spurious oscillations. In the baseline TURNS solver, Monotone Upstream-Centered Scheme for Conservation Laws (MUSCL) [43] is employed for reconstruction of fluxes.

The first step for reconstruction is the evaluation of the left state and the right state at the interface. The left and right states are more meaningful from Figure 2.16. It can be seen

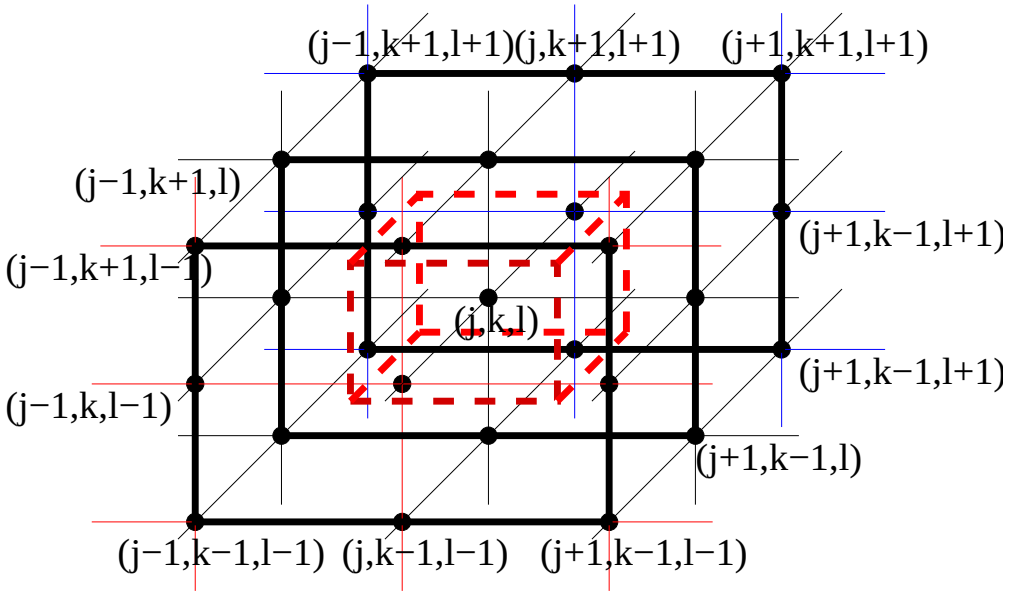

Figure 2.15: Fictitious volume at (j,k,l).

from the figure that left and right state are calculated at the interface $(j + 1/2)$ using the reconstruction in cell j and $j + 1$. The order of accuracy of the evaluation of the left and right states is governed by the stencil used (number of neighboring points). Piece wise cubic reconstruction with Koren's limiter [44] is used in the baseline TURNS. Limiting prevents generation of a new extrema while reconstruction and it drops the accuracy to first order when it encounters sharp discontinuities.

After evaluation of the left and right states at the cell interface, the next step is to calculate the fluxes at the interface. Upwind schemes are utilized to find the inviscid fluxes at the interface. Euler equations in one dimension are composed of three waves with wave speeds given be u, u+a and u-a (Figure 2.17). The left and right states can be multiplied by the flux Jacobian to obtain the left and right fluxes. These fluxes are split into plus (F^+) and minus (F^-) depending on their contributions to the left and right running waves. Part of the flux which contributes to the right running wave is referred to as F^+ and the part which contributes to the left running wave is referred to as F^-. Therefore, for the illustration in Figure 2.17, since two waves are right running at the interface and one is left running, F_L^+

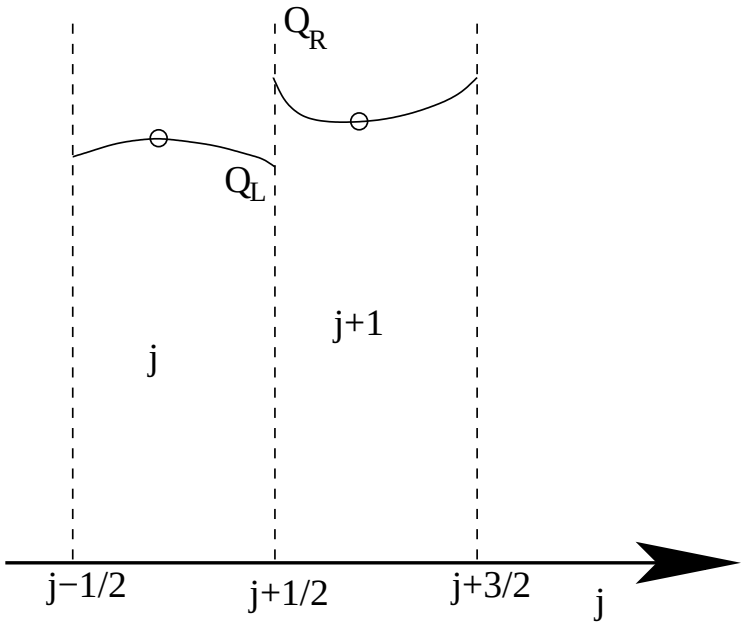

Figure 2.16: Evaluation of Q at $(j + 1/2)$ using the left and right states.

contributing to the right running waves (2 in number) should be used and F_R^- contributing to the left running wave (1 in number) should be used. There are several ways in which these F^+ and F^- can be calculated [46, 47]. The approach adopted by Steger-Warming [46] is a wave splitting approach and is observed to be unphysical close at sonic points, because of the lack of derivative continuity across sonic points. Van Leer [47] approach rectifies this drawback by choosing Mach numbers for splitting the fluxes and achieving continuity of flux derivative at sonic points. Roe upwinding [45] has been implemented in the original TURNS solver. Roe upwinding utilizes the left and right states of the conservative variable at the interface and evaluates the flux at the interface. Original Roe upwinding scheme is observed to predict unphysical expansion shocks at sonic points and has been corrected by Harten [48] at sonic points. More details about Roe upwinding are provided in the next chapter.

The fluxes at the interfaces are shown in two dimensions for simplicity in Figure 2.18. It can be clearly seen from the figure that flux E is calculated in the j direction (ξ direction) at $(j - 1/2, k)$ and $(j + 1/2, k)$, while flux F is calculated in the k direction (η direction) at $(j, k - 1/2)$ and $(j, k + 1/2)$. Hence, the resultant flux in the cell is the vectorial sum of the

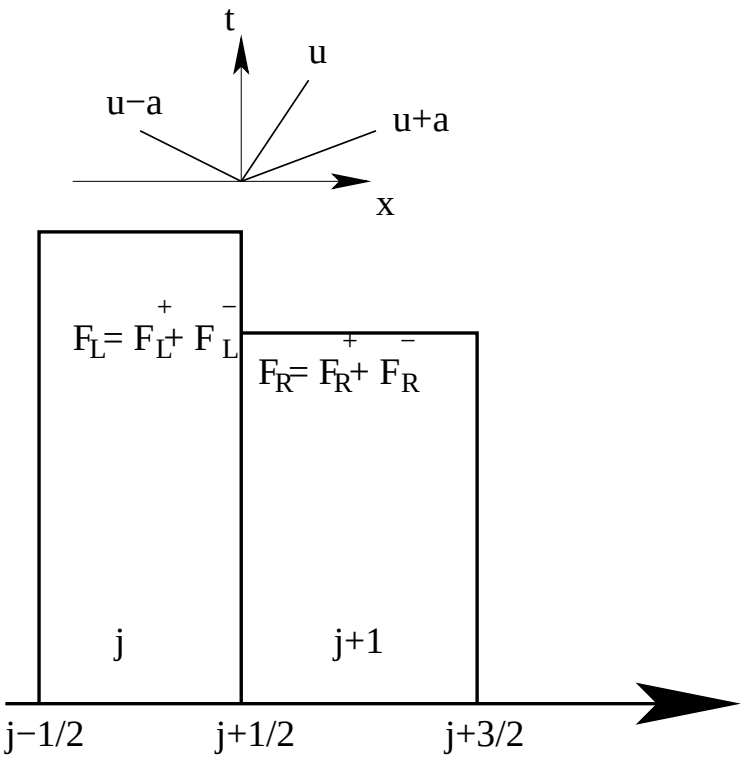

Figure 2.17: Demonstration of upwinding at the interface.

fluxes on each face and leads to an increase/decrease in the conserved quantity in the control volume. Hence, the equation 2.12 (in three dimensions) can be written as in a semi-discrete form as :

$$\frac{\partial \hat{Q}}{\partial \tau} = -\frac{\hat{E}_{j+1/2} - \hat{E}_{j-1/2}}{\Delta\xi} - \frac{\hat{F}_{k+1/2} - \hat{F}_{k-1/2}}{\Delta\eta} - \frac{\hat{G}_{l+1/2} - \hat{G}_{l-1/2}}{\Delta\zeta} + \hat{S}_{j,k,l} \tag{2.23}$$

The contribution from viscous fluxes and source terms should also be augmented to the right hand side, but there is no need to use upwinding to evaluate these contributions. These viscous flux contributions are dissipative in nature and do not follow hyperbolic convection laws and central differencing is used to obtain these viscous contributions. There are two types of viscous terms depending on complexity of calculations : Normal viscous terms and cross viscous terms. Normal viscous terms involve second derivative only in one direction ($F_{\xi\xi}$, $F_{\eta\eta}$ or $F_{\zeta\zeta}$), whereas cross viscous terms involve second derivative as a combination of two directions ($F_{\xi\eta}$, $F_{\eta\zeta}$ or $F_{\zeta\xi}$). Normal derivatives can be calculated by sweeping along

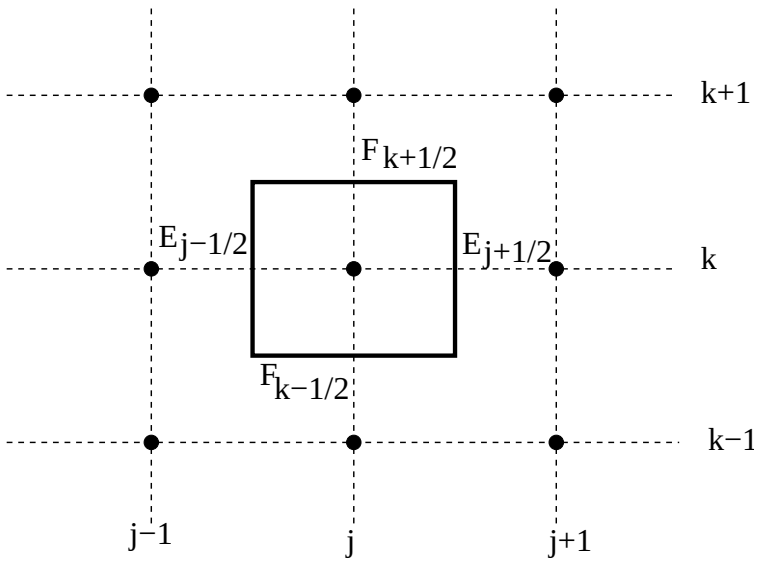

Figure 2.18: Flux calculation at cell interfaces.

normal lines, but sweeping along planes is necessary to calculate cross derivatives. The cross derivatives are very important in separated flows where sharp velocity gradients occur in streamwise direction (grid lines parallel to the surface). These terms are very similar to Reynolds stresses since they co-relate gradients of component of velocities in different directions. More details about modeling of the viscous terms is given in Appendix B. The source terms, added to the Momentum and Energy Equations because of the Rotor Model, do not involve any derivatives in space and can be added to the right hand side directly with ease. These terms do not require any linearized jacobians on the left hand side to increase the stability of the scheme.

Once, the right hand side of the equation is evaluated (including viscous fluxes and source terms), the conservative variables, Q are evolved in time. There are mainly two types of methods to evolve the solution in time, explicit and implicit. The explicit methods use only the information at the previous time step to calculate the conservative variables at the new time step, where as the implicit methods indirectly use information at the new time step and require inversion of large sparse matrices. Baseline TURNS code utilized Lower Upper Symmetric Gauss Siedel Scheme (LUSGS) [49, 50] as the implicit scheme.

If an index for time step is included in equation 2.24, the implicit scheme can be written as the following.

$$\frac{\partial \hat{Q}^{n+1}}{\partial \tau} = -\frac{\hat{E}^{n+1}_{j+1/2} - \hat{E}^{n+1}_{j-1/2}}{\Delta\xi} - \frac{\hat{F}^{n+1}_{k+1/2} - \hat{F}^{n+1}_{k-1/2}}{\Delta\eta} - \frac{\hat{G}^{n+1}_{l+1/2} - \hat{G}^{n+1}_{l-1/2}}{\Delta\zeta} + \hat{S}^{n+1}_{j,k,l} \tag{2.24}$$

In the equation above, all the quantities are desired at the new time step $(n+1)$, but the fluxes are not known at the $(n+1)$ time step, so there is a need for them to be linearized and expressed in terms of fluxes and conservative variables at step (n). The flux E, F and G in j, k and l directions can be linearized as:

$$\hat{E}^{n+1}_j = \hat{E}^n_j + \Delta\hat{E}^n_j = \hat{E}^n_j + \hat{A}\Delta\hat{Q}^n_j \tag{2.25}$$

$$\hat{F}^{n+1}_k = \hat{F}^n_k + \Delta\hat{F}^n_k = \hat{F}^n_k + \hat{B}\Delta\hat{Q}^n_k \tag{2.26}$$

$$\hat{G}^{n+1}_l = \hat{G}^n_l + \Delta\hat{G}^n_l = \hat{G}^n_l + \hat{C}\Delta\hat{Q}^n_l \tag{2.27}$$

where $\hat{A} = \frac{\partial \hat{E}}{\partial \hat{Q}}$, $\hat{B} = \frac{\partial \hat{F}}{\partial \hat{Q}}$ and $\hat{C} = \frac{\partial \hat{G}}{\partial \hat{Q}}$. The source terms can also be linearized with respect to the conservative variables.

If the linearized fluxes are substituted in equation 2.28, the equation can be written in δ form as :

$$[I+\Delta t(\frac{\bar{A}}{\Delta\xi}+\frac{\bar{B}}{\Delta\eta}+\frac{\bar{C}}{\Delta\zeta})]\delta\hat{Q}^n = \Delta t[-\frac{\hat{E}^n_{j+1/2} - \hat{E}^n_{j-1/2}}{\Delta\xi} - \frac{\hat{F}^n_{k+1/2} - \hat{F}^n_{k-1/2}}{\Delta\eta} - \frac{\hat{G}^n_{l+1/2} - \hat{G}^n_{l-1/2}}{\Delta\zeta} + \hat{S}^n_{j,k,l}] \tag{2.28}$$

where $\bar{A} = \frac{(\hat{A}\delta\hat{Q})_{j+1/2} - (\hat{A}\delta\hat{Q})_{j-1/2}}{\delta\hat{Q}_j} \simeq (\hat{A})_{j+1/2} - (\hat{A})_{j-1/2}$. Similarly $\bar{B}$ and $\bar{C}$ are defined. The approximation for $\bar{A}$ does not degrade the accuracy of the algorithm, because the left hand side is only used to accelerate the convergence by enabling choice of a larger time step, and does not have to be exact, but still needs to be a good conservative approximation. The left hand side is sparsely populated, but is still very expensive to invert in order to obtain a solution for $\delta\hat{Q}^n$. Further approximations are necessary for ease of inversion of the matrix without the loss of speed of convergence.

One such approximation is made in the LUSGS algorithm. In the LUSGS algorithm, the left hand side is factorized in to L, D and U matrices, which are lower diagonal, diagonal and upper diagonal matrices, respectively and can be written as.

$$LDU\delta\hat{Q}^n = -\Delta t[RHS^n] \tag{2.29}$$

where

$$L = I - \Delta t\hat{A}^-_{j,k,l} + \Delta t\nabla_\xi\hat{A}^+ - \Delta t\hat{B}^-_{j,k,l} + \Delta t\nabla_\eta\hat{B}^+ - \Delta t\hat{C}^-_{j,k,l} + \Delta t\nabla_\zeta\hat{C}^+ \tag{2.30}$$

$$D = I - \Delta t(\hat{A}^+ - \hat{A}^- + \hat{B}^+ - \hat{B}^- + \hat{C}^+ - \hat{C}^-)_{j,k,l} \tag{2.31}$$

$$U = I + \Delta t\hat{A}^+_{j,k,l} + \Delta t\Delta_\xi\hat{A}^- + \Delta t\hat{B}^+_{j,k,l} + \Delta t\Delta_\eta\hat{B}^- + \Delta t\hat{C}^+_{j,k,l} + \Delta t\Delta_\zeta\hat{C}^- \tag{2.32}$$

here $\Delta_\xi\hat{A}$ denotes $\hat{A}_{j+1,k,l} - \hat{A}_{j,k,l}$ and $\nabla_\xi\hat{A}$ denotes $\hat{A}_{j-1,k,l} - \hat{A}_{j,k,l}$. $\Delta_\eta\hat{B}$, $\Delta_\zeta\hat{C}$, $\nabla_\eta\hat{B}$ and $\nabla_\zeta\hat{C}$ are defined similarly. The matrix L consists of elements only at (j,k,l), $(j-1,k,l)$, $(j,k-1,l)$ and $(j,k,l-1)$. The diagonal of matrix is defined as (j,k,l), there fore all the element in the matrix L will lie on or below the diagonal (Lower diagonal matrix). Similarly, matrix U consists of elements at (j,k,l), $(j+1,k,l)$, $(j,k+1,l)$ and $(j,k,l+1)$, which lie at or above the diagonal (Upper diagonal matrix).

This does not clearly explain the ease of inversion of LDU matrices. The matrices $\hat{A}^+$ and $\hat{A}^-$ are defined as $1/2(A+\sigma_\xi)$ and $1/2(A-\sigma_\xi)$, respectively. σ is the spectral radius of matrix A, which simplifies the D matrix to a block diagonal matrix. Since D matrix is only a block diagonal matrix, it only requires a scalar inversion to invert this matrix. The other two matrices L and U can be easily inverted by a forward and a backward sweep. Hyperplanes are used in the TURNS code to accelerate the convergence by choosing an updated value for the linearization of fluxes.

2.6.2 Diagonalized Algorithm

The spectral radius approximation works fine for inviscid and moderately viscous problems, but once highly stretched meshes are involved in computations, convergence of LUSGS

method is delayed. Pulliam and Chaussee's [75] diagonalized algorithm (ARC3D) was incorporated in to the code to alleviate the lack of convergence caused by grid stretching issues. This algorithm makes an approximation that the eigenvectors of the flux Jacobian matrices do not vary between adjacent grid points in space.

The left hand side of equation 2.28 can be discretized and factorized in different ways. The left hand side of equation 2.28 can be rewritten as :

$$[I + \Delta t(\frac{\bar{A}}{\Delta\xi} + \frac{\bar{B}}{\Delta\eta} + \frac{\bar{C}}{\Delta\zeta})]\delta\hat{Q}^n = [I + \frac{\Delta t}{\Delta\xi}\bar{A}][I + \frac{\Delta t}{\Delta\eta}\bar{B}][I + \frac{\Delta t}{\Delta\zeta}\bar{C}] = RHS^n \tag{2.33}$$

Another simplification is made in the expressions for $\bar{A}$, $\bar{B}$ and $\bar{C}$.

$$\bar{A} \simeq \hat{A}_{j+1} - \hat{A}_{j-1} \tag{2.34}$$

$$\bar{B} \simeq \hat{B}_{k+1} - \hat{B}_{k-1} \tag{2.35}$$

$$\bar{C} \simeq \hat{C}_{l+1} - \hat{C}_{l-1} \tag{2.36}$$

The resulting algorithm was given by Beam and Warming [76]. The factorization reduces the accuracy of the system to first order in time. This reduction of order of accuracy in time is not relevant since we are solving to a steady state, where all time derivatives go to zero. This algorithm involves inversion of block tri-diagonal matrix (5×5 A, B and C matrices, situated off diagonal), which is computationally very expensive. Further approximation by Pulliam and Chausee lead to the ARC3D algorithm.

$$\begin{aligned}
&[I + \tfrac{\Delta t}{\Delta\xi}\bar{A}][I + \tfrac{\Delta t}{\Delta\eta}\bar{B}][I + \tfrac{\Delta t}{\Delta\zeta}\bar{C}] = \\
&[T_\xi T_\xi^{-1} + \Delta t\delta_\xi T_\xi \Lambda_\xi T_\xi^{-1}][T_\eta T_\eta^{-1} + \Delta t\delta_\eta T_\eta \Lambda_\eta T_\eta^{-1}][T_\zeta T_\zeta^{-1} + \Delta t\delta_\zeta T_\zeta \Lambda_\zeta T_\zeta^{-1}] \simeq \\
&T_\xi[I + \Delta t\delta_\xi\Lambda_\xi]T_\xi^{-1}T_\eta[I + \Delta t\delta_\eta\Lambda_\eta]T_\eta^{-1}T_\zeta[I + \Delta t\delta_\zeta\Lambda_\zeta]T_\zeta^{-1} = RHS^n
\end{aligned}$$

where T_ξ is the left set of eigenvectors of matrix A and T_ξ^{-1} is the right set of eigenvectors of matrix A. Similarly, T_η and T_ζ matrices correspond to matrices B and C, respectively. The set of eigenvalues of matrix A are given in matrix Λ_ξ. The approximation assumes the eigenvectors of matrices A, B and C to be constant spatially in the neighborhood of (j, k, l).

This approximation reduces the number of operations dramatically, without modifying the stability or the steady state solution. The modified implicit algorithm requires inversion of three tri-diagonal (penta diagonal for second order in space with dissipation) matrices and multiplication with four 5×5 matrices for all grid points. This is opposed to inversion of three block tri-diagonal matrices in Beam Warming scheme. In two dimensions, the Beam Warming algorithm involves 410 multiplications, 356 additions and 10 divisions, a total of 776 operations, while the diagonalized algorithm requires 233 multiplications, 125 addition and 26 division and a total of 384 operations per grid point [54].

Flow field in a single C-H structured mesh could only be simulated using the original TURNS code. There was a need to modify the code so that it could solve the Navier-Stokes equations on any grid topology. This mainly required specification of more generalized boundary conditions, because the solution at interior points could be calculated by the existing flow solver. Several new boundary conditions were augmented to the code making it more general. Overset mesh capability was also incorporated in TURNS code.

A compressible solver works efficiently and accurately for moderate velocities, but the velocities observed in the proximity of the wing for the tilt rotors are very small in magnitude and not well modeled using a compressible solver (high artificial dissipation based on maximum wave speed). If a compressible solver is utilized, desired convergence is not achieved. Some modifications are necessary in the compressible solver to obtain accurate solution with faster convergence.

2.7 Preconditioning

A tilt rotor operates over a wide range of conditions, including hover, vertical climb, transition to airplane mode and high speed cruise. The hovering flight condition involves a very large region of low velocity flow (nearly incompressible conditions) in the proximity of the wing, compared to high velocity in the high speed cruise case. Transitioning flight from hover to forward flight would also involve moderate Mach numbers in the flow field, in-

hibiting the application of an incompressible solver. In order to simulate all these disparate conditions, employment of a single compressible solver, with adaptations to tackle different flight regimes, is assumed to be more appropriate as opposed to developing or using different solvers for different conditions.

Slow forward flight and vertical climb of a Quad Tilt Rotor was simulated using a compressible RANS solver [65] in and out of ground effect. Operation of the Quad Tilt Rotor in ground effect dramatically reduced the download on the wings when compared to out of ground effect operation. Confirmation of these findings was shown by experiments conducted by Radhakrishnan and Schmitz [19, 20]. However, usage of a compressible solver limited the free stream Mach number to a relatively high value. A need for modeling lower free stream Mach numbers is deemed necessary to approach more realistic vertical climb velocities and eventually hovering conditions. These small Mach numbers ill-condition the governing equations, such that the characteristic speeds of the different waves are very disparate. This ill-conditioning of the matrices leads to slow convergence and inaccurate solutions. Hence, some modifications to the existing numerical scheme are necessary. Preconditioning of Navier Stokes Equations for more accurate and faster solutions in these low Mach number flows is adopted. Many of the low Mach number preconditioning methods have been summarized by Turkel [66–68]. All the preconditioning methods suggested by Turkel involve modification of the acoustic wave speed. The methods discussed by Turkel are specialized for different applications, such as reacting flows, where the energy equation is preconditioned differently to account for the source terms in the energy equation. Other applications involved strong temperature variations, which leads to the inclusion of temperature terms in the preconditioning matrix. These complications are not present in the current work and hence the simplified Roe-Turkel preconditioning is adopted and will be discussed in detail in later sections.

Low Mach number preconditioning was also employed by Gleize and Costes [71] for simulating the low speed turbulent flow around the helicopter fuselage. They implemented local preconditioning suggested by Choi and Merkle [72] for viscous flows. Extensive comparison of non-preconditioned results with preconditioned results is presented in their work and

benefits of preconditioning are discussed.

2.7.1 Roe Upwinding Scheme

The flux terms in compressible Navier-Stokes equations consist of inviscid fluxes and viscous fluxes. The viscous fluxes are elliptic (dissipative) in nature, where as the inviscid fluxes are hyperbolic in nature. In other words, the inviscid fluxes are carried along waves and travel in the direction of the characteristic wave, unlike viscous fluxes, which dissipate equally in all directions. Upwind schemes are favored while modeling the inviscid fluxes to ensure that the waves travel in the appropriate directions.

Roe upwinding has been successfully used in solving many problems involving transonic flows [73]. Roe scheme is only demonstrated for one dimensional flow for simplicity.

$$\frac{\partial Q}{\partial t} + \frac{\partial F}{\partial x} = S \tag{2.37}$$

where Q is the state vector, F is the flux vector, and S is the source term vector. These vectors are expanded below.

$$Q = \left\{ \begin{array}{c} \rho \\ \rho u \\ \rho e \end{array} \right\} \tag{2.38}$$

$$F = \left\{ \begin{array}{c} \rho u \\ \rho u^2 + p \\ \rho u H \end{array} \right\} \tag{2.39}$$

$$S = \left\{ \begin{array}{c} 0 \\ f_x \\ u f_x \end{array} \right\} \tag{2.40}$$

where ρ, u, H, e, f_x and p are the density, velocity, enthalpy, total energy, body force and pressure respectively. The flux Jacobian can be written as:

$$A_c = \frac{\partial F}{\partial Q} =$$

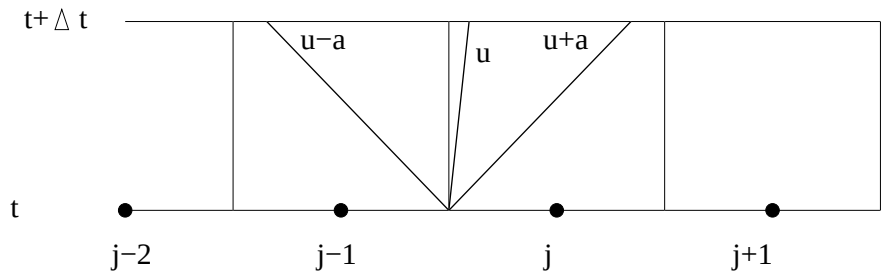

Figure 2.19: Waves at the interface.

$$\left\{ \begin{array}{ccc} 0 & 1 & 0 \\ \frac{3-\gamma}{2}u^2 & (3-\gamma)u & (\gamma-1) \\ (\gamma-1)u^3 - \gamma ue & \gamma e - \frac{3(\gamma-1)u^2}{2} & \gamma u \end{array} \right\} \tag{2.41}$$

where γ is the ratio of specific heat of gases.

The eigenvalues of the system of hyperbolic Euler equations are :

$$\lambda = \left\{ \begin{array}{c} u \\ u+a \\ u-a \end{array} \right\} \tag{2.42}$$

where a is the speed of sound. The eigenvalues of the hyperbolic equations are synonymous to the propagation speeds of the disturbances through the fluid. As the Mach number is small, it can be noted that the first eigenvalue, associated with the material wave is much slower than the second and third eigenvalues, associated with the acoustic waves. Such large disparities in eigenvalues slow down the convergence, because the material waves travel for a very short distance as compared to the acoustic waves for a particular time step. The time step chosen is governed by the stability limit of the differencing scheme employed (linearization errors).

For a one dimensional equal spaced mesh, the waves at the interfaces of the cells travel in different directions depending on the eigenvalues (u, $u+a$ and $u-a$). The waves at the interface $(j+1/2)$ are shown in Figure 2.19.

It can be inferred from Figure 2.19 that the acoustic waves travel much further than the material wave. The distance traveled by the material wave is $Ma\Delta t$, where as the distance

traveled by the larger acoustic wave is $(M+1)a\Delta t$. The ratio of the smallest and the largest eigenvalue, also known as the condition number is M/(M+1). This ratio dictates the rate of convergence, higher values leading to a faster convergence. To obtain a converged solution, all the waves should travel to the boundary and reflect and settle down to a steady state. Since the material waves move very slow, it will take a long time for the solution to converge and the convergence is restricted by the material waves. This convergence issue is ameliorated by preconditioning the equations and is presented in the next section.

The other issue of accuracy of Roe upwinding for low Mach number flows is discussed next. If differencing scheme, which is Euler explicit in time and first order upwind in space is employed, the equation 2.37 can be discretized as.

$$\delta Q_j^n = -\frac{\delta t}{\delta x}(F_{j+1/2}^n - F_{j-1/2}^n) \tag{2.43}$$

$$F_{j+1/2} = \frac{F_{j+1} + F_j}{2} - \frac{1}{2}|A_{j+1/2}|(Q_{j+1} - Q_j) \tag{2.44}$$

where $|A| = T^{-1}|\Lambda|T$, T is the set of eigenvectors of A and Λ is the set of eigenvalues. Roe scheme adopts density averaging to obtain the fluxes at the cell interfaces (j+1/2). The density, velocity and enthalpy are calculated at the cell interfaces using the following equations.

$$\rho_{j+1/2} = \sqrt{\rho_j \rho_{j+1}} \tag{2.45}$$

$$u_{j+1/2} = \frac{\sqrt{\rho_j}u_j + \sqrt{\rho_{j+1}}u_{j+1}}{\sqrt{\rho_j} + \sqrt{\rho_{j+1}}} \tag{2.46}$$

$$h_{j+1/2} = \frac{\sqrt{\rho_j}h_j + \sqrt{\rho_{j+1}}h_{j+1}}{\sqrt{\rho_j} + \sqrt{\rho_{j+1}}} \tag{2.47}$$

After manipulation for Roe scheme at low Mach numbers, it can be noted that several terms in $|A|$ have different order of Mach number from terms in A. This difference in order of Mach number leads to large dissipation terms (evident from the momentum equation, where A has O(1), and $|A|$ has O(1/M); in the energy equation the dissipation terms are too small) for low Mach number flows and is a major source of inaccuracy in such flow regimes.

$$A \simeq \begin{bmatrix} 0 & O(1) & 0 \\ O(1) & O(1) & O(1)) \\ O(\frac{1}{M^2} & O(\frac{1}{M^2}) & O(1) \end{bmatrix} \tag{2.48}$$

$$|A| \simeq \begin{bmatrix} O(1) & O(M) & O(M) \\ O(\frac{1}{M}) & O(\frac{1}{M}) & O(M) \\ O(\frac{1}{M}) & O(\frac{1}{M}) & O(\frac{1}{M}) \end{bmatrix} \tag{2.49}$$

Turkel preconditioner will be discussed next, which not only accelerates the convergence for low Mach number flows, but also provides a more accurate steady solution by modifying the dissipation terms.

2.7.2 Turkel Preconditioner

Preconditioning involves modification of Navier Stokes Equations to achieve faster convergence, with more accurate solutions for special cases. The effectiveness of the preconditioner is only demonstrated theoretically for Euler equations in one dimension for simplicity, although the Navier Stokes equations in three dimensions are preconditioned in the present work.

Roe-Turkel preconditioning algorithm was adopted by Guillard and Viozat [69] in a compressible code for unstructured grids. It was employed in simulating low Mach number flow over symmetric airfoils at zero degrees angle of attack. Notable improvements are observed in these cases by the application of the preconditioner. The Roe-Turkel preconditioning matrix used to modify the wave speeds and dissipation can be written as:

$$P = I + \frac{(\beta^2 - 1)(\gamma - 1)}{a^2} \begin{Bmatrix} \frac{u^2}{2} & -u & 1 \\ \frac{u^3}{2} & -u^2 & u \\ \frac{Hu^2}{2} & -uH & H \end{Bmatrix} \tag{2.50}$$

The modified Euler equations as a result of preconditioning can be written as:

$$\frac{\partial Q}{\partial t} + PA\frac{\partial Q}{\partial x} = PS \tag{2.51}$$

The eigenvalues of the modified system are :

$$\lambda = \left\{ \begin{array}{c} u \\ \frac{u(1+\beta^2)+\sqrt{u^2(\beta^2-1)^2+4a^2\beta^2}}{2} \\ \frac{u(1+\beta^2)-\sqrt{u^2(\beta^2-1)^2+4a^2\beta^2}}{2} \end{array} \right\} \tag{2.52}$$

It can be easily noted that if β is chosen to be of the same order as the Mach number, the magnitude of the acoustic eigenvalues can be reduced (2^{nd} and 3^{rd}) and brought closer to the magnitude of the convective eigenvalue (1^{st}), without altering their signs. It is necessary to maintain the sign of the eigenvalues, because the sign determines the direction of wave propagation. If a wave is forced to propagate in a wrong direction, it will carry information in the wrong direction and hence will defy the conservation laws.

The condition number, which is the ratio of the magnitude of smallest eigenvalue to the magnitude of largest eigenvalue in plotted in Figure 2.20. It clearly shows that the condition number is higher for the preconditioned case for low Mach number regime, implying the closeness of eigenvalues for the preconditioned as compared to the non preconditioned case. This modification enables the choice of a larger time step as compared to an unmodified system, leading to faster convergence, although limiting its application to steady state problems. If β is chosen to be one then the eigenvalues are unchanged and the non preconditioned system is obtained. Thus, the parameter β allows for a consistent unified approach from transonic flow to nearly incompressible flow.

Dissipation terms added to the hyperbolic equations enhance the accuracy and stability of the algorithm (source of error in any numerical scheme). The dissipation terms added in Roe-Turkel scheme for low Mach number flows are of the form.

$$P^{-1}|PA| \simeq \left[\begin{array}{ccc} O(1) & O(1) & O(1) \\ O(1) & O(1) & O(1)) \\ O(\frac{1}{M^2} & O(\frac{1}{M^2}) & O(\frac{1}{M^2}) \end{array} \right] \tag{2.53}$$

The order of terms as a function of Mach number is similar to order of terms in A matrix. This characteristic of the dissipation matrix keeps the terms bounded even at low Mach

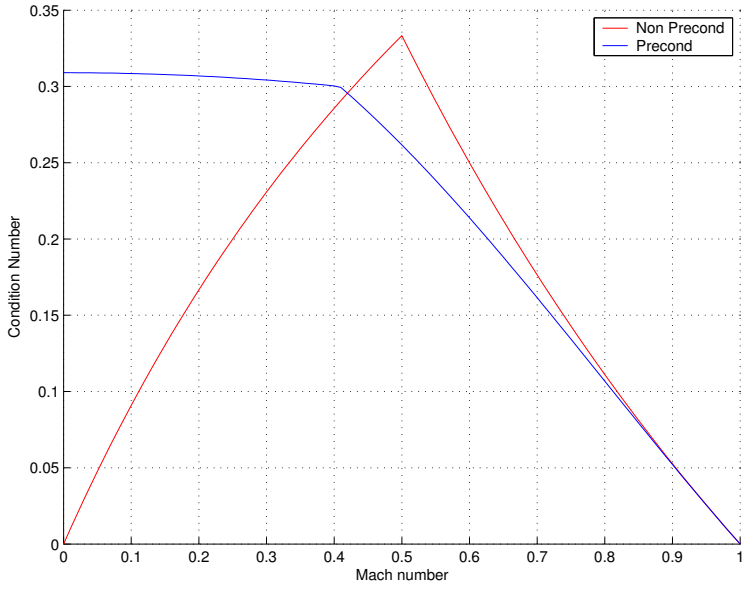

Figure 2.20: Comparison of condition number ($\beta = 1$ for Non Preconditioned; $\beta = \mathrm{M}$ for Preconditioned).

numbers, improving the accuracy of the system for low Mach number flows.

There are other advantages of implementing low Mach number preconditioning, which have been identified in the literature [66]. Pressure terms in low Mach number flows are not scaled properly relative to convective terms [70], leading to large round off errors. This problem can be partly rectified by using double precision, but that increases the turn around time and also the memory requirements. Preconditioning scales these terms appropriately. Finally, as already elucidated, the magnitude of the acoustic eigenvalues is brought closer to the magnitude of convective eigenvalues, resulting in faster convergence.

Chapter 3

Verifications and Validations

The flow field around the QTR is highly complicated and before attempting to simulate the QTR flow field, it is necessary to apply the current methodology to simpler problems to gain confidence in the solution algorithm. First, the solution algorithm is verified by applying it to two dimensional problems and demonstrating its effectiveness and consistency. The effectiveness of the preconditioner is also verified for a model problem of rotor-wing interaction. This exercise does not test the accuracy of the solver, but only verifies its effectiveness. Accuracy of the solver needs to be verified, hence the algorithm is employed to simulate a V-22 rotor and the results obtained are validated against experiments and are presented next. Finally, the rotor-wing interaction experiment by Felker is modeled and comparison of computational results with experiment is presented.

3.1 Effectiveness of Preconditioner for 2-D Airfoil

Effectiveness of preconditioning is demonstrated by simulating the flow over a symmetric airfoil at zero degree angle of attack for a free stream Mach number of 0.05 for inviscid flow using Pulliam Chaussee algorithm on the left hand side. The pressure contours are plotted in Figure 3.1 near the leading edge of the airfoil with and without the application of preconditioning after 500 iterations. The pressure contours are smoother with the application of preconditioning as compared to the case without the preconditioner. Non smooth contours

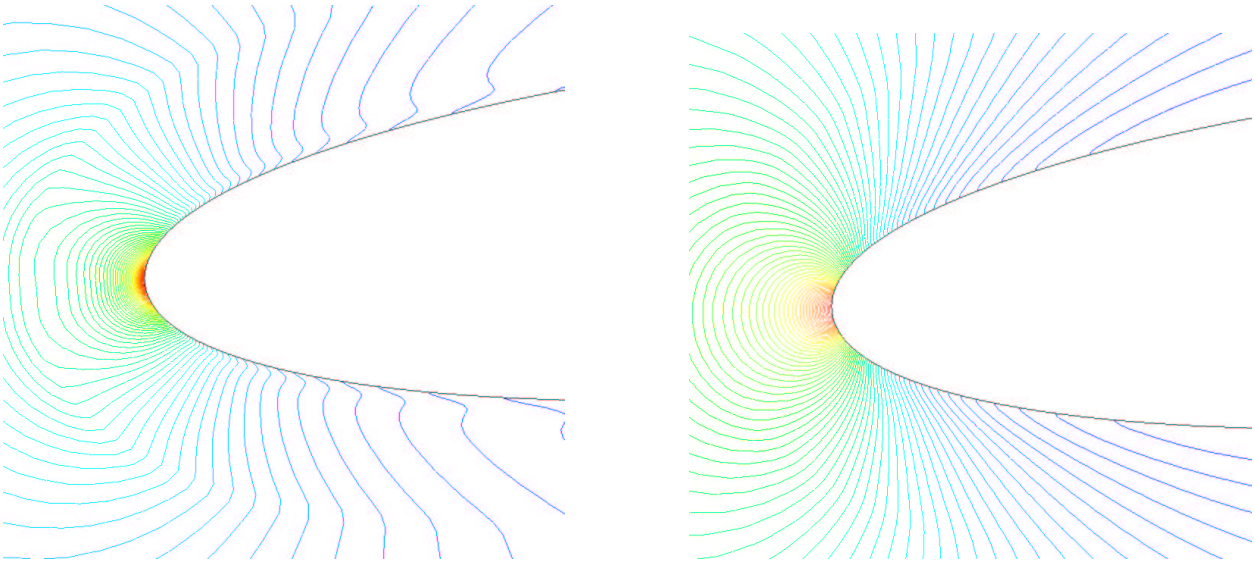

(a) Without preconditioning

(b) With preconditioning

Figure 3.1: Pressure contours of flow over a symmetric airfoil at zero degree angle of attack (Inviscid Flow).

lead to incorrect pressure gradients at the surface of the airfoil. This can lead to velocity gradients at the wall (entropy gradients), which are non-physical in inviscid flow. Convergence history of the two cases is plotted in Figure 3.2. The differences in the converged solutions between the preconditioned and non preconditioned case when single precision data is used disappeared on employment of double precision data for the inviscid case. Dissipation errors are smaller in the inviscid case, because cell aspect ratio near the wall is not very high. The smaller aspect ratios are better modeled with double precision and lead to better convergence and a larger drop in errors. The use of double precision was found to be sufficient at this Mach number (0.05) for inviscid flow.

The Beam-Warming type scheme with the inclusion of viscous Jacobian on the left hand side is observed to be efficient for viscous low Mach number flows. Inclusion of the viscous Jacobian on the left hand side makes it very beneficial in simulating low Reynolds number flow. Beam-Warming type scheme is computationally more expensive per iteration, but

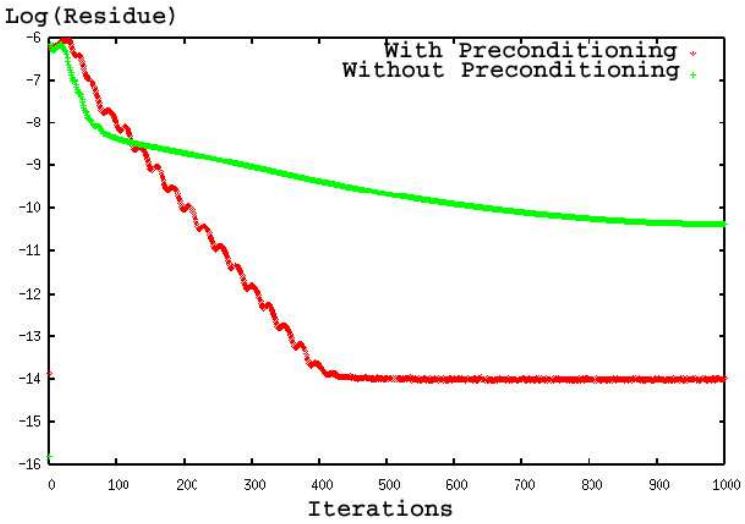

Figure 3.2: Comparison of convergence history.

accelerates the convergence enormously. The flow is assumed to be completely laminar with all viscous terms included (no thin layer approximation).

Pressure contours for low Mach number(= 0.05) viscous flow (Reynolds number= 300,000) over a symmetric airfoil at zero degree angle of attack are shown in Figure 3.3 with and without the application of a preconditioner. Application of preconditioning leads to much smoother contours near the surface of the airfoil, demonstrating the accuracy benefit of preconditioning. Abrupt changes in the pressure contours are observed near the surface of the airfoil. These abrupt changes demonstrate incorrect modeling of the boundary layer. This incorrect modeling of the boundary layer leads to incorrect drag prediction. For the viscous case even the use of double precision data is not beneficial in improving the accuracy of the solution and there are clear differences in the converged solutions with and without preconditioning. The smoothness of the contours for the preconditioned case did not get altered much when double precision is employed. Therefore, single precision accuracy is sufficient for the preconditioned system.

Application of preconditioning is also investigated for an airfoil at 90 degrees angle of attack relative to the flow. The coefficient of pressure contours are shown in Figure 3.4. Flow is completely separated on the lower surface, as expected. Averaged drag coefficient of

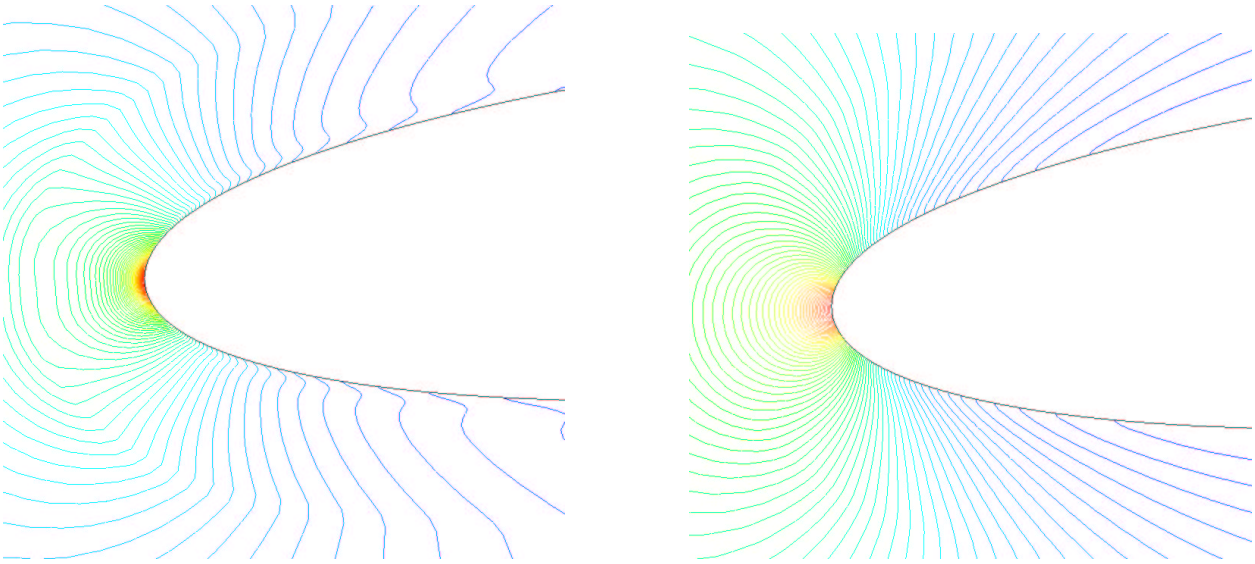

(a) Without preconditioning

(b) With preconditioning

Figure 3.3: Pressure contours of flow over a symmetric airfoil at zero degree angle of attack (Reynolds number=300,000).

1.56 is obtained for this case, which is quite representative. Stagnation point is located very close to mid chord. The velocity vectors close to the stagnation point are shown in Figure 3.5. It should be noted that this case did not converge to a steady state and the solution is shown at one of the time instances.

Force coefficients obtained for viscous flow (Reynolds number = 300,000, Mach number = 0.05) at different angles of attack for both preconditioned and non-preconditioned cases are listed in Table 3.1. Higher stretching in the cells near the airfoil surface magnifies the errors in the non-preconditioned system. All the force coefficients for the preconditioned case are predicted to be lower than that for the non preconditioned case, except for the 10 degrees angle of attack, where the flow is separated near the trailing edge in the preconditioned case. The dissipation added to the system of equations is much higher for the non-preconditioned case. This higher dissipation in the non-preconditioned system leads to these inaccuracies.

There is no sign of separation for the non preconditioned case at 10 degrees angle of

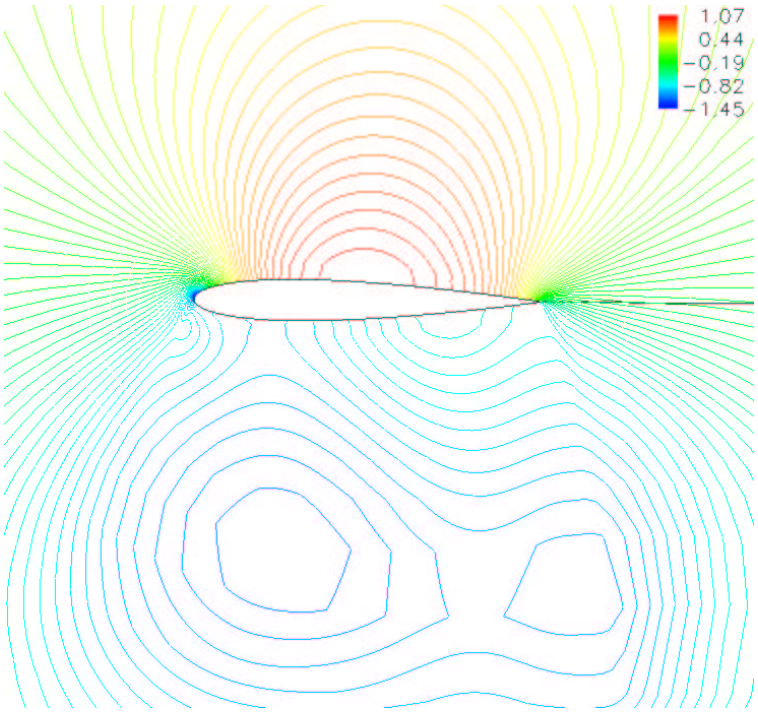

Figure 3.4: Pressure contours of flow over a symmetric airfoil at 90 degrees angle of attack (Reynolds number = 300,000) with preconditioning.

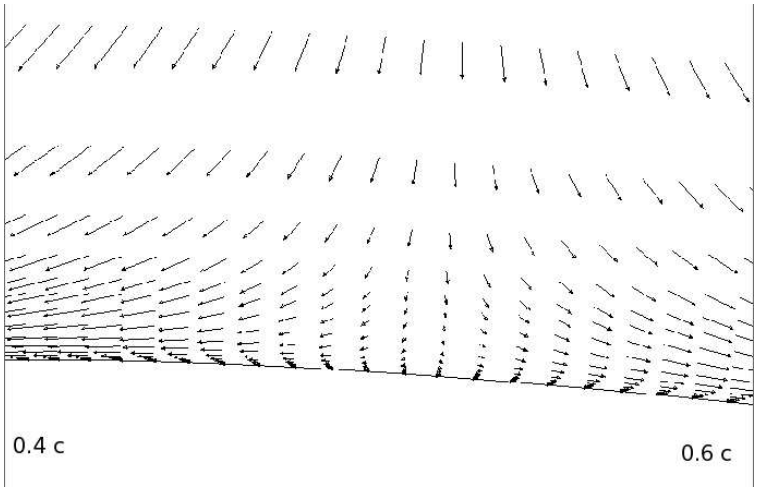

Figure 3.5: Velocity vectors close to the stagnation point for a symmetric airfoil at 90 degrees angle of attack (Reynolds number = 300,000) with preconditioning.

Table 3.1: Comparison of coefficient of forces for NACA-0012 airfoil at Mach number=0.05 (Reynolds number = 300,000) as a function of angle of attack.

	No Preconditioning		Preconditioning	
Angle of Attack	C_l	C_d	C_l	C_d
0	0.000	0.0179	0.000	0.0128
5.	0.575	0.0169	0.534	0.0131
8.	0.905	0.0203	0.852	0.0192
10.	1.103	0.0232	1.037	0.0306
12.	1.297	0.0343	-	-
90.	-	-	0.092	1.561

attack. The reason for this delay in separation is higher shear stresses (higher gradient of velocity) predicted at the airfoil surface boundary for the non preconditioned case, when compared to the preconditioned case. This is very evident from Figure 3.6, which plots the velocity vectors in the boundary layer near the mid chord (x/c=0.52). The shorter arrows are for the preconditioned case and the longer one represent the boundary layer of the non-preconditioned case. This case without preconditioning has excessive dissipation in the calculation of convective fluxes close to the wall and artificially thins the boundary layer and leads to higher shear stress at the surface.

Drag coefficient for 0 degree angle of attack for various Mach numbers are listed in Table 3.2. The preconditioned case predicts exactly the same value of drag coefficient with decreasing Mach number, where as the drag coefficient increases monotonically for the non preconditioned case.

3.2 Verification of Preconditioner for a Model Problem

A single rotor-wing interaction model is simulated in this work. A set of three meshes (rotor mesh, wing mesh and background mesh) is employed. The configuration of the rotor, wing

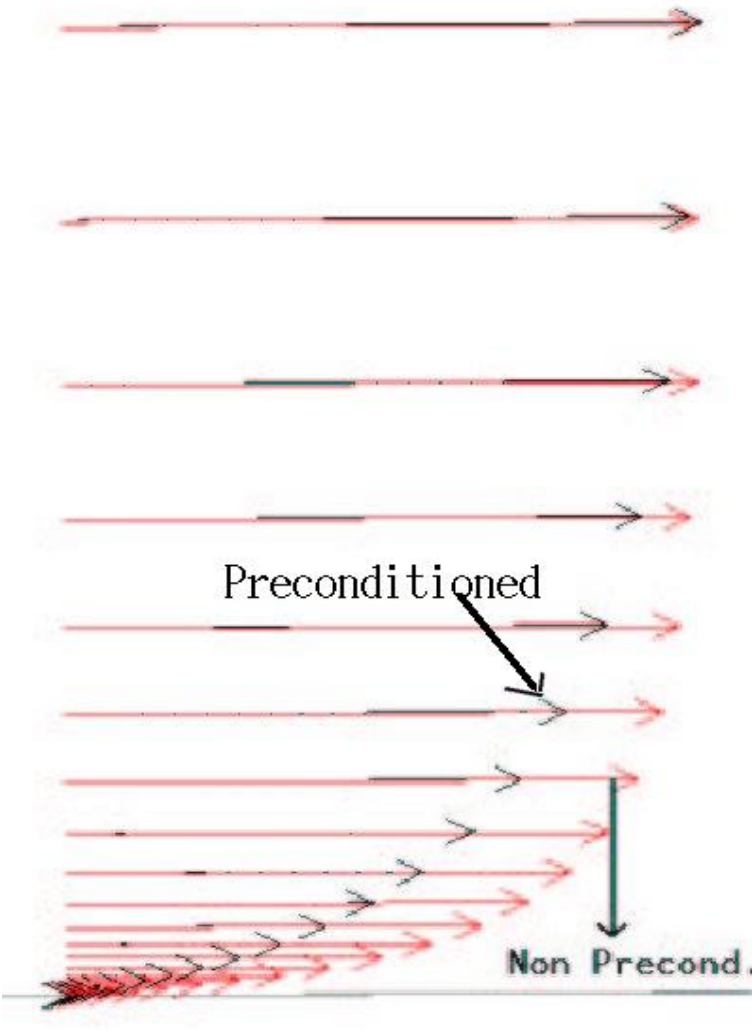

Figure 3.6: Boundary layer comparison for angle of attack of 5 degrees with Mach number = 0.05 (Reynolds number=300,000; red arrows for non preconditioned case and black arrows for preconditioned case).

and Cartesian meshes, along with the boundary conditions adopted, is shown in Figure 3.7. The aspect ratio of the wing is chosen to be 6 and the diameter of the rotor is 4.5 times the chord of the wing. The rotor is located 2 chords above the wing, with the center being directly above the mid chord of the wing tip. The rotor tip Mach number is chosen to be 0.5. The operational parameters are not the same as those for the V-22, but are representative

Table 3.2: Comparison of Coefficient of Drag for NACA-0012 airfoil at 0 degree angle of attack (Reynolds number = 300,000) as a function of Mach number.

Mach No.	Preconditioning C_d	No Preconditioning C_d
0.2	0.0128	0.0130
0.1	0.0128	0.0144
0.05	0.0128	0.0179

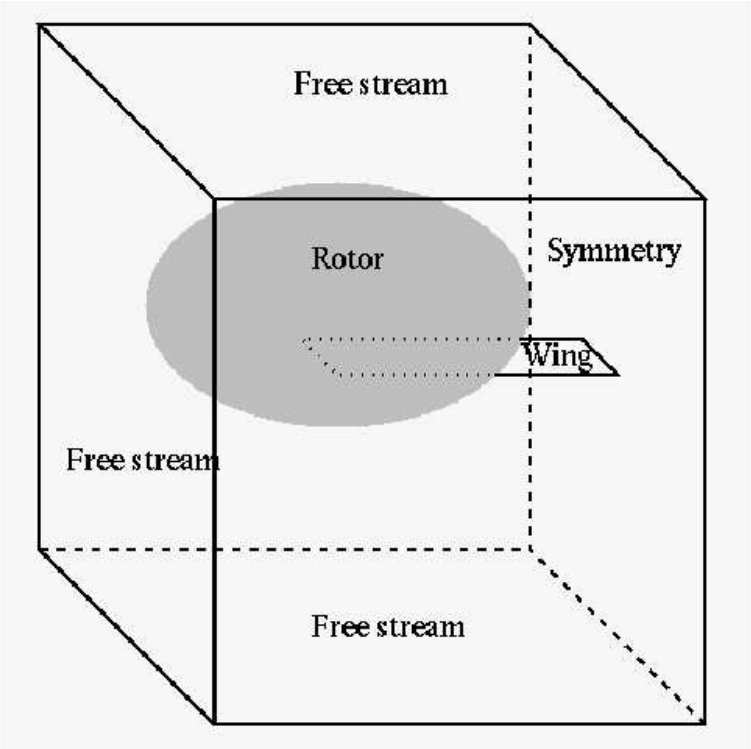

Figure 3.7: Configuration of various grids.

of a typical tilt rotor.

3.2.1 Grid Topology

A set of three grids is employed for modeling the downwash from a rotor on to a wing. The rotor is modeled as a part of a plane in a cylindrical grid across which source terms are added. Points are clustered in the radial direction in the proximity of the rotor root

and tip. Similarly, clustering is maintained in the axial direction on either side of the rotor plane. A C-H viscous grid is generated around the wing with airfoil section NACA-2323 by stacking together 2 dimensional grids, obtained using a hyperbolic grid generator. Points are clustered in the span wise direction near the wing tip and also at the wing root at the symmetry plane. A background Cartesian mesh is employed for information transfer and specification of free stream boundary conditions. This grid is fine in the overlapping region with the near body meshes and coarse beyond it. One of the boundaries of the Cartesian grid is specified as a symmetry boundary and the rest are labeled as free stream boundaries. Free stream boundaries are updated using method of characteristics ensuring no wave reflections. The choice of a symmetry boundary condition reduced the number of grid points to a half, without loss of any accuracy, because the employed time averaged rotor model will not capture the effect of individual blades and hence will not be able to resolve any lateral shifting of flow across the symmetry plane as observed by Polak [11] and Potsdam [28] for the full span model. These grids are shown in Figure 3.8. The total system contains approximately 1.5 million grid points.

3.2.2 Results on Model Problem

The objective of this work is to simulate the flow around a wing with a rotor hovering above it. These flow features can be easily associated to fountain flow in tilt rotors. Unfortunately, the free stream velocity is limited by compressibility issues of the solver and cannot be reduced to zero, which would be the case for a hovering rotor. Reduction of this free stream velocity is attempted to a very low value in this work, by employing low Mach number preconditioning, so that hovering conditions can be approached asymptotically.

Vertical descent, vertical climb, forward, backward and sideward flight of the wing and rotor combination at various free stream Mach numbers are simulated with the rotor operating above the wing. Same grids are employed for the vertical climb, vertical descent, forward and backward flight conditions, with the only alteration being the direction of the free stream velocity. The whole wing is simulated for the sideward flight, because the flow is

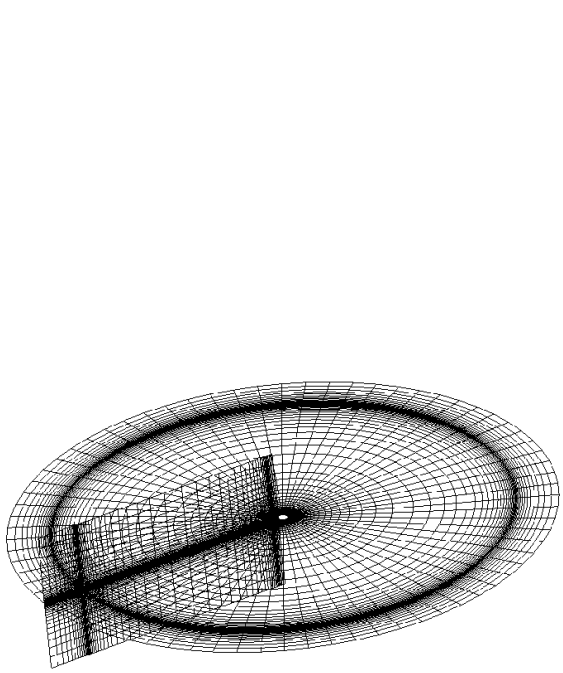

(a) rotor grid

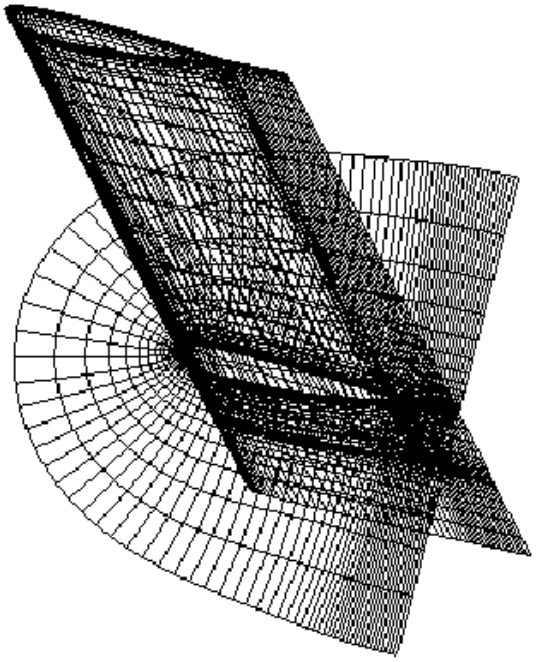

(b) wing grid

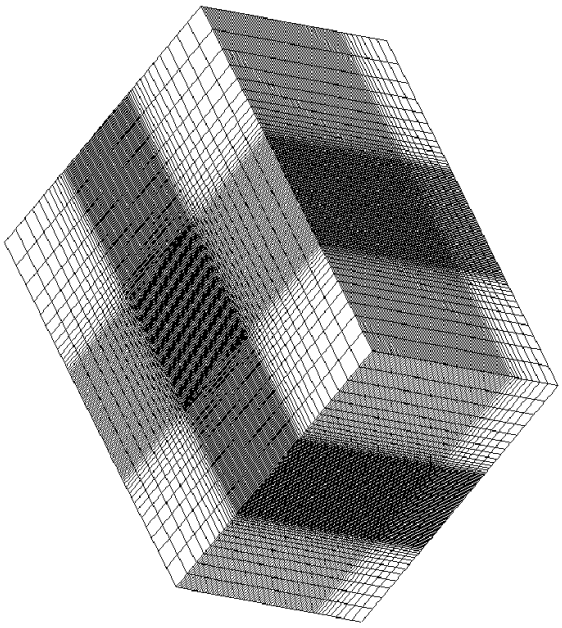

(c) background grid

Figure 3.8: Various grids employed for modeling rotor-wing interaction.

not symmetric, inhibiting the application of symmetry. Download on the wing is calculated for various free stream velocities and the results are presented in Table 3.3 as a percentage of the rotor thrust, rendering it non dimensional. For vertical climb and descent cases, λ_c represents the ratio of the climb or descent rate to the rotor tip speed. λ_c will also be referred to as advance ratio in this section . Download on the wing is compared at same advance ratios (μ for forward, backward and sideways flight, λ_c for vertical climb or descent) for different flight conditions.

The differences in the downloads for different flight conditions at $\mu = 0.02$ suggest that the effect of climb or forward velocity could not be neglected and there is a need to simulate even lower free stream velocity or advance ratio. Hence, vertical descent, climb, and forward flight along with backward and sideways flight are simulated at $\mu = 0.01$. The differences in the downloads between the various flight conditions are certainly lower than the previous case, but are still significant. Even lower free stream velocity is therefore desired and attempted. Forward, backward, sideways and vertical climb conditions are simulated for $\mu = 0.002$. At $\mu = 0.002$, the differences in integrated downloads are greatly reduced (between 10.1 and 10.6) and suggest that either vertical climb, sideways, backward or forward flight is a good approximation to the hovering condition. The integrated downloads for the lowest advance ratio are very close to each other for different flight directions, but distribution of the loading on the wing and flow patterns around the wing are compared to gain more confidence in the algorithm.

Velocity vectors at a plane (at 84% of the wing span) parallel to the symmetry plane are shown in Figure 3.9 for the vertical climb, vertical descent, forward and backward flight conditions at $\mu/\lambda_c = 0.01$. These figures clearly indicate the skewing of the velocity vectors for the forward and backward flight case when compared to vertical climb and descent conditions. The velocity vectors in the vertical descent condition appear very similar to the vertical climb condition, but have a slightly lower magnitude as compared with the climb velocity. All the four configurations suggest a large pocket of separated flow below the wing. The velocity vectors are more closely shown around the wing for the four cases in Figure 3.10.

Table 3.3: Comparison of Download to Thrust ratio for various flight conditions at C_t = 0.01.

Condition	μ or λ_c	D/T%
Climb	0.02	8.9
Climb	0.01	10.6
Climb	0.002	10.1
Forward	0.02	5.3
Forward	0.01	8.9
Forward	0.002	10.6
Descent	0.02	8.4
Descent	0.01	9.0
Descent	0.001	10.0
Backward	0.01	10.0
Backward	0.002	10.2
Sideways	0.01	9.8
Sideways	0.002	10.2

Again, velocity vectors in the vertical climb and descent conditions look very similar. Also, the velocity vectors have much larger magnitude in the backward flight, vertical climb and descent cases past the trailing edge of the wing section when compared to velocity vectors in the forward flight case. The difference in orientation of the velocity vectors strongly suggests a difference in center of pressure location of the wing section, but nothing can be concluded with confidence about the magnitude of the downward forces at this section by observing the velocity vectors.

The difference in the pressure value and the free stream pressure value is divided by the disk loading of the rotor to obtain a non-dimensional representation of pressure (C_{pDL}), instead of adopting the more common coefficient of pressure (C_p). This parameter directly represents the pressure as a ratio of downwash dynamic pressure and not the free stream

dynamic pressure, which is meaningless in this problem since the free stream velocity is minimal (zero in true hover).

$$C_{pDL} = \frac{p - p_\infty}{T/A} \tag{3.1}$$

Contours of C_{pDL} are plotted at the same span wise location of the wing for the four flight conditions in Figure 3.11. The peak of the pressure contours is centered very close to the trailing edge for the backward flight case. The peak moves towards the leading edge on the top surface for the vertical descent and climb cases, and it moves further upstream for the forward flight condition. C_{pDL} on the surface of the wing section is plotted for all four cases in Figure 3.12. As expected, the pressure variation on the lower surface is almost the same for the four cases, but it distinctly varies on the top surface. The shape of the curve for the vertical descent case is very similar to the vertical climb case. However, the integrated force for the descent case is much smaller than that for the climb case. The peak of pressure shifts towards the leading edge for the forward flight case and towards the trailing edge for the backward flight case, which is also clear from the previous pressure contour plots. The sectional integrated force for the four cases seem very similar. However this is not true when the forces on the entire wing are compared. This wing section shows the typical flow features around the wing, but does not represent the entire flow field. Therefore, span wise lift on the wing is shown in Figure 3.13. Clear differences in the download can be observed among the four flight conditions at $\mu = 0.01$. The closeness of the sectional download at 84% span justifies the similarity in integrated pressure loading at 84% span wise location shown in Figure 3.12.

Velocity vectors for the lowest advance ratio ($\mu/\lambda_c = 0.002$) at the same span wise location as the previous results are shown in Figure 3.14. Unlike the higher advance ratios, the velocity vectors look very similar in the four cases, even though the free stream velocity is in a different direction for the four cases. The C_{pDL} contours at the same location are shown in Figure 3.15. This comparison also reveals a similarity in contours, although the center of pressure seems to have shifted more towards the trailing edge for the vertical climb

condition. C_{pDL} is plotted at 84 % wing span section surface for the four cases in Figure 3.16. Similar to the pressure contour plot, the center of pressure is observed to have moved aft for the vertical climb condition. Integrated loads at the same sections are comparable to each other for the cases. A comparison of the span wise variation of the download on the wing is shown in Figure 3.17. The download in the vertical climb case is only slightly higher as compared to the forward flight case.

The inclusion of Roe-Turkel preconditioning in the solver and its application on two dimensional airfoils and the model problem justifies its advantages in terms of consistency and efficiency for low Mach number flows. It is still necessary to apply the solver to simple but representative problems and compare the results with experiments to gain confidence in the solver capabilities. A systematic approach is adopted to validate the solver for a set of representative problems. The solver is verified for the results obtained on isolated V-22 rotor and installed V-22 rotor over a V-22 wing for experiments.

3.3 Validation of the Rotor Model

A single cylindrical grid is used for validation of the rotor model, with far-field boundary condition extending up to four times the rotor radii in all directions. The grid utilized for validation is shown in Figure 3.18, extending till the far-field. Thus, overset meshes are not used for validation of the rotor model. However, little effect is seen when overset meshes were used.

3.3.1 Comparison with Corrected Momentum Theory

The rotor model is validated for various thrust coefficients for a constant climb velocity ($v_c/v_{tip} = 0.002$). In this process, the induced power of the rotor is calculated for several thrust coefficients and compared with Momentum Theory. This comparison is shown in Figure 3.19. The computational results follow the cubic square law similar to Momentum Theory [64] ($C_p = kC_t^{3/2}$). A representative value of 1.15 was chosen for k. This factor

increases the induced power requirement for Momentum Theory calculations. A relatively small climb velocity (1.5 ft/sec) is used, because of the inability to model zero free stream Mach number. The rotor used, consists of 3 blades and each blade is assumed to have a rectangular plan form of aspect ratio, 13.0, with a linear twist of 15^0. The rotor model is also validated for various advance ratios at a constant thrust ($C_t = 0.0064$) in ground effect and out of ground effect cases in forward flight (Figure 3.20). A comparison of induced power for various advance ratios is demonstrated with Momentum Theory. The results show good correlation with momentum theory results for out of ground effect in forward flight.

3.3.2 Simulation of the V-22 Rotor

Before applying the Rotor Model to the current problem of a Quad Tilt Rotor, it is validated against some experimental results obtained for the TRAM rotor (0.25 scale V-22 rotor) [79] and 0.658 scale V-22 rotor [7]. V-22 rotor characteristics are compiled in Table 3.4. The TRAM isolated rotor was tested at Duits-Nederlande Wind tunnel Large Low speed facility (DNW-LLF) and is a reliable source of loads on the blades of the rotor. A climb rate of 0.001 times the tip speed (between 1-2% of the induced velocity) is assumed to be a good approximation to hover. In the current work, such a small climb rate will be used to model hovering conditions. This climb rate was shown to be sufficient while simulating hovering conditions for the model problem. The TRAM rotor is simulated in hover in the current work for various collective settings using the rotor model with low Mach number preconditioning.

The loading on the blade is compared between the experiment and computation for a thrust coefficient of 0.0149 and is shown in Figure 3.21. The blade loading obtained for the same conditions, as obtained by a computation by Potsdam [28], is also shown in the figure. The loading matches very well until 0.8 R, but then starts to diverge from the experimental data further outboard. The predicted differences at the tip are more exaggerated for the Rotor Model than for the more detailed individual blade calculations of Potsdam. Similar results (not shown) are obtained for a range of thrust coefficients.

Felker [7] measured the downwash velocity at a location 0.42 rotor radii below the rotor

Table 3.4: V-22 rotor characteristics

Rotor Radius	19 feet
Solidity	0.105
Tip chord	22 inches
Twist	32 to -6 degrees
Airfoil sections	XN series

(shown in Figure 3.22). The velocity vectors obtained computationally using the current analysis at an azimuthal plane for a thrust coefficient of 0.0164 are shown in Figure 3.23. The contraction of the wake is clearly evident in the computation. Relatively little mass flow is observed in the center for this tilt rotor configuration. The measured velocity distribution is compared with the computational result obtained using the Rotor Model in Figure 3.23. Although the loading on the blade obtained by the Rotor Model does not compare very well at the tip to the loads obtained experimentally, nonetheless the axial velocity distribution agrees very well in the wake. The velocity distribution is compared at the exact location where the wing would be placed in the installed rotor condition. The agreement builds up confidence in employment of the rotor model for the current problem.

3.4 Comparison with Felkers Experiment

After gaining confidence in the rotor model in its ability to simulate the flow field through a rotor, the problem of rotor-wing interaction is analyzed. Rotor-wing interaction is an integral part of the flow field around the Quad Tilt Rotor and accurate modeling of this interaction is a daunting challenge.

The rotor downwash impinges on the wing and causes a large downward force on the wing. The presence of the wing modifies the induced velocity distribution and hence the performance of the rotor. This aerodynamic interaction problem was analyzed by Felker. Felker [7] conducted an experiment in 1990 on a semi span 0.658 scale model of the V-22. In

Table 3.5: Parameters of Felkers' Experiment

Rotor Wing vertical separation	1.6 m
Wing Span	4.75 m
Wing Chord	1.76 m
Wing Twist	0^0
Wing Dihedral	3.5^0
Airfoil	Bell A821201
Flap Deflection	67^0
Pressure Tap Locations (%R)	30, 50, 70, 90
Rotor	V-22 rotor
Rotor Radius	3.81 m
Rotor Tip Speed	144 m/sec
Rotor C_t	0.0186

this experiment, pressure measurements were acquired at the surface of the wing at several span wise locations with the rotor rotating at the tip of the wing at various collective settings. Significant parameters for this test are listed in Table 3.5.

The experimental set up was simulated using overset meshes. The rotor was approximated once again by the Rotor Model. Low Mach number preconditioning was employed to accurately predict the flow, especially in the proximity of the wing. Three meshes were employed in this simulation: a cylindrical rotor mesh, a C-O wing mesh and a Cartesian background mesh. A span wise section of the wing mesh is shown in Figure 3.24. The rotor system is situated 0.42 rotor radii above the wing surface, with the center of the rotor offset by 0.1 rotor radii outward from the wing tip. The rotor is trimmed by iteratively modifying the collective to obtain a thrust coefficient of 0.0186. A total of 1.7 million points were used in the three grids.

Velocity vectors at a plane close to 0.5 c (mid chord), as shown in Figure 3.25, are depicted in Figure 3.26. The velocity vectors are colored appropriately for the C_{pDL} values at those

grid points. The span wise flow across the wing along with the high pressure on the top surface of wing is clearly evident in this figure. One can also note the splaying of the wake boundary as it impinges upon the wing, rather than the continued contraction observed when the wing is not present. C_{pDL} distribution over the wing surface was measured at the four span wise locations on the wing shown in Figure 3.25. The pressure comparison at these locations is shown in Figure 3.27. The pressure data at the flaps was not available for the experiment and is not shown in the figure. The pressure distribution matches fairly well with that from the experiment, although there are some differences close to the leading edge on the top surface. Especially of note is the accurate prediction of the base pressure on the bottom surface of the wing. The previous comparison of an isolated rotor confirmed the accuracy of the axial velocity below the rotor, the comparison of pressure measurements also confirms the accurate modeling of the swirl introduced into the flow by the rotor. Furthermore, the reduced downwash at the 0.9 R span wise location results in the reduced pressure predicted and measured on the upper surface. Also, it can be noted that the stagnation point on the top surface moves toward mid chord as the wing root is approached. This fair comparison with the experimental results leads the way for simulation of the current problem of the QTR.

To analyze the effect of rotor swirl on the wing loading, the rotor was rotated in the opposite direction and very different pressure variation at these sections was obtained and are shown in Figure 3.28. The flap was observed to produce an upload in the original case, but produces a high download with the reversed rotation of the rotor. In the reversed rotation case, the rotor spins from the trailing edge of the wing towards to leading edge, inducing the swirling flow to stagnate on the top surface of the flap and lead to a download on the flap.

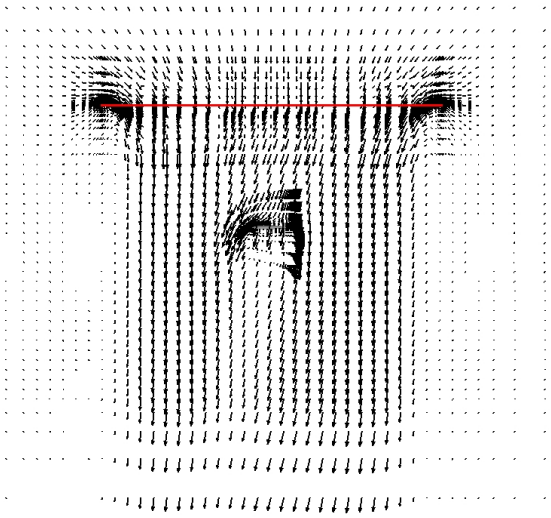

(a) Vertical climb ($\mu = 0.01$)

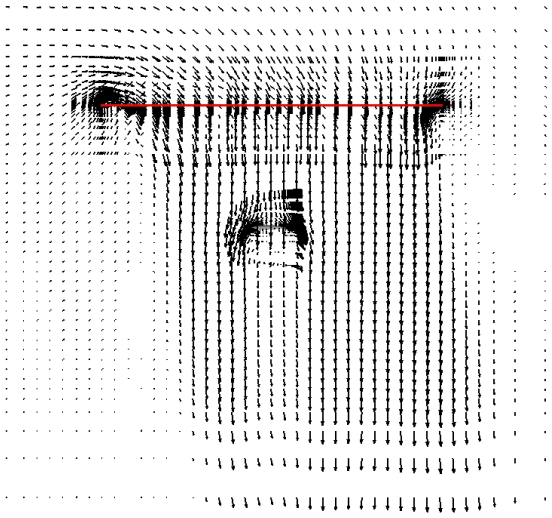

(b) Forward flight (μ=0.01)

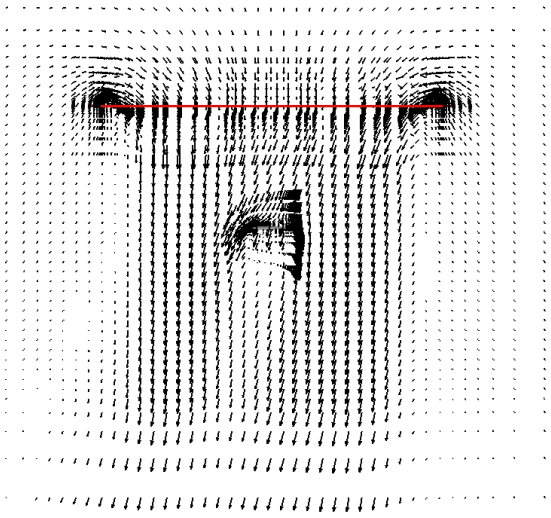

(c) Vertical descent ($\mu = 0.01$)

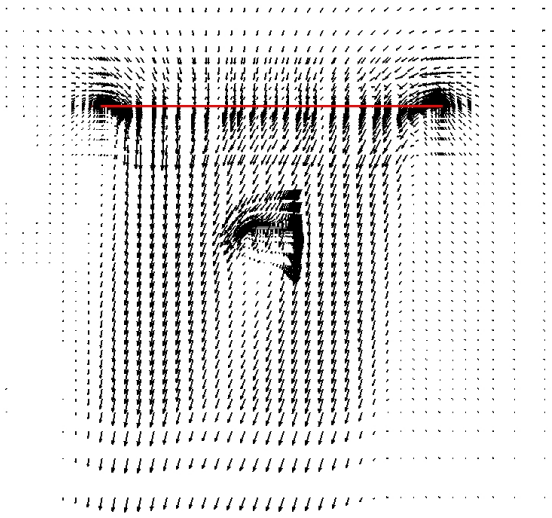

(d) Backward Flight($\mu = 0.01$)

Figure 3.9: Velocity vectors in a span wise plane through the rotor disk.

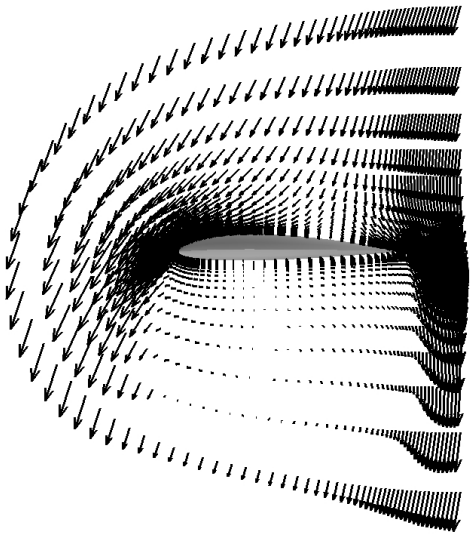

(a) Vertical climb (λ_c = 0.01)

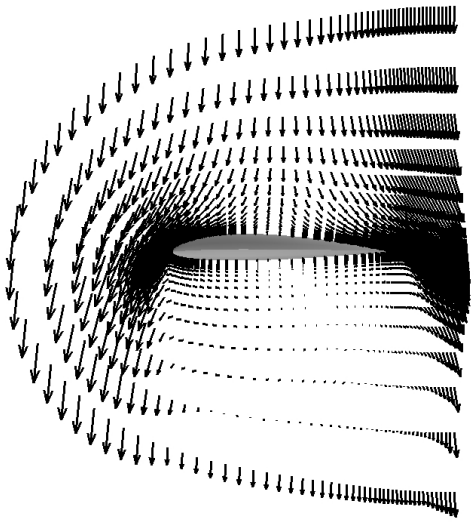

(b) Forward flight (μ = 0.01)

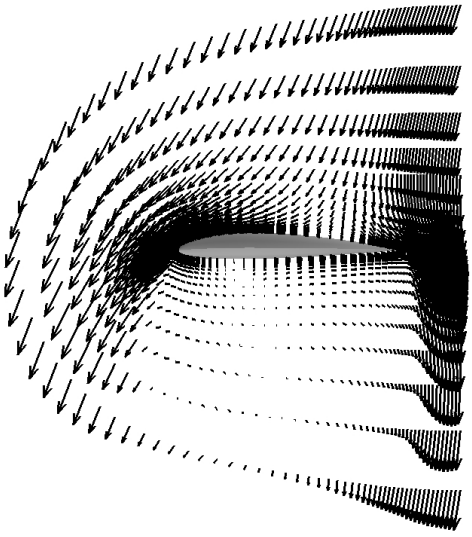

(c) Vertical descent (λ_c = -0.01)

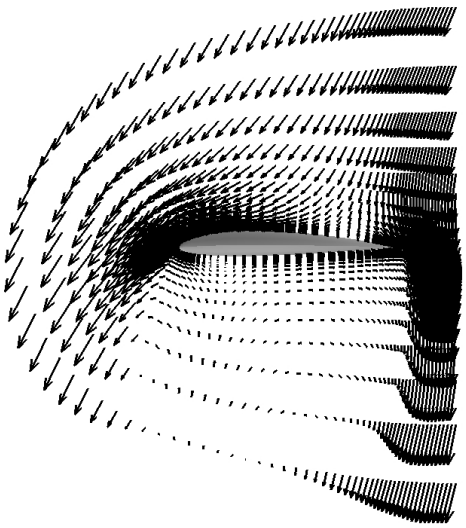

(d) Backward Flight(μ = -0.01)

Figure 3.10: Close up of velocity vectors around the wing at 84% of span.

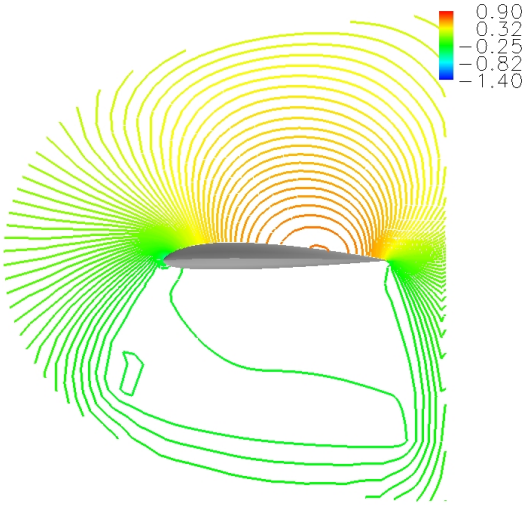

(a) Climb ($\lambda_c = 0.01$)

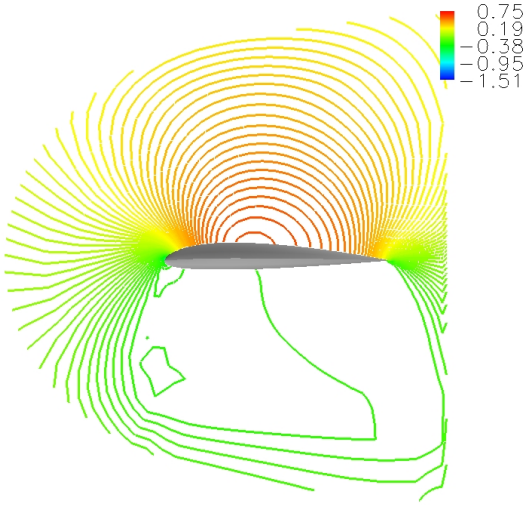

(b) Forward flight (μ=0.01)

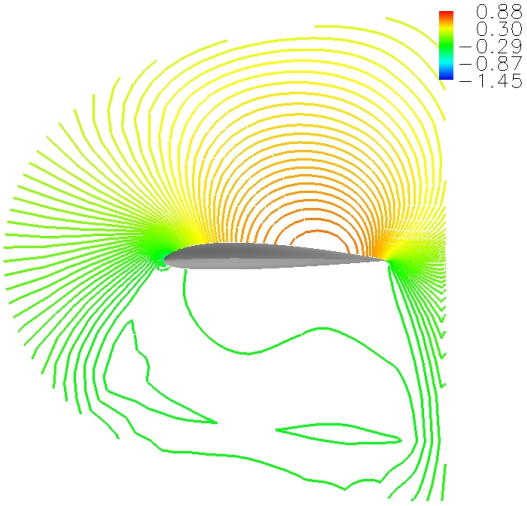

(c) Vertical Descent (λ_c=-0.01)

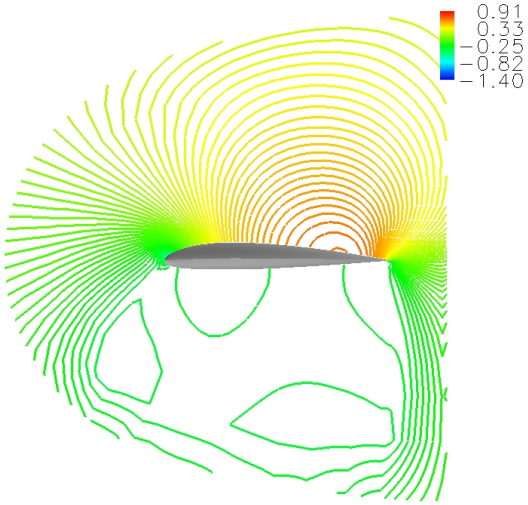

(d) Backward Flight(μ=-0.01)

Figure 3.11: C_{pDL} contours at the 84% wing span.

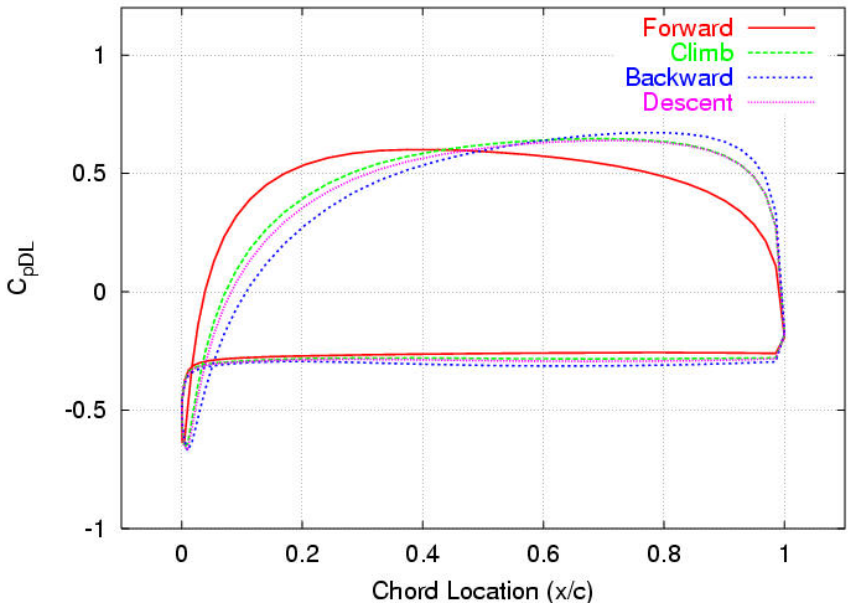

Figure 3.12: Comparing C_{pDL} at 84% wing span location for $\mu = 0.01$.

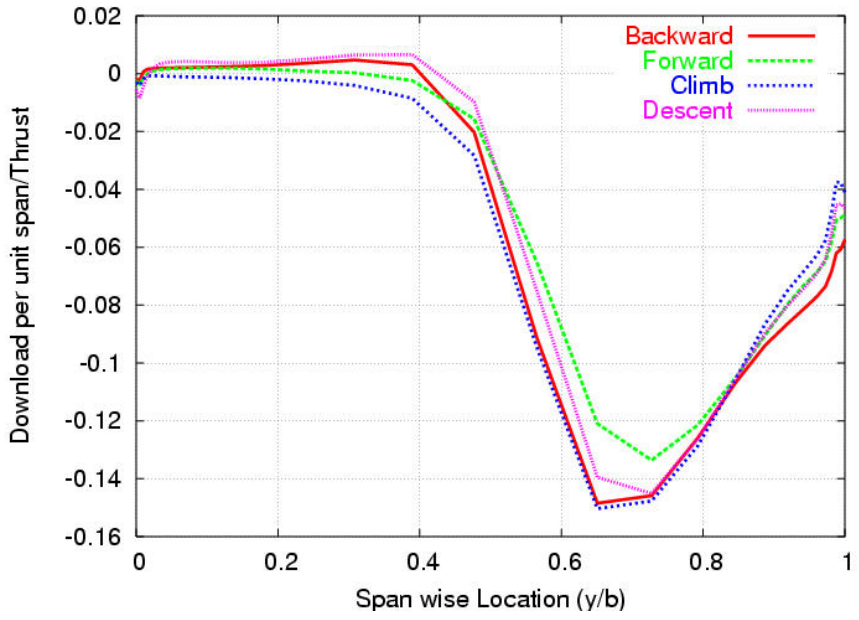

Figure 3.13: Loading on the wing as a fraction of rotor thrust in the span wise direction for $\mu = 0.01$.

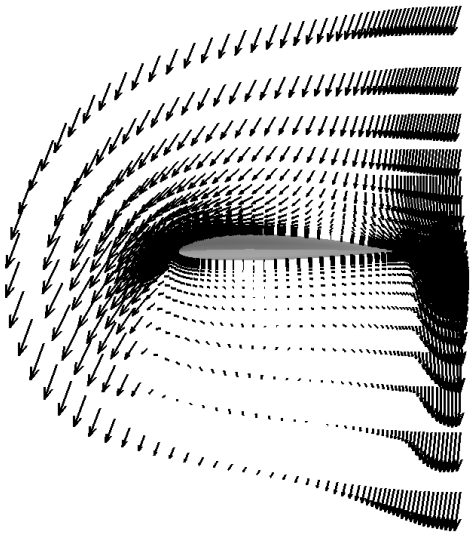

(a) Vertical climb ($\mu = 0.002$)

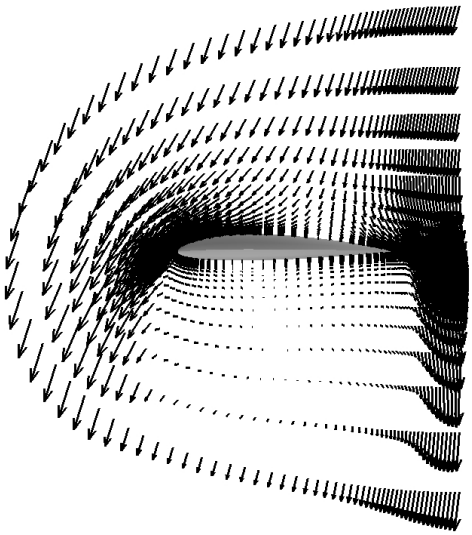

(b) Forward flight ($\mu = 0.002$)

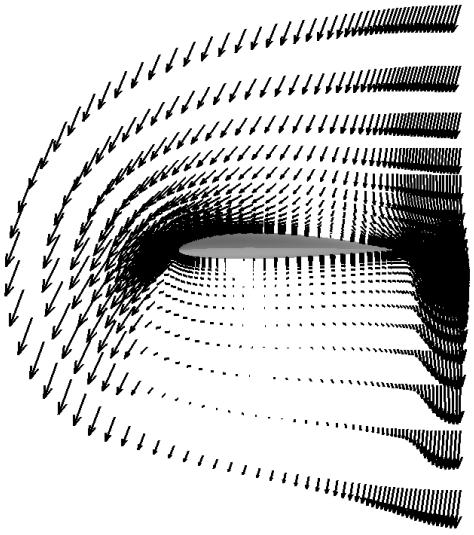

(c) Backward flight ($\mu = 0.002$)

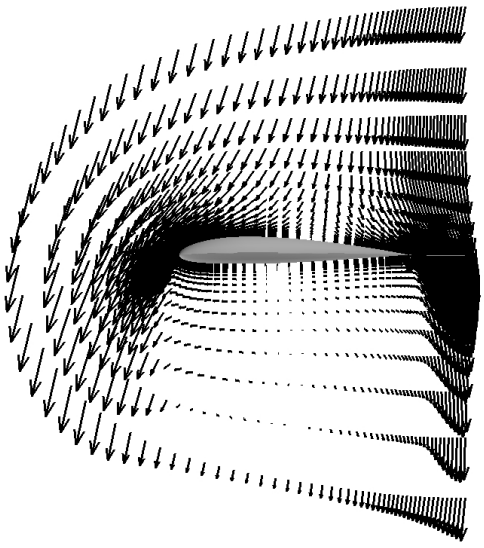

(d) Sideward flight ($\mu = 0.002$)

Figure 3.14: Close up of velocity vectors around the wing at 84% wing span.

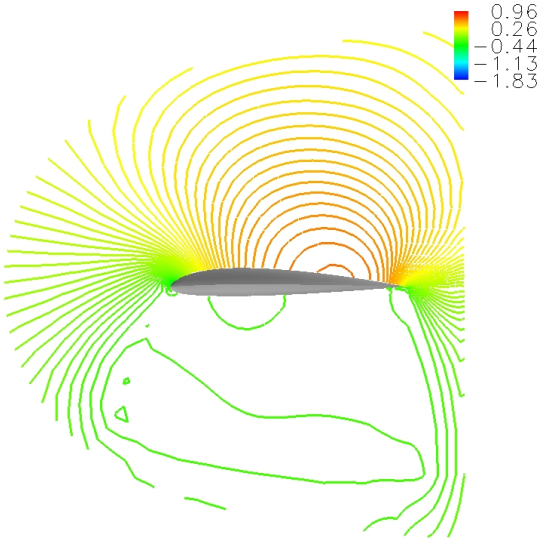

(a) Climb ($\mu = 0.002$)

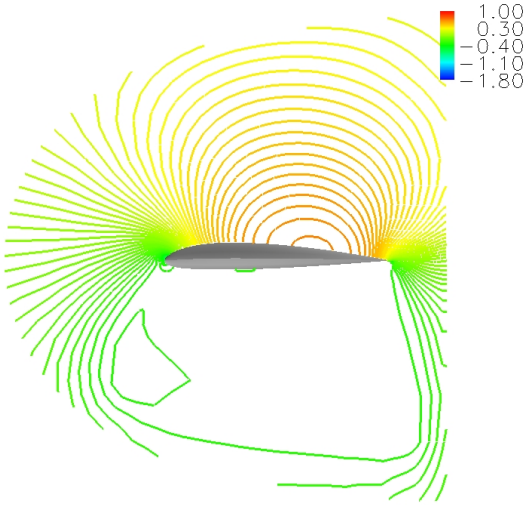

(b) Forward flight ($\mu = 0.002$)

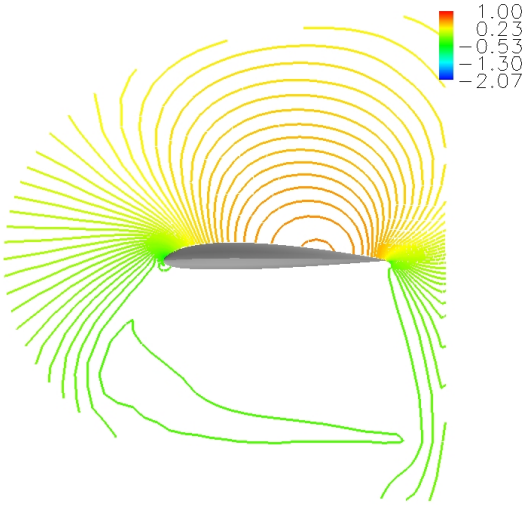

(c) Backward flight ($\mu = 0.002$)

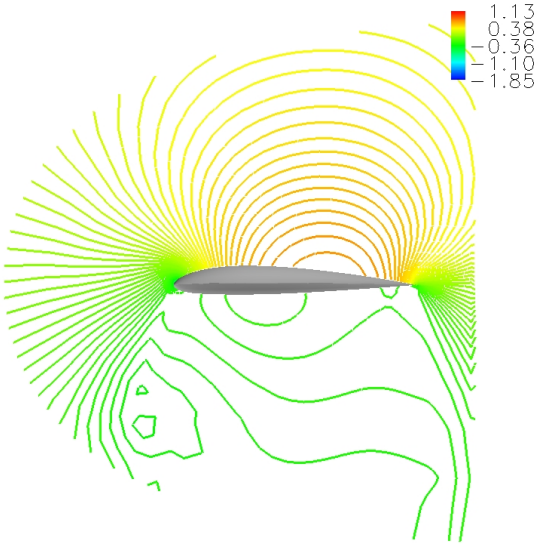

(d) Sideward flight ($\mu = 0.002$)

Figure 3.15: C_{pDL} contours at 84% wing span location.

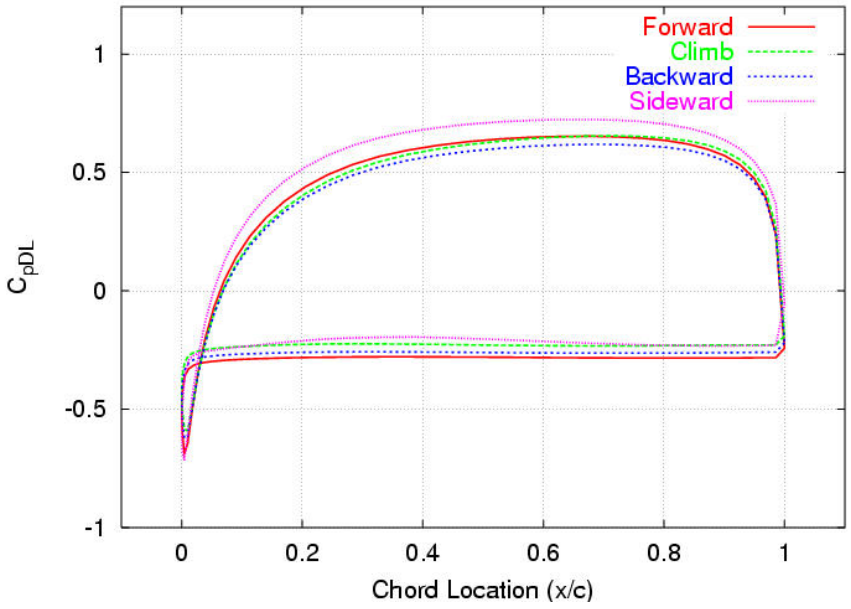

Figure 3.16: Comparing C_{pDL} at 84% wing span location for $\mu = 0.002$.

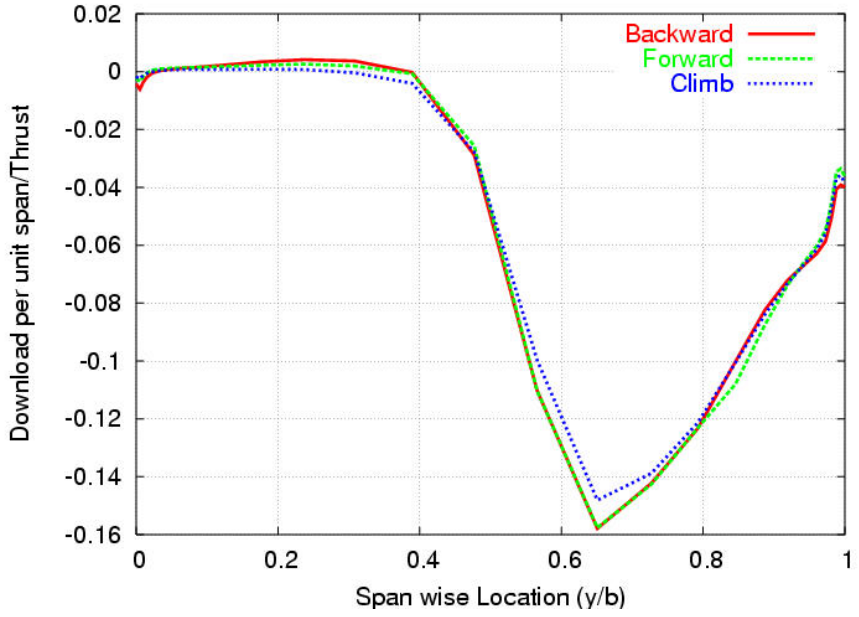

Figure 3.17: Lift on the wing in the span wise direction for $\mu = 0.002$.

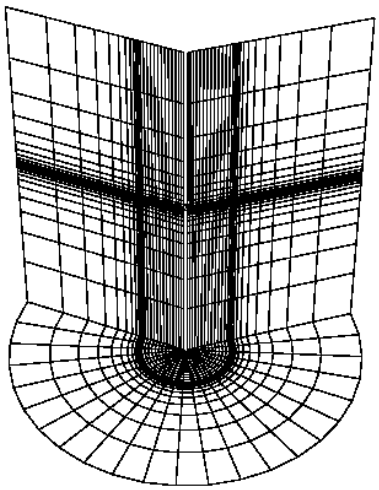

Figure 3.18: Cylindrical grid used to simulate the rotor model for validation.

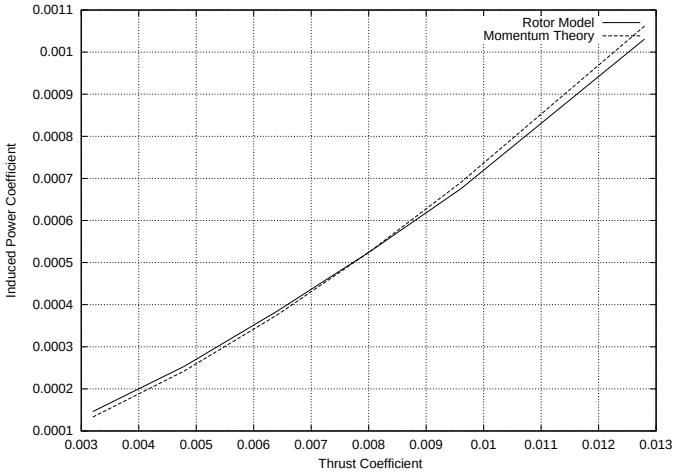

Figure 3.19: Curve between thrust coefficient and induced power coefficient (OGE; Induced power factor included in Momentum Theory).

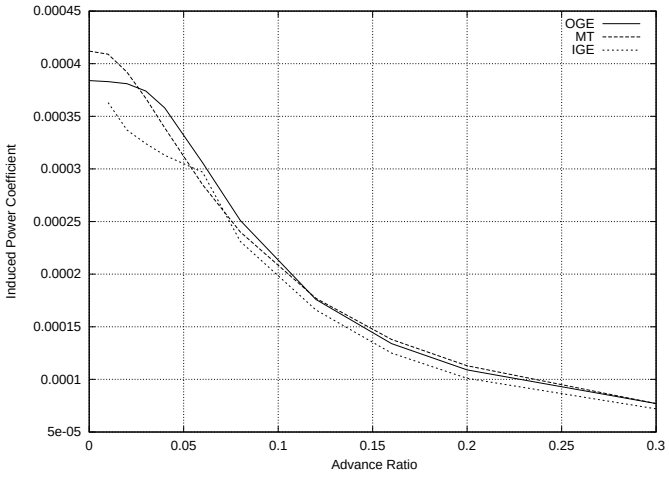

Figure 3.20: Induced power coefficient as a function of advance ratio.

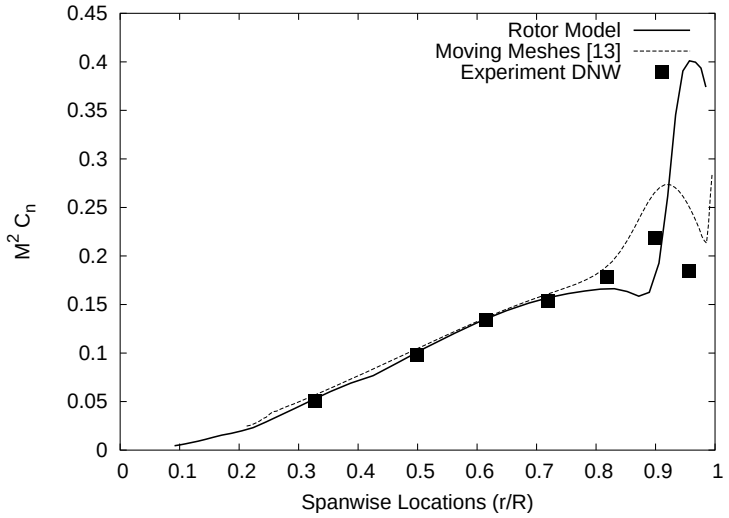

Figure 3.21: Non-dimensional force distribution on the rotor for $C_t = 0.0149$.

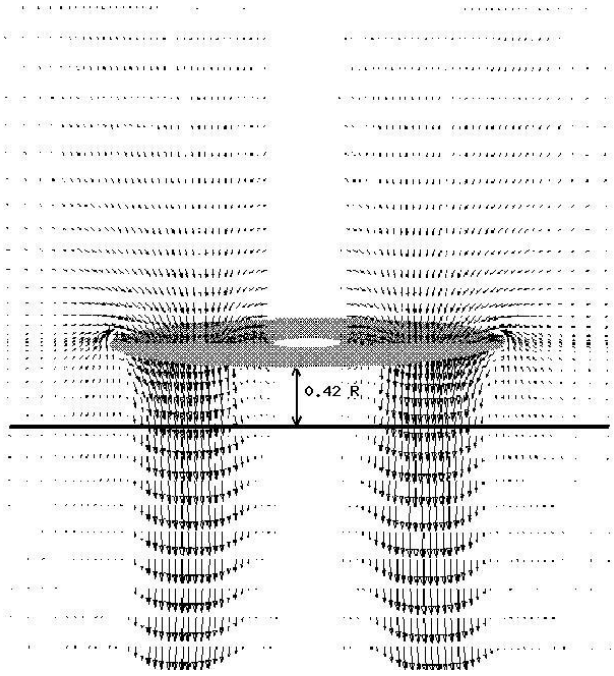

Figure 3.22: Velocity vectors in an azimuth plane of the rotor flow field for $C_t = 0.0164$.

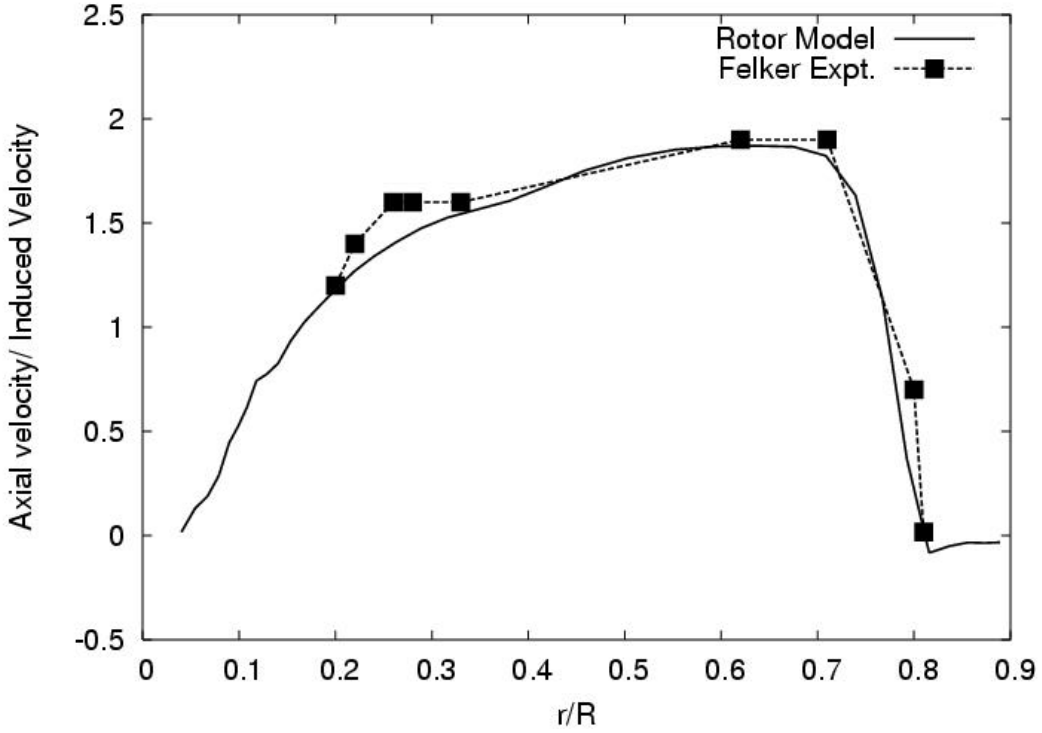

Figure 3.23: Axial velocity distribution at 0.42 R below the rotor for $C_t = 0.0164$.

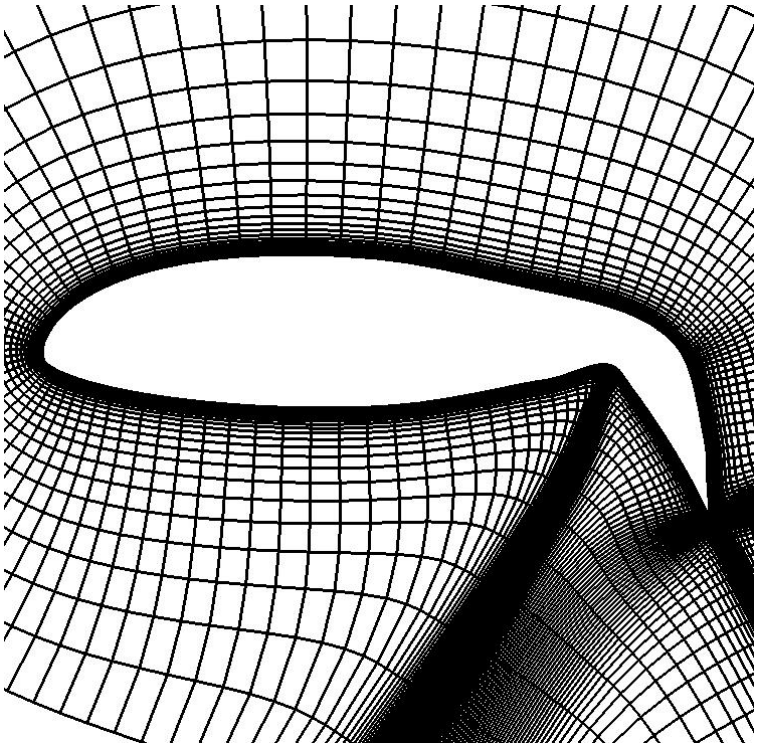

Figure 3.24: Span wise section of the wing grid.

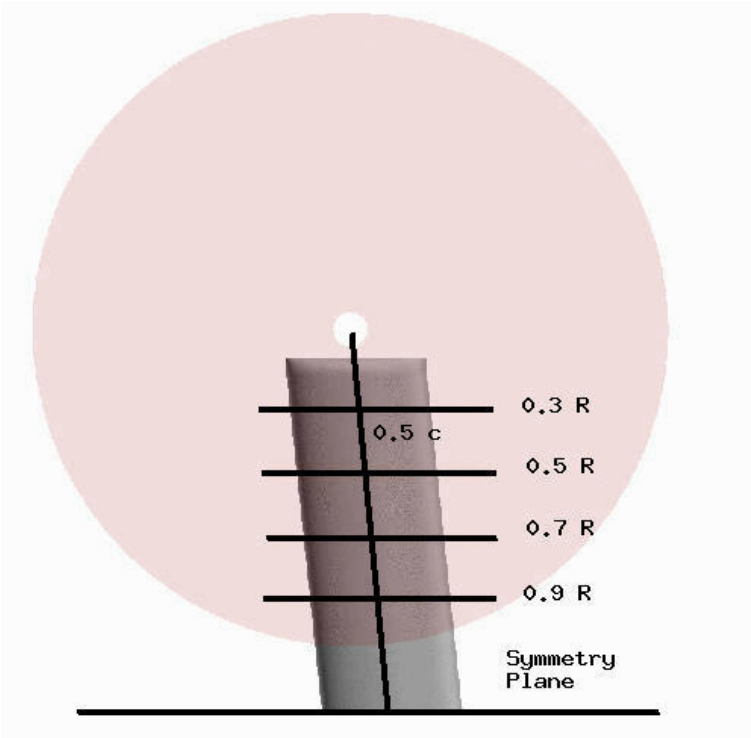

Figure 3.25: Top view of the set up of experiment showing the pressure tab locations.

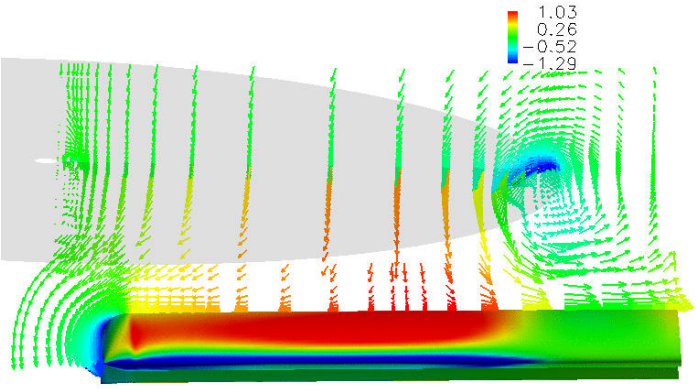

Figure 3.26: Velocity vectors at a plane close to 0.5 c colored by C_{pDL}.

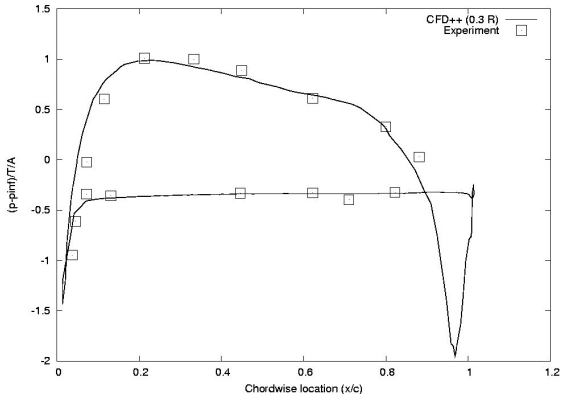

(a) 0.3 R

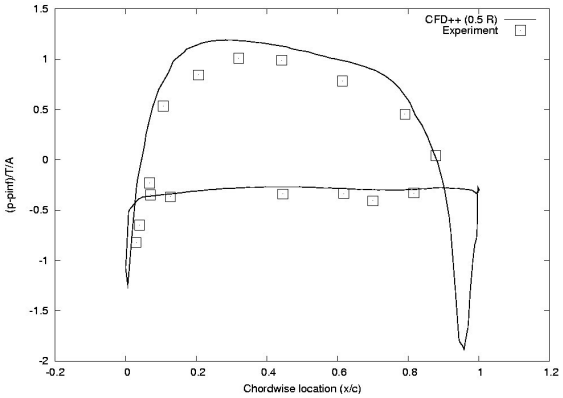

(b) 0.5 R

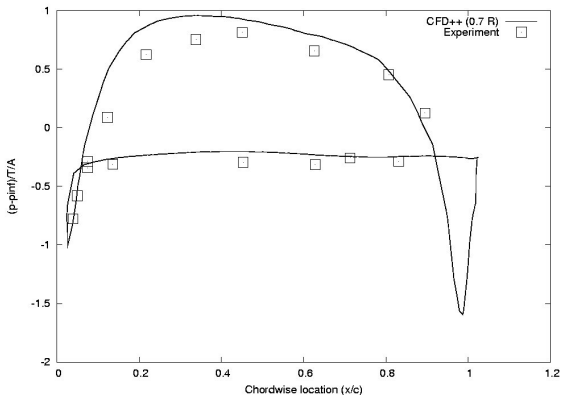

(c) 0.7 R

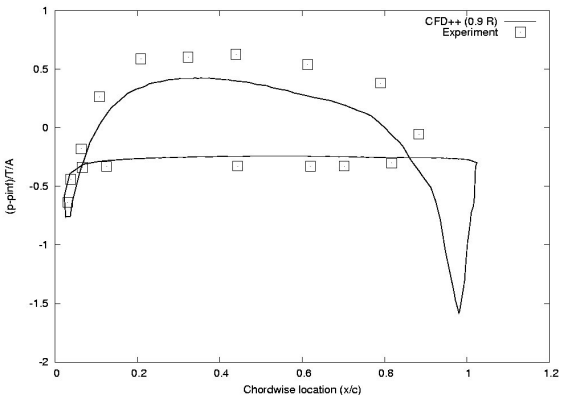

(d) 0.9 R

Figure 3.27: Non-Dimensional pressure comparison with Felkers' Experiment.

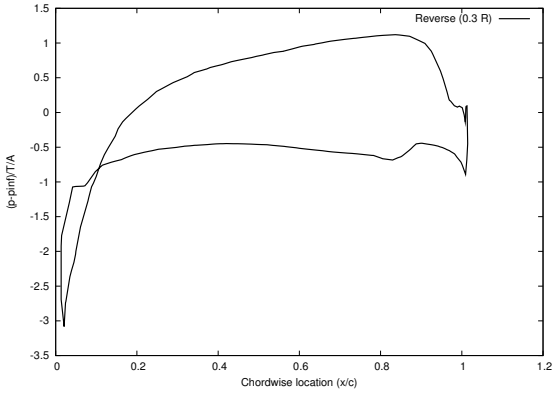

(a) 0.9 R

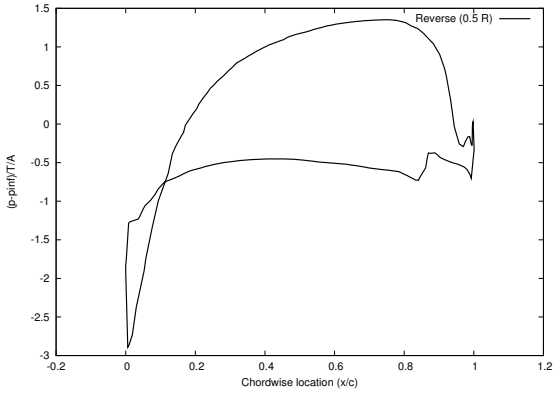

(b) 0.9 R

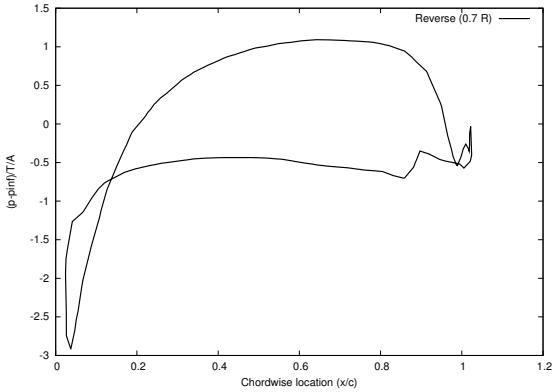

(c) 0.9 R

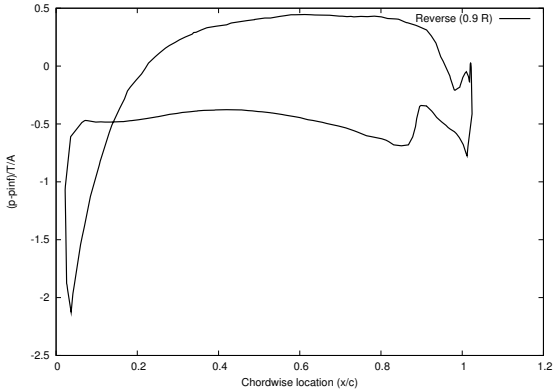

(d) 0.9 R

Figure 3.28: Non-Dimensional pressure variation with reverse rotation.

Chapter 4

Geometry and Grids Details of Quad Tilt Rotor

Grid generation is an integral part of any CFD simulation. It is very important to generate a good grid with sufficient number of points in the regions of high gradients and fewer points in other regions where the gradients are not large. Judicious distribution of points saves computational resources along with resolving high gradients in regions of interest. Accuracy and convergence of a solution is highly dependent on the quality of the grid. All the improvements in the solver algorithm would be futile if the grid employed is not sufficiently fine. Other properties such as orthogonality and stretching of the grids are also very important and have been appropriately chosen to accelerate convergence and obtain accurate solutions. The simplified geometry of the Quad Tilt Rotor followed by the grids employed is discussed in this chapter.

4.1 Simplified Geometry

A simplified model of the Quad Tilt Rotor is used for conducting the download study in the helicopter mode. The geometry employed is not a replica of the proposed Quad Tilt Rotor, however it is equipped with sufficient details and is a good representation of the Quad Tilt Rotor. The airfoil section for the wings is chosen to be the same as that for the V-22 wing.

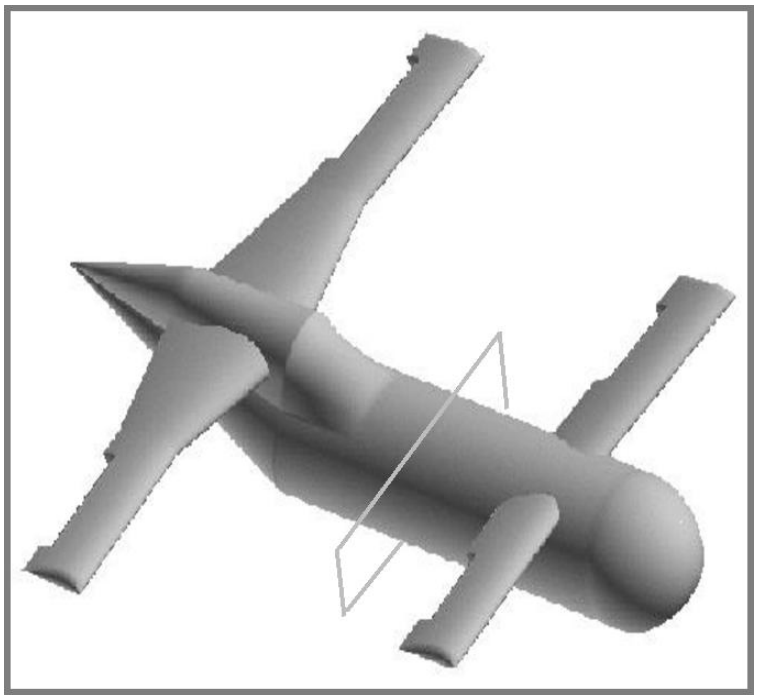

Figure 4.1: Simplified geometry of the Quad Tilt Rotor without rotors.

Flaps are modeled on both the front and rear wing as a means of download reduction in hovering flight. The flaps are deflected by 67 degrees, because the download was observed to be minimum at this setting in hovering flight [7]. The bottom surface of the fuselage is flatter, since it is observed to aid in download reduction, when the QTR operates close to the ground. The top surface of the fuselage is raised for better definition of the intersection of the rear wing with the fuselage. The nacelles and pylons are not modeled, because their contribution to the download for V-22 is observed to very small [28]. The geometry of the QTR used for all the flight conditions is shown in Figure 4.1. The cross-section of the fuselage is shown in Figure 4.2.

4.2 Grid Topology

Overset meshes are utilized to model the complicated geometry of the Quad Tilt Rotor. Body conforming meshes along with a background Cartesian mesh are generated in this

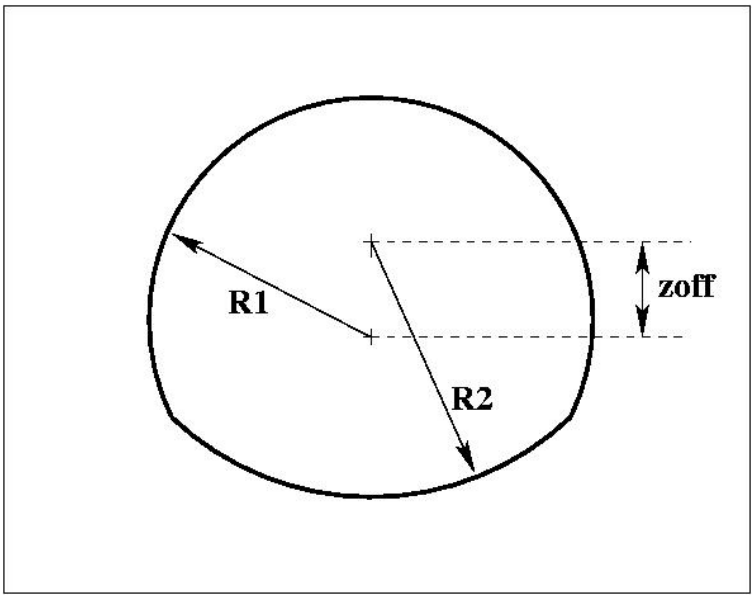

Figure 4.2: Cross-section of the fuselage modeled (R1 = 7.1 feet, R2=11.2 feet, zoff = 5.0 feet).

approach for the various components of the QTR, namely front wing, rear wing, fuselage, front rotor and rear rotor. Connectivity information between the grids is obtained once the grids are generated. The topology of these grids is explained next.

4.2.1 Rotor Grid

Each rotor system is modeled as a disk in the middle axial plane of a cylindrical grid. The axial spacing on the two sides of the disk is approximately 0.004 times the radius and increases as a geometric progression in the axial direction away from the disk. The mesh spacing is maintained to be very fine, approximately 0.003 times the rotor radius, at the root and the tip of the disk in the radial direction, in order to capture the shear layer at the tip and better approximate the tip loss effect. The grid used to model the rotor system is shown in Figure 4.3. This grid did not extend to the far field, because the background Cartesian grid takes care of the far field boundary condition. All the four rotors have the same dimensions.

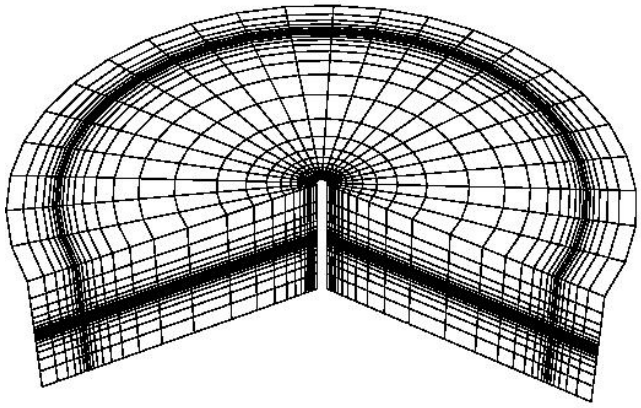

Figure 4.3: Cylindrical grid for modeling the rotor.

4.2.2 Wing Grid

The wings are modeled as a C-O grid shown in Figure 4.4. The C mesh around each wing section (A821201) is generated by solving hyperbolic equations at various span wise locations and then joined to each other to get a three dimensional mesh. The top and bottom halves of the span wise grid near the wing tip are rotated in opposite directions around the wing tip until they collapse to a plane. The rotation of grid lines in Figure 4.4 near the wing tip is a clear indication of the rotation of the span wise planes. This rotation of the span wise planes gives a better definition to the wing tip. Flaps deflected at 67^o are included in both wings. Same length of the flap is used on both wings. A smooth transition from the flap to wing is

achieved by interpolating between the two airfoil definitions over a few span wise locations. Air gap between the flap and the wing is not modeled as a consequence. Air gaps between the flap and the wing are treated as solid surfaces. A close up of this region is shown in Figure 4.5. Fine spacing (10^{-6} chord) in a direction normal to the body surface is used in order to better capture the boundary layer on these surfaces. Employment of a C-O mesh ensures fine spacing at the wing tip also. The outer boundary of the grid is approximately 2 chords away from the wing surface. The conservative variables and turbulent viscosity on the outer boundary are interpolated from the background or other near body meshes.

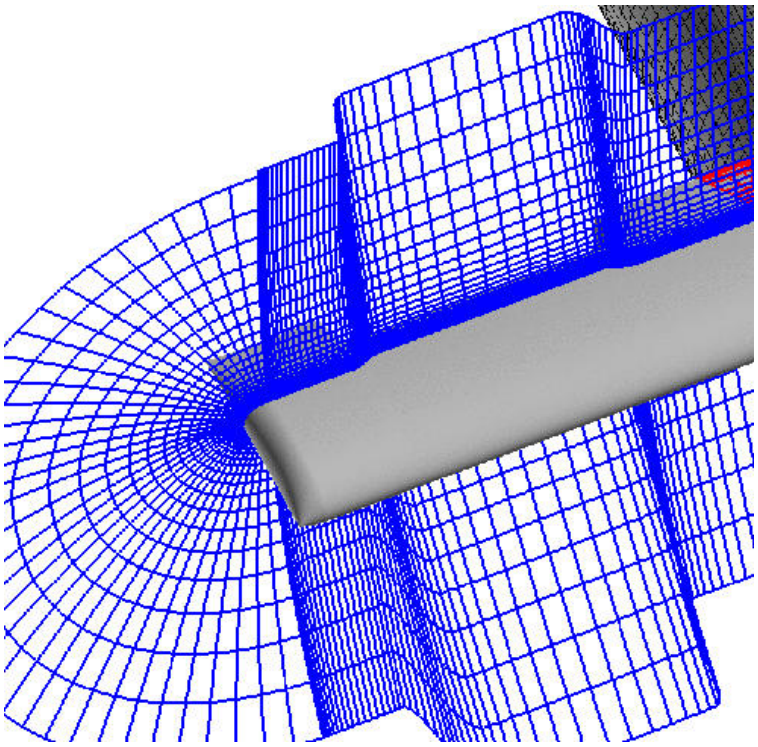

Figure 4.4: Grid for modeling the front wing.

4.2.3 Fuselage Grid

A simplified fuselage geometry with a flatter bottom and raised top surface is generated. An algebraic O-O grid (shown in Figure 4.6) is generated around the fuselage, with the cell spacing increasing in a direction normal to the fuselage wall. The singular lines at the nose and the tail of the fuselage are treated as axis and the conservative variables and turbulent viscosity are averaged in the wrap around around direction to obtain the conservative variables and turbulent viscosity at these singular lines. The grid generated is finer in the longitudinal direction in the region where the wings intersect the fuselage. The outer boundary of the fuselage mesh is approximately one wing chord away from the surface.

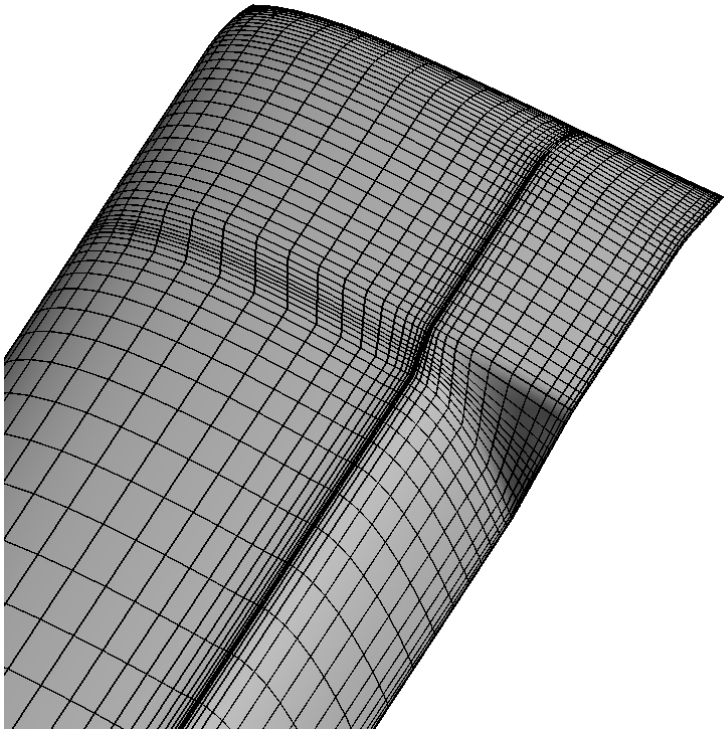

Figure 4.5: Transition from the flap mesh to the wing mesh for the front wing.

4.2.4 Collar Grid

The span wise direction of the wing is parallel to the fuselage normal close to the fuselage surface and the grid spacing in the span wise direction in the wing grid is not as fine (0.01 chord) as the normal spacing (10^{-6} chord) on the fuselage surface. Hence, the information transfer will not be adequate without the employment of a collar mesh at the junction of the wing and the fuselage. The collar meshes are generated at the junction of the front wing and the rear wing with the fuselage. These meshes begin from the intersection of the fuselage surface and the wing surface and propagate along the wing surface in one direction and along the fuselage surface in the other direction. Normal spacing similar to the wing mesh and the fuselage mesh can be maintained by adopting collar meshes. The collar meshes for the front wing and the rear wing intersections with the fuselage are shown in Figures 4.7 and 4.8, respectively. The collar meshes extend in the wing span wise direction until the spacing on the collar meshes is similar to the spacing on the wing mesh in the span wise direction.

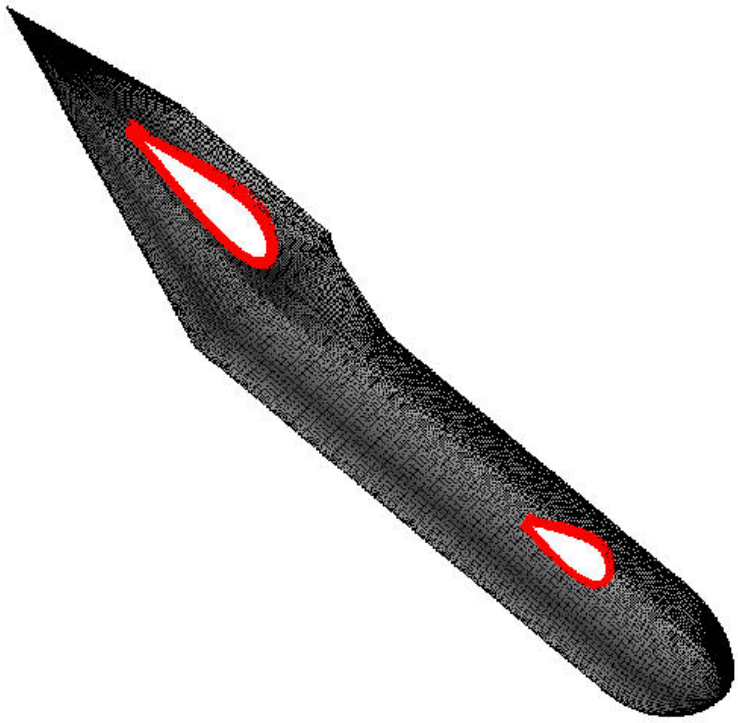

Figure 4.6: Grid for modeling the fuselage.

Also the extent of the collar mesh in a direction parallel to the fuselage surface is dictated by the spacing on the fuselage mesh.

4.2.5 Background Cartesian Mesh

A background Cartesian grid is used to specify the far field boundary conditions and information transfer between the various grids. The Cartesian grid extends up to at least three rotor diameter outside the aircraft body for the out of ground effect cases. The conservative variables and turbulent viscosity are interpolated at the boundaries of the near body meshes from the Cartesian mesh and other intersecting near body meshes, enabling the exchange of information between the meshes. A minimum of two cell overlap is maintained between the grids for smooth transfer of information between the grids. The spacing of the background Cartesian grid (shown in Figure 4.9) is increased in levels, with a fine grid spacing in the region where the body conforming meshes lie, i.e. the cylindrical grids, fuselage grid and

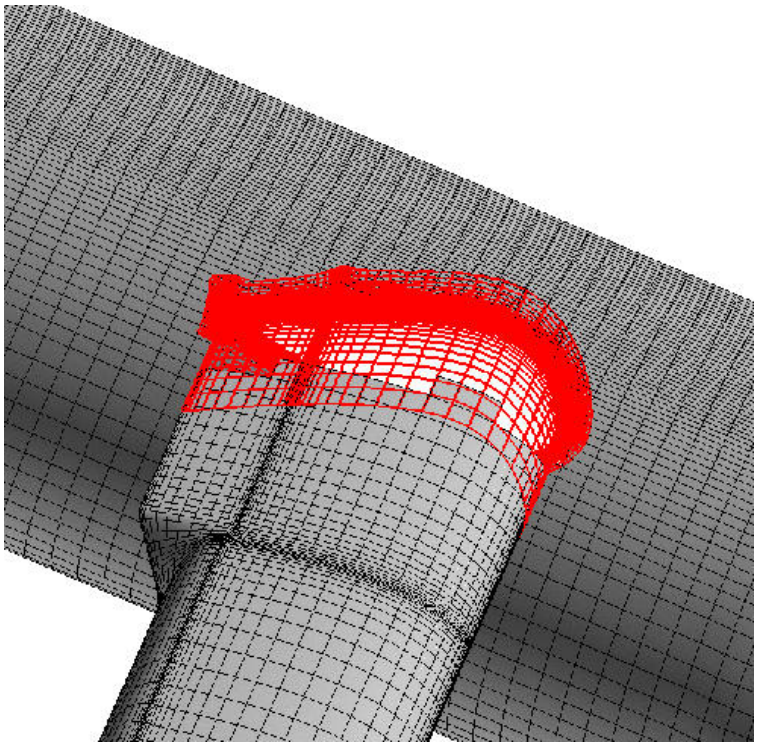

Figure 4.7: Grid for modeling the juncture between the fuselage and the front wing.

meshes around the wings and a coarse grid spacing beyond it. Fine spacing of the Cartesian mesh in this region ensured better information transfer between the grids. The coarse grid spacing in the region of less significance is used to reduce the total number of grid points. The Cartesian grid for the in ground effect cases, shown in Figure 4.10, has fine spacing near the ground plane, to better simulate the effect of the ground plane, which is modeled as a moving viscous wall. The velocity of the wall is set to be the free stream velocity providing a better approximation of the ground plane. The dimensions of the grids are shown in Table 4.1. A total of approximately 5.7 million mesh points are used to simulate the QTR in the present study.

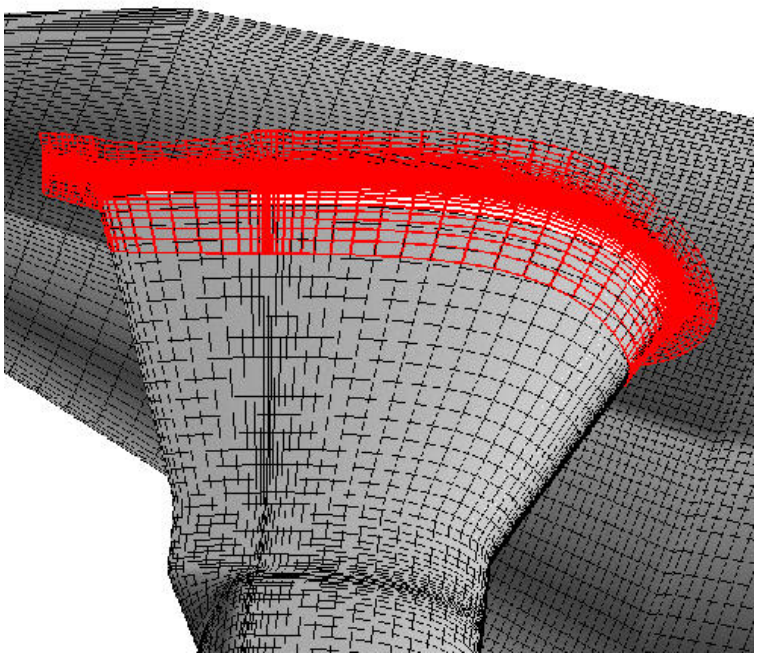

Figure 4.8: Grid for modeling the juncture between the fuselage and the rear wing.

4.3 Connectivity

As stated earlier, in an overset mesh approach several meshes may overlap in the same region. If grid points of a near body or background mesh lie inside a solid body of a near body mesh, they need to be alienated from regular grid points. This process of isolation of these invalid points is called Hole cutting. A vertical plane through the front wing is shown in Figure 4.11. This plane clearly elucidates the hole cutting done for the current set of grids. It can be observed from the figure that the background mesh(red) is removed from the regions where the fine near body meshes are present, but still maintains sufficient overlap for information transfer. The near body meshes receive information at the far away boundary from the solid surface from other meshes, depending on which mesh those points lie in. The newly generated boundary visible on the background mesh as a result of hole cutting receives information from near body meshes. Similar boundaries are created in other

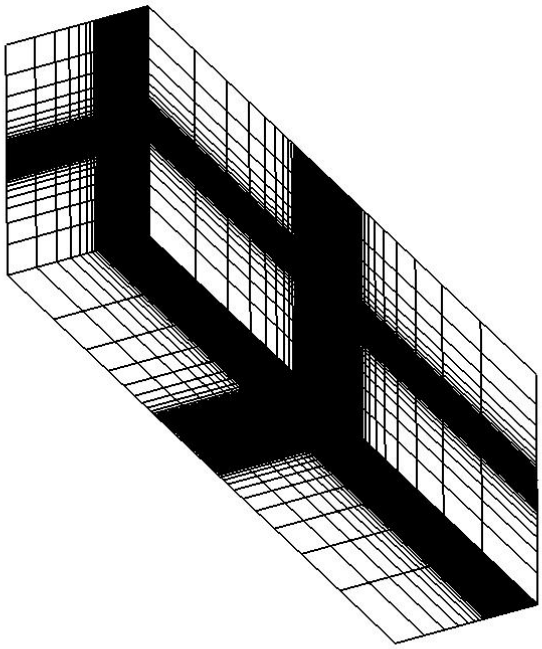

Figure 4.9: Background Cartesian mesh for OGE.

meshes also, for instance in the front wing mesh (blue) as a result of hole cutting because of the fuselage. The process of hole cutting and then finding donor points for the points on the chimera boundaries and far away boundaries on the near body meshes along with interpolation sets is carried out maintaining at least two layer overlap between the meshes for smoother transfer. Same tools are utilized to generate the connectivity data for both OGE and IGE grids.

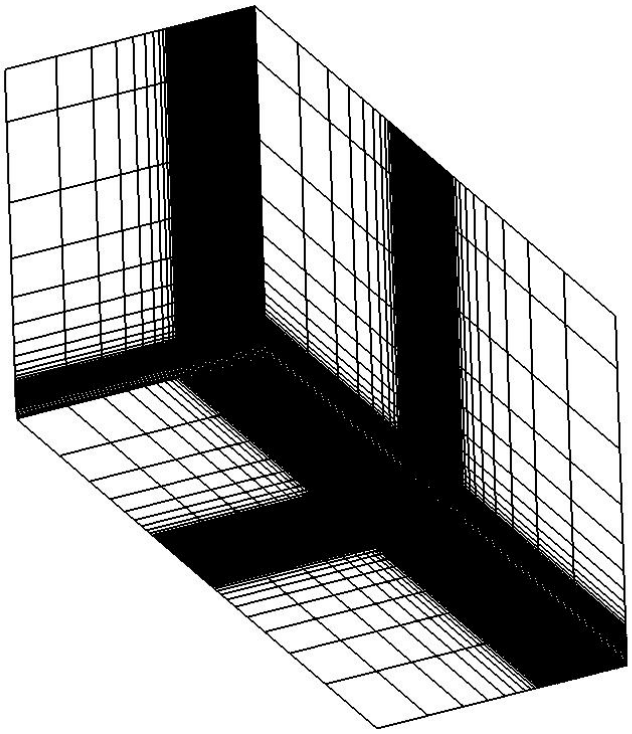

Figure 4.10: Background Cartesian mesh for IGE.

Table 4.1: Grid Dimensions.

Grid	JMAX	KMAX	LMAX	Points
Front Rotor	35	73	57	145635
Rear Rotor	35	73	57	145635
Front Wing	151	99	56	837144
Rear Wing	151	111	63	1055943
Fuselage	161	91	71	1040221
Front Collar	109	50	44	239800
Rear Collar	109	50	38	207100
Cartesian	141	121	121	2064381

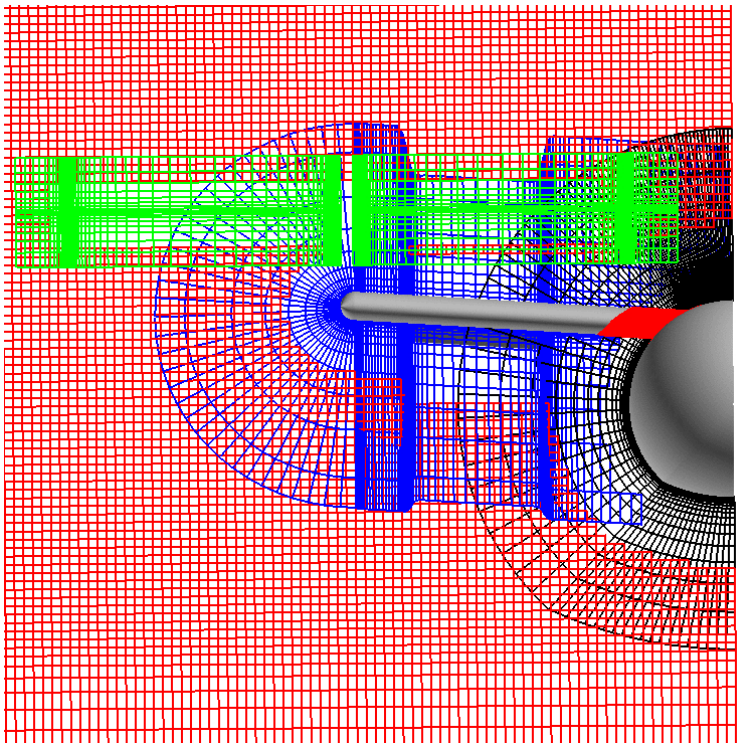

Figure 4.11: Longitudinal plane illuminating hole cut grids.

Chapter 5

Hovering Flight of the Quad Tilt Rotor

Several configurations and ambient conditions are simulated for the modeled Quad Tilt Rotor (QTR) in hover and forward flight mode, enabling prediction of its performance in these conditions and configurations. Overset meshes, described in the Methodology chapter, are utilized to model the complicated geometry of the QTR. The grids described in the previous chapter, are utilized to obtain solutions for the flow field around the QTR. Low Mach number preconditioning as explained in the Preconditioning section is employed to obtain more accurate solutions with a smaller turn around time. Hovering flight is approximated by simulating a climb rate of 1.5 ft/second. This climb velocity is 2-3 % of the induced velocity of the rotor and its effect on the download is observed to be small (0.5% of the total thrust). This was previously confirmed by simulating the rotor-wing interaction at these free stream velocities (1.5 ft/sec) but approaching the aircraft from different directions. Small differences were observed in the download distribution on the wing for these flight conditions, ensuring the closeness of any of these flight conditions to hovering flight.

A simplified QTR is simulated in hovering flight and described in this chapter. The effect of ground plane is analyzed on the performance of the aircraft by simulating the conditions in which the wheels of the aircraft are on the ground, 10 feet off the ground and far away from the ground. The two modes of operation (In Ground Effect; Out of Ground Effect) are drastically different in terms of flow patterns observed (described in the Introduction chapter). These flow patterns along with pressure distribution over the wings are analyzed

in great detail in this chapter. The differences in flow patterns in these two regimes of flight are highlighted and their influence on the loading distribution is investigated and explained.

5.1 Out of Ground Effect

Three span wise locations are selected on both the front and rear wings to examine the chord wise variation of C_{pDL}, which was defined previously in the Validation chapter. These locations are situated at 0.3 R, 0.5 R and 0.7 R from the rotor center (wing tip) and are shown in Figure 5.1. The chord wise variation of C_{pDL} (Figure 5.2) reveals that it is approximately a constant at the bottom surface at these sections for both wings, suggesting a large region of separated flow below the wing. A very high negative C_{pDL} is observed at the leading edge because of the acceleration of the flow around the curved leading edge. The flow is observed to begin to accelerate earlier close to the leading edge on the top surface of the rear wing than for the front wing. This causes a gradual gradient of C_{pDL} along the top surface for the rear wing; and as a result, a reduction in downward force at these sections is expected. The area between these closed curves suggests a higher downward force on the front wing sections than the rear wing sections. The flaps are observed to produce an upward force, because of the acceleration on the top surface of the flap. It is also noted that the pressure on the upper surface of the wings on the sections below the outer portions of the tip of the rotors is reduced compared to that toward the wing tips due to the expected lower downwash in that region, similar to that observed experimentally and computationally for the isolated rotor wing interaction.

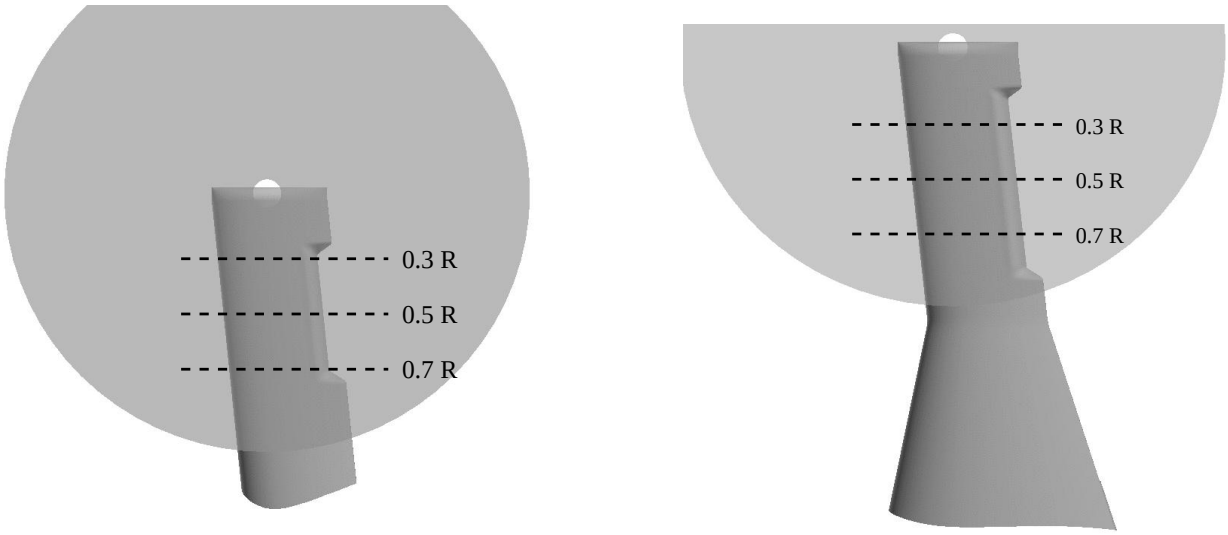

(a) Front Wing

(b) Rear Wing

Figure 5.1: Span wise stations on the wings.

The loading on the wings is integrated at all span wise locations and plotted as a ratio of thrust per unit span for both wings in Figure 5.3. It can be noted from the figure that the front wing experiences a higher download per unit span than the rear wing as was partly explained by the span wise C_{pDL} plots. The rear rotors are further apart as compared to the front set of rotors. This larger span wise separation for the rear rotors provides a larger region for the diffusion of high downwash velocities from the rotor. In addition, it is now seen that the inner portion of the rear wing experiences a small upward force. The small upward force is a ramification of the span wise flow observed on the top surface, reducing the pressure and providing lift.

The velocity vectors a short distance above the surface, along with the pressure variation, are shown in Figure 5.4. A top view is shown in the top half of the figure and a bottom view is shown in the bottom half of the figure. Chord wise and span wise flow on the top surface of both wings is clearly visible. Span wise flow is more prominent for the rear wing, as it persists for a longer distance, because of the rotors being further apart. High pressure

regions (red) can be seen on the wing surfaces, suggesting a strong downward force. Flow at the bottom surface is more quiescent than at the top surface. There is a clear indication of span wise flow close to the tip of both wings on the bottom surface. The strong rotor downwash out past the wing tip is pulled toward the center, because of the lower pressure below the wing, as was shown in the C_{pDL} plots.

Vertical planes to be used for a more detailed flow description are shown in Figure 5.5. Velocity vectors at vertical planes through the front (plane 1) and the rear wing (plane 2) are shown in Figure 5.6. The colors of the velocity vectors depict the magnitude of the vertical velocity. The velocity field from fine near-body meshes is interpolated on to the Cartesian mesh for clarity, even though solution is obtained utilizing finer meshes. Velocity vectors impinging upon the wing surface and then turning in the span wise direction are clearly observed in the figure. High speed downward streams outside the wing tips are observed at both the front and rear wing planes. These streams attempt to contract towards each other below the QTR vehicle, populating the region between them. The region directly below the rear wing appears more quiescent than the region below the front wing since the rotors are further apart. Eventually, in the far field the downwash from the various rotor systems are seen to merge.

5.2 In Ground Effect

The repercussions of the presence of the ground plane when operating IGE are not very well understood for tilt rotor vehicles. The upload producing or download diminishing mechanism described briefly earlier (Introduction chapter), is explained in more detail in this section by examination of the CFD simulation of the simplified QTR geometry operating IGE in hover.

5.2.1 Wheels on Ground

This condition is with the bottom of the QTR fuselage approximately 3 feet from the ground and represents the condition at which the wheels underneath the vehicle just rest on the

ground.

The chord wise distributions of the non-dimensional pressure (C_{pDL}) are plotted at the same span wise locations as for the OGE case in Figure 5.7. C_{pDL} is again observed to be constant at the lower surface of the front wing. However, the magnitude is actually positive and much higher than when the vehicle was operating OGE, reducing the area inside the curve and as a result the downward force at each of these sections. Positive values of C_{pDL} on the lower surface suggests a higher than ambient pressure. This is a clear indication of more stagnated flow below the front wing surface. In addition the trailing edge flap region actually produces a small amount of upload. The pressure is no longer constant along the lower surface of the rear wing and increases slightly toward the trailing edge. The area inside the curves indicates a higher download for the rear wing at these sections than that for the front wing. The fact that the rear wing experiences a higher download than the front wing in most of the region underneath the rotor systems is clearly visible in the span wise loading distribution shown in Figure 5.8 for the QTR operating IGE. The front wing experiences a lower download per unit span everywhere when compared with the OGE download. The rear wing follows a different mechanism for download reduction. The inboard sections of the rear wing experience a strong upload balancing the download on the middle sections, which is not drastically reduced from the OGE condition. Hence, a significant download relief is experienced by both wings, which were seen to be the most significant sources of download for OGE operation.

Velocity vectors a little above the surface of the QTR are shown in Figure 5.9. The velocity vectors do not look much different from the OGE condition on the top surface except for the fuselage surface. A strong upward flow is observed grazing the fuselage surface. The bottom surface of the fuselage reveals a high pressure with flow predominantly in the longitudinal direction. There is also a reduction in span wise flow close to the wing tips when compared with OGE. The bottom surface of the front wing experiences a high pressure through out, where as the rear wing experiences high pressure at only the in-board locations on the lower surface. Velocity vectors at longitudinal planes (plane 1 and 2) through the front and rear

wing (Figure 5.10) reveal an upward flow impinging upon the bottom of the fuselage and inner sections of the wings when the vehicle operates IGE (especially the rear wing) and the flow is forced inwards at the ground plane. The right half of the figure depicts flow patterns OGE for comparison. These upward flow patterns underneath the QTR for IGE operation confirm the presence of an effective upward force on the fuselage. The fountain flow is also much stronger IGE at plane 2 than in OGE. This is a result of the flow blockage at the bottom surface IGE with the flow that escapes adopting different paths than when OGE. The effect of the ground plane is also to reduce the contraction of the rotor slip streams in the portion of the rotor flow outboard of the wing tips before they are turned outward.

5.2.2 In Ground Effect (10 feet off the ground)

The flight conditions with the wheels of the QTR on ground and far away were presented previously. The observed high download OGE transformed into a strong upload when the condition with the wheels of the QTR on ground was simulated. Better understanding of this drastic change in the loading pattern is desired and this change needs to be clearly explained. An intermediate condition in which the wheels of the QTR are 10 feet from the ground is simulated for hovering conditions. These simulations will provide an intermediate data point between the OGE and wheels on ground condition and hence will aid in a better understanding of the change in flow patterns and its ramification on the loading on the aircraft.

The QTR with wheels 10 feet off the ground is simulated using the current methodology attempting to accurately estimate the download on the aircraft. The near-body meshes employed for this condition are the same as those used to model hovering flight of QTR OGE and with wheels on the ground. The background mesh is modified such that the ground plane is moved further away, with respect to wheels on the ground condition, from the bottom of the aircraft body. This simulation also acts as a consistency check for the current methodology. The flow patterns observed in this condition will illuminate the download/upload producing mechanism for the current condition.

Similar to previous representations, C_{pDL} is plotted at three span wise locations, namely 0.3 R, 0.5 R and 0.7 R from the wing tip. The variation of C_{pDL} on the front and rear wing is shown in Figure 5.11. Similar to OGE and wheels on the ground condition, the pressure at the bottom surface is observed to be a constant, suggesting a large region of separated flow. Acceleration of flow across the leading edge leads to a steep drop in pressure or high negative values for C_{pDL}. Area inside the curve, or the download on the wing is observed to increase away from the tip. The increase in download can be partly explained by the location of maximum downwash for the isolated rotor. Since the maximum download for the isolated rotor occurs close to 0.7 R, the span wise location at 0.7 R from the wing tip experiences a high download. The span wise distribution of the loading is shown in Figure 5.12. Contrary to OGE, the rear wing experiences a higher download per unit span than the front wing. A large upload is observed at the inboard sections of the rear wing. This upload balances the download on the outer sections of the rear wing, similar to condition with wheels on the ground. The upload observed at the in-board sections is significant, but is considerably smaller than the wheels on the ground condition. The download on the middle sections of rear wing is comparable to the download observed at the middle sections of the rear wing for the wheels on the ground condition. The front wing experiences a higher download everywhere when compared to the wheels on the ground condition.

Velocity vectors at a small height above the surface of the QTR along with the C_{pDL} variation are shown in Figure 5.13. Strong span wise flow on the top surface of the QTR is evident close to the root of both front and rear wings. Flow is predominantly in the chord wise direction in the region where the flaps are present and separates at the bottom surface of the wing. High pressure is observed at the bottom surface of the fuselage and inner sections of the front and rear wing. The flow is fairly quiescent at the bottom surface of the fuselage. The direction of the flow is upward at the bottom surface suggesting the presence of an upward stream.

Velocity vectors at longitudinal planes through the front and rear wings are shown in Figure 5.14. The velocity vectors for the condition when the wheels of the aircraft are 10

feet off the ground are compared with the condition when the aircraft wheels are on ground. In both cases, the downward flow outside the wing tip is obstructed by the ground plane. This obstruction by the ground plane results in rotation of the flow to a horizontal plane. The downward stream is observed to bifurcate into two streams; one moving toward the center of the vehicle and the other moving outward away from the center of the vehicle. The stream moving toward the center of the vehicle starts to change direction as it approaches the symmetry plane. When the wheels of the aircraft are further away from the ground plane, the downward flow has a longer distance to suitably rotate from a vertical direction to a horizontal direction. This larger distance provides a larger space for the flow to slow down and turn and as a result would lead to a lower pressure at the bottom surface of the fuselage and inner sections of the wings. The flow below the wing is more quiescent for the wheels on the ground case when compared to the condition, where the wheels are 10 feet off the ground.

5.3 Integrated Loads

The integrated forces for the various surfaces are listed in Table 5.1 for OGE, wheels on ground and wheels 10 feet off the ground conditions along with differences between the IGE conditions with the OGE condition. The integrated loads are also plotted for these three conditions (OGE, Wheels 10 feet of the ground, Wheels on the ground) in Figure 5.15. The download on both wings (Front Wing, F.W. and Rear Wing, R.W.) for OGE operations transforms into an almost negligible load when the wheels are placed on the ground, where as the negligible load on the fuselage (fslg.) in OGE operations transforms into a strong upload. Intermediate loads are observed for the condition where wheels are 10 feet of the ground. The overall lifting capability of the QTR when operating IGE is drastically improved, because of the changes in loading on the three components of the QTR. It can be noted that the fuselage accounts for 50% of the difference in loads (between OGE and wheels on the ground condition), while the wings each contribute approximately 25% each. This increase in overall

Table 5.1: Loads as percentage of thrust on the QTR components in hover at various heights above the ground

Condition	F. W.	R. W.	Fslg.	Total
OGE	-5.3	-3.7	-0.1	-9.1
Wheels 10 feet off ground	-2.7	-1.5	6.3	2.1
Wheels on ground	-0.7	0.6	8.9	8.8
Difference (OGE - 10 feet)	2.6	2.2	6.4	11.2
Difference (OGE - ground)	4.6	4.3	9.0	17.9

vehicle lifting capability when operating IGE can translate into a large increase in payload capability of the aircraft, if it is seen to persist at higher forward speeds. Even for the wheels 10 feet off the ground, there is a drastic increase in the payload carrying capability of the QTR, because of the benefits of operating in the ground cushion.

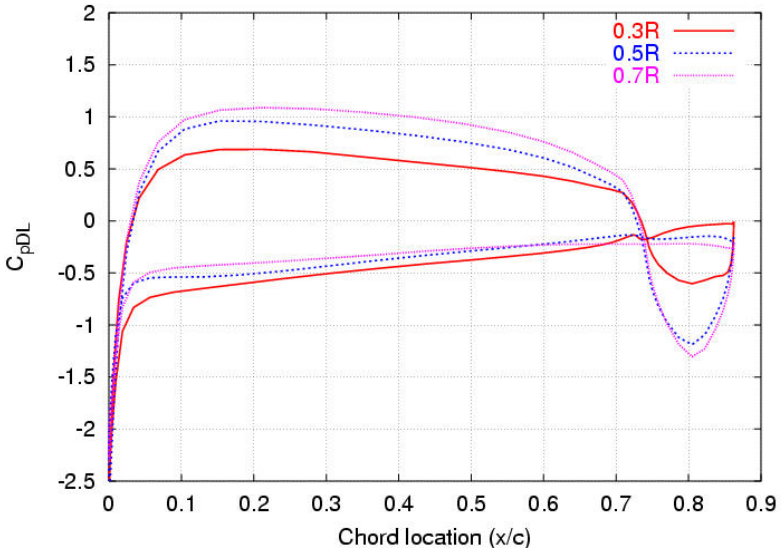

(a) Front Wing

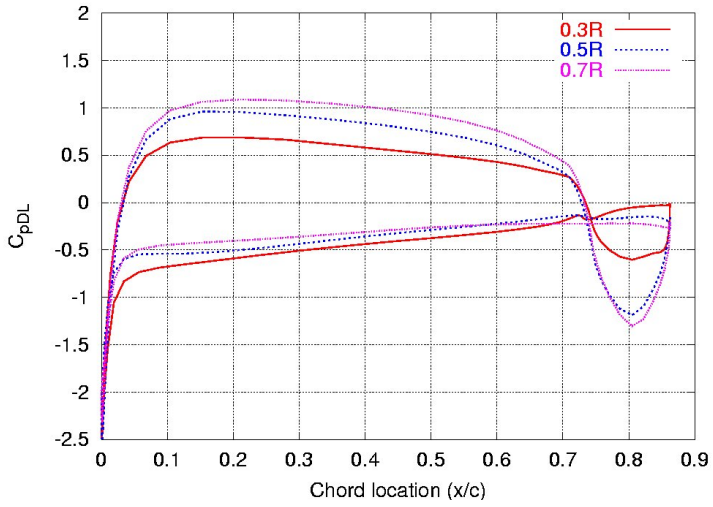

(b) Rear Wing

Figure 5.2: Chord wise pressure distribution at various locations on the wings in hover (OGE).

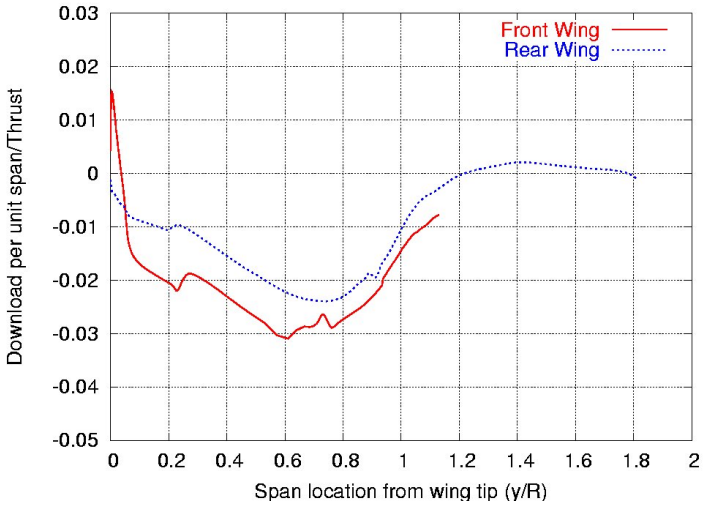

Figure 5.3: Span wise download per unit span distribution on the wings in hover (OGE).

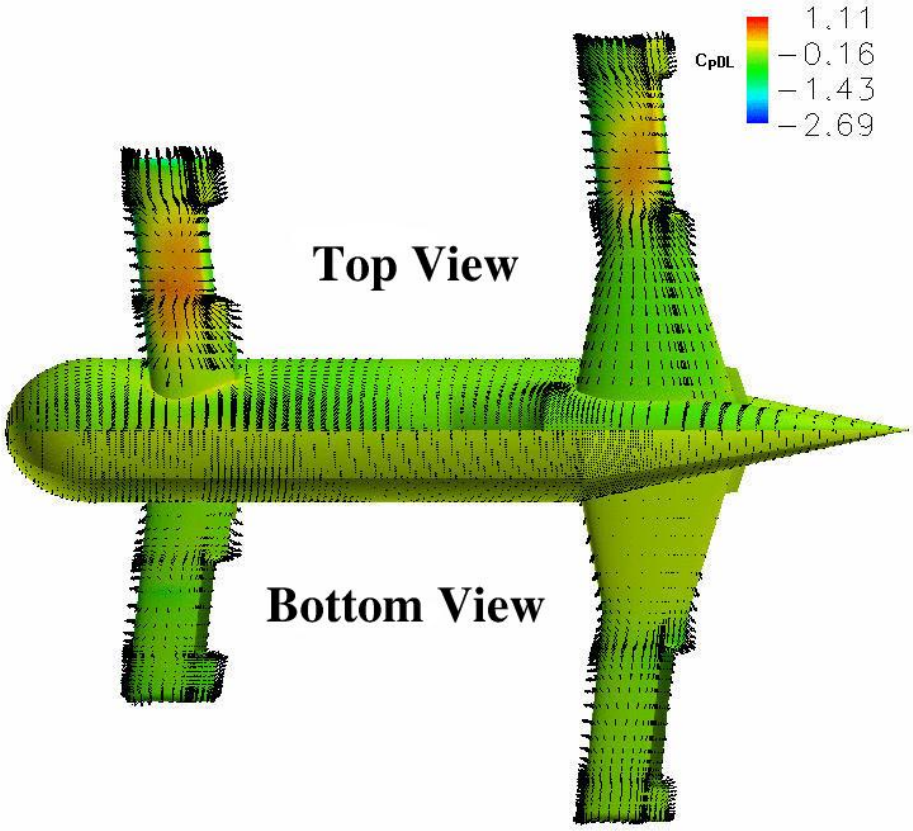

Figure 5.4: Velocity at a small height above the surface along with C_{pDL} distribution in hover (OGE).

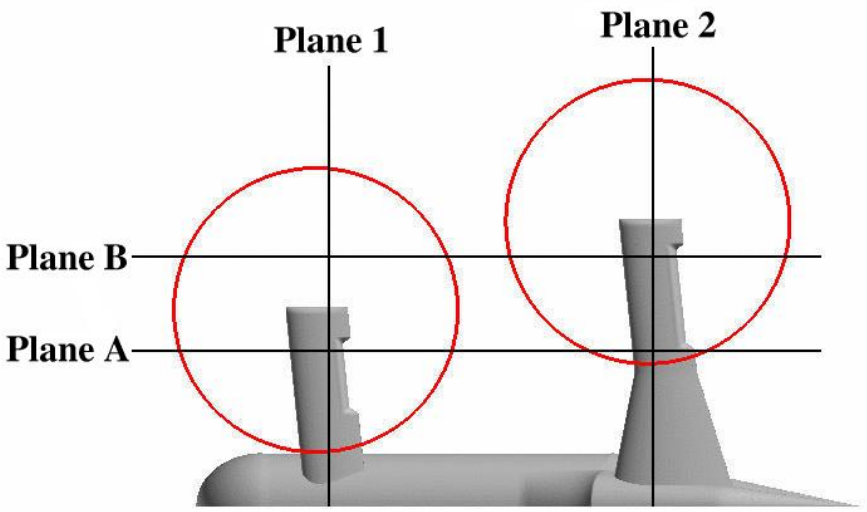

Figure 5.5: Location of various planes used for flow description.

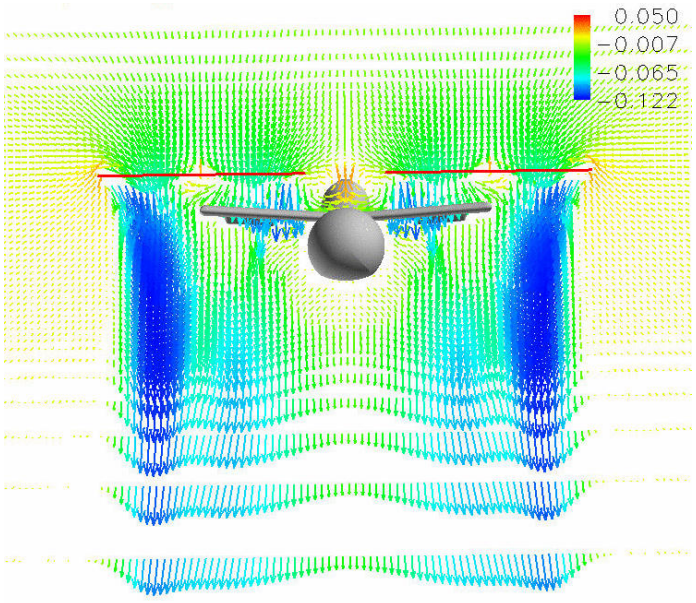

(a) Front Wing

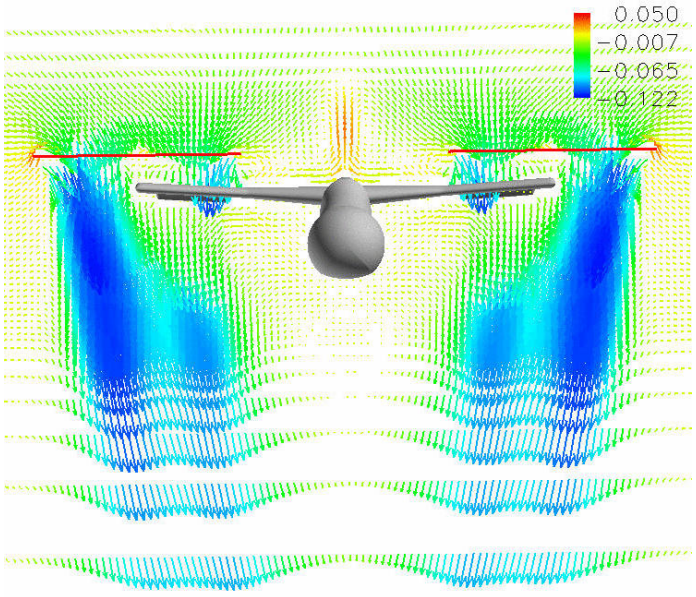

(b) Rear Wing

Figure 5.6: Velocity vectors at vertical longitudinal planes (1 and 2) through the front and rear wing; colors depicting vertical velocity (hover OGE).

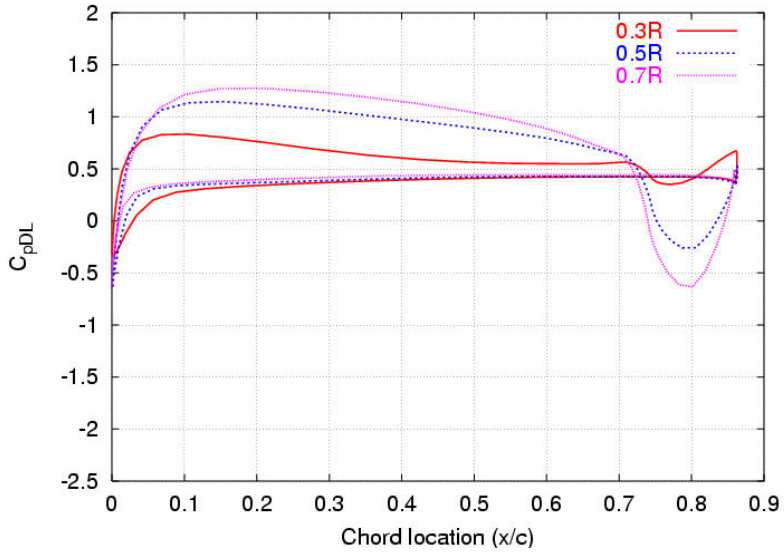

(a) Front Wing

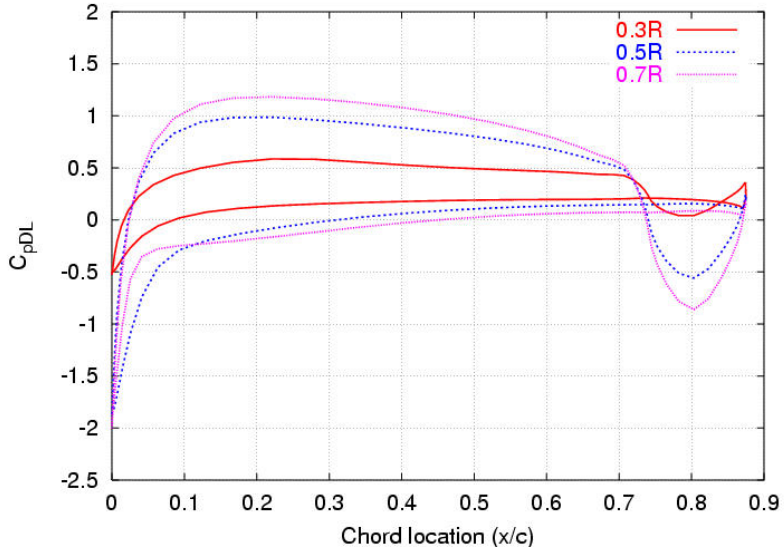

(b) Rear Wing

Figure 5.7: Chord wise pressure distribution at various locations on the wings in hover (wheels on ground).

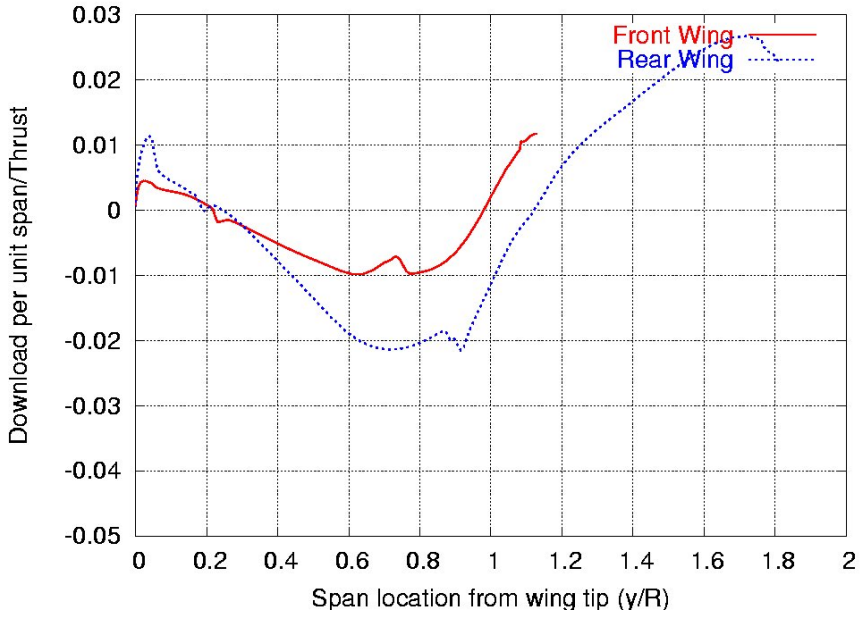

Figure 5.8: Span wise download per unit span distribution on the wings in hover (wheels on ground).

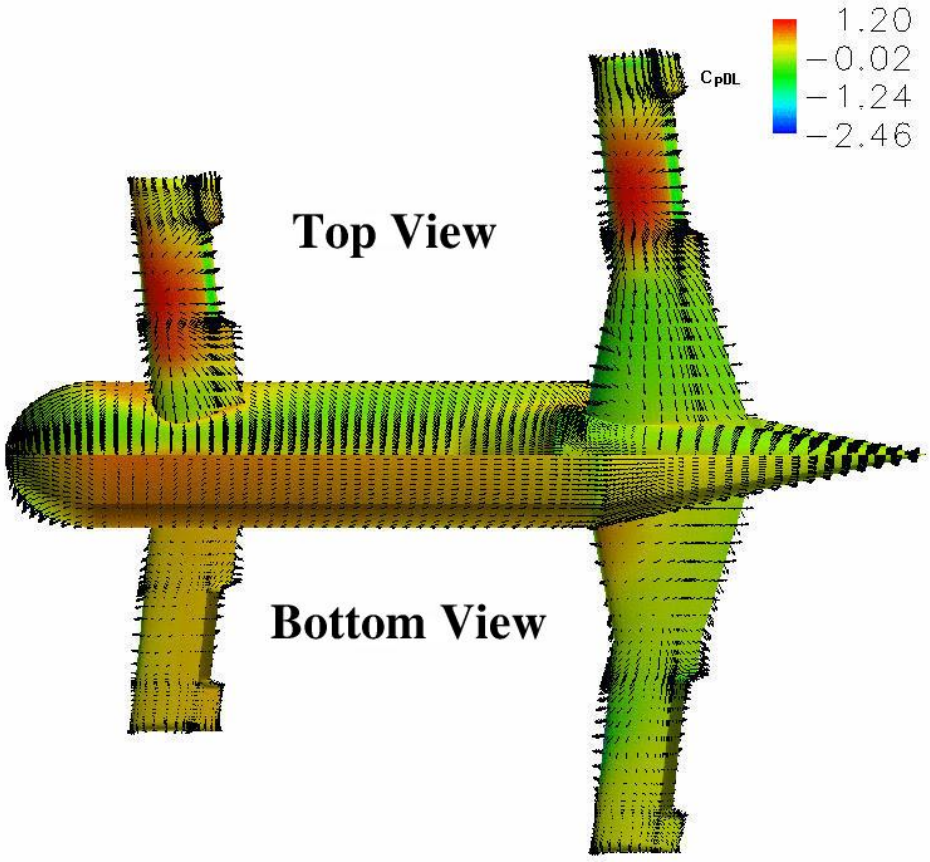

Figure 5.9: Velocity at a small height above the surface along with C_{pDL} distribution in hover (wheels on ground).

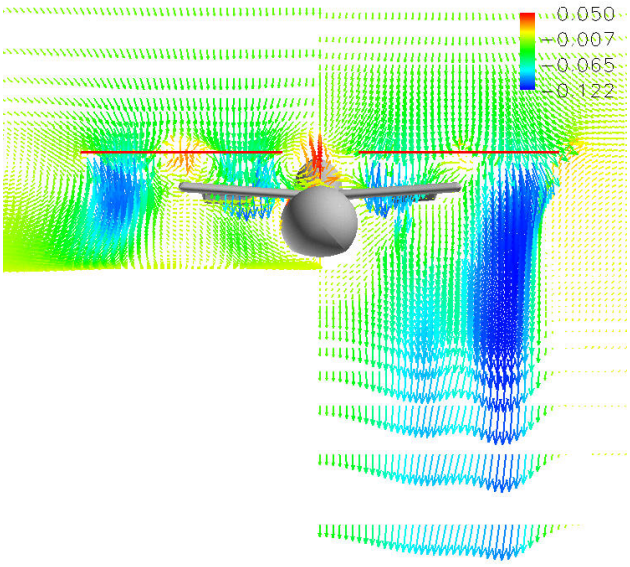

(a) Front Wing

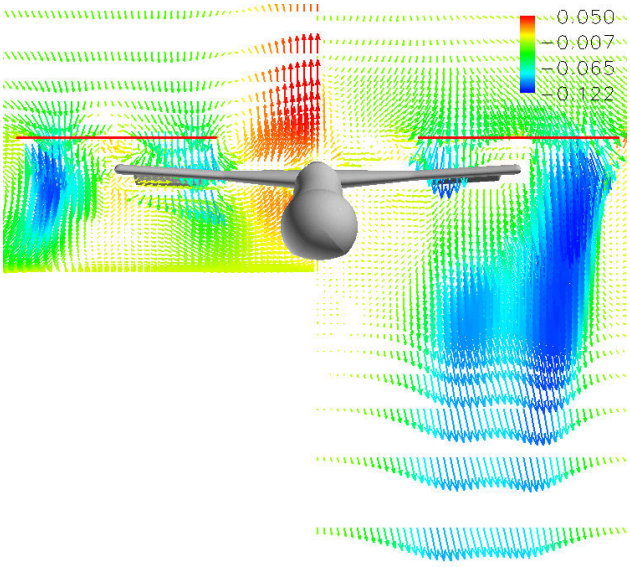

(b) Rear Wing

Figure 5.10: Velocity vectors at vertical longitudinal planes (1 and 2) through the front and rear wing (Left - Wheels on ground, Right - OGE; hover).

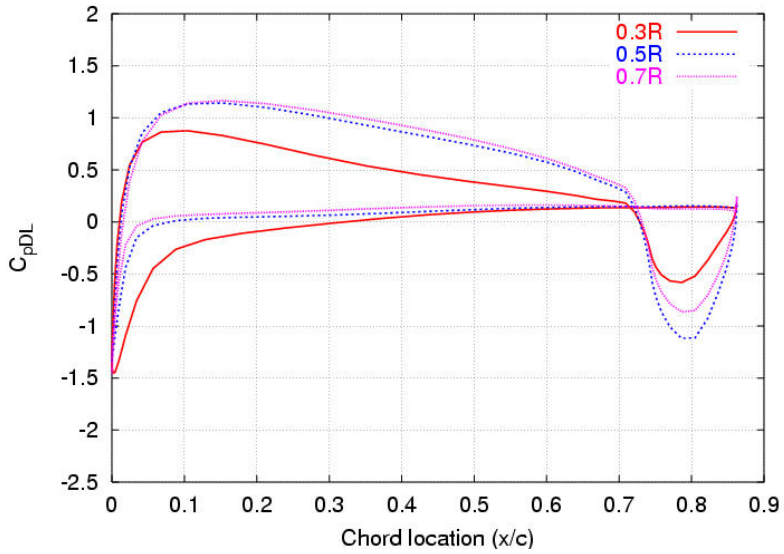

(a) Front Wing

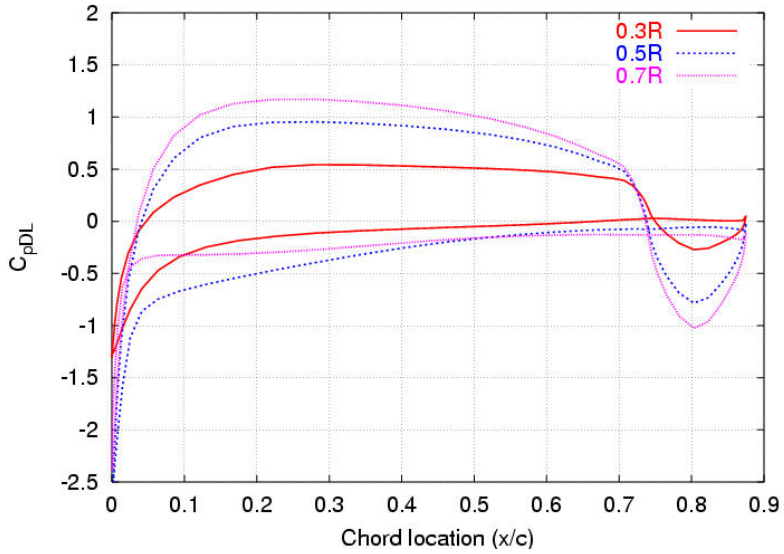

(b) Rear Wing

Figure 5.11: Chord wise pressure distribution at three span wise locations in hover (wheels 10 feet off the ground).

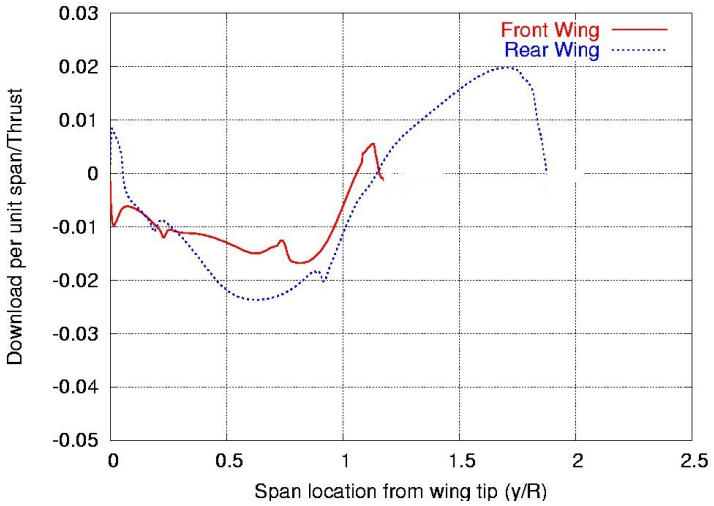

Figure 5.12: Span wise distribution of download on the wings from the wing tip in hover (wheels 10 feet off the ground).

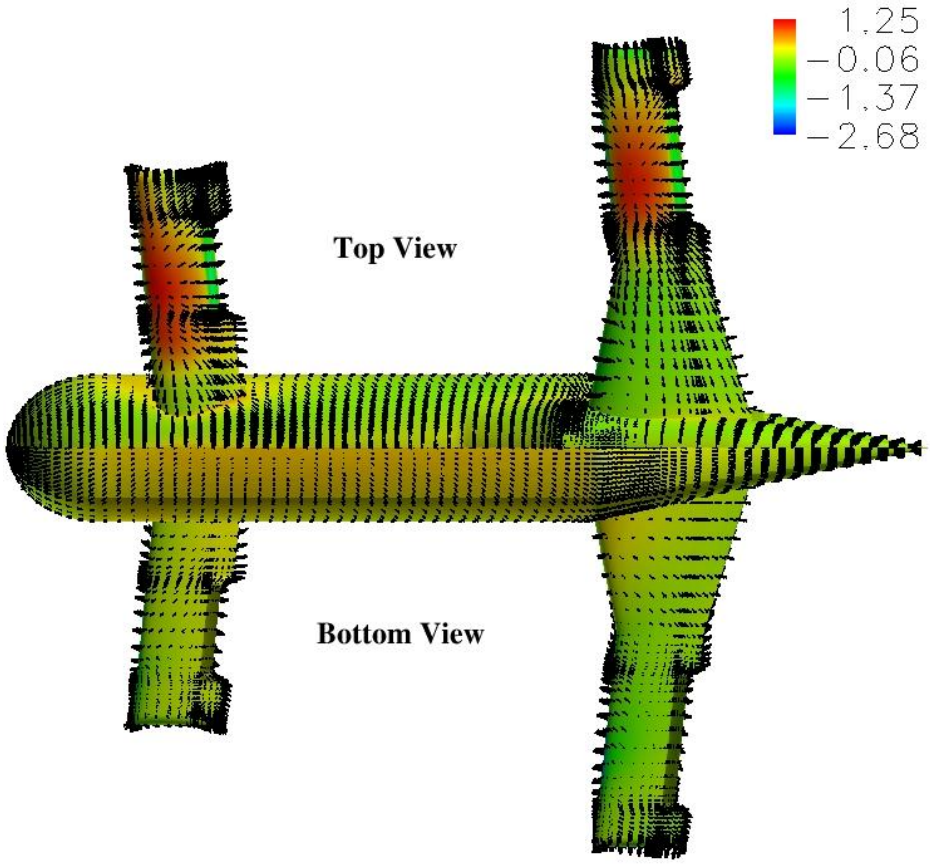

Figure 5.13: Velocity vectors at a small height above the surface along with C_{pDL} distribution (wheels 10 feet off the ground; in hover).

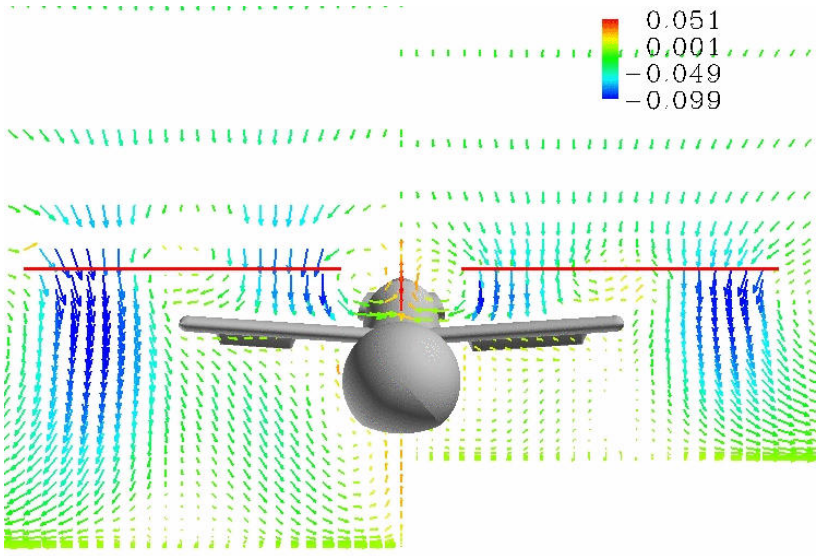

(a) Front Wing

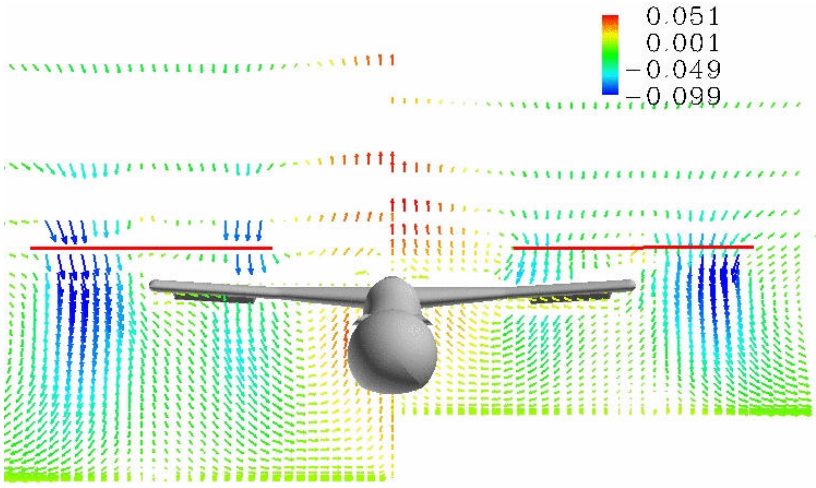

(b) Rear Wing

Figure 5.14: Velocity vectors at vertical longitudinal planes (1 and 2) through the front and rear wing (Left - 10 feet off the ground, Right - on ground).

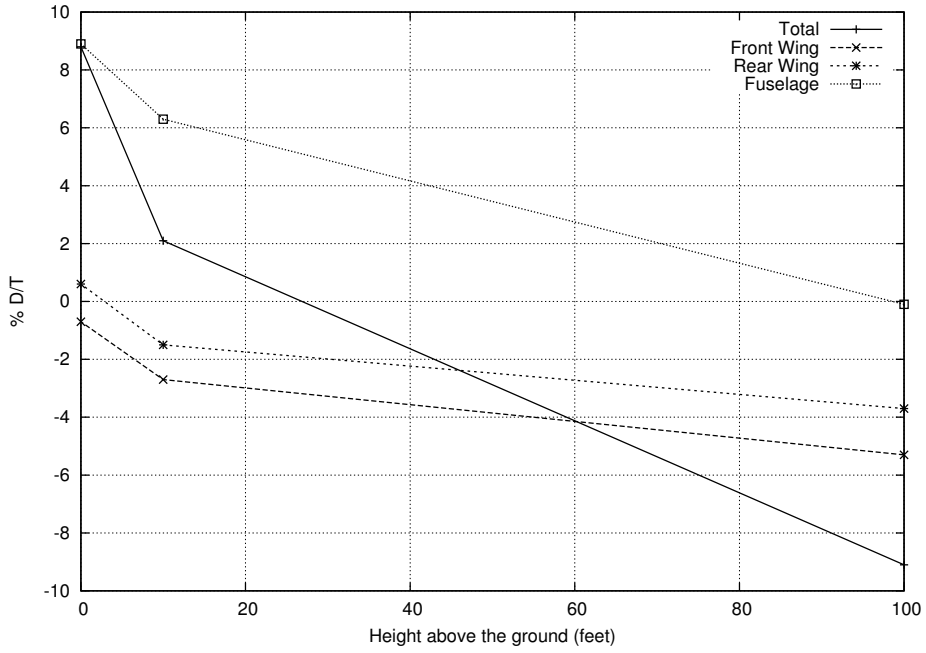

Figure 5.15: Integrated loads on the QTR as a percentage of total thrust at various heights above the ground.

Chapter 6

Slow Forward Flight of the Quad Tilt Rotor

Hovering flight for OGE and IGE was presented in the previous chapter. High download experienced OGE transformed into a strong upload IGE for hovering flight. Various forward speeds are simulated for OGE and IGE operation to investigate whether the differences in loading for hovering flight will magnify or diminish as the QTR moves forward. Flow field patterns are compared for these conditions. These flow patterns directly affect the loading distribution on various components of the QTR. These modifications in loading patterns are of great significance and there is a need to quantify the loads as a function of forward speed.

The rotor induced velocity is not only the most important parameter of the rotor, but also dictates the download experienced by the wings. Hence, the forward speeds are non-dimensionalized by the induced velocity of the rotor and expressed as an angle by which the flow through the rotor plane would be skewed. The skewness of the flow governs the angle at which the rotor downwash impinges on the wing below it and directly affects the download experienced by the wing. The skew angle can be written as:

$$\chi = atan(\frac{V_\infty}{V_{ind}}) \tag{6.1}$$

where V_∞ is the forward speed or free stream velocity and V_{ind} is the rotor induced velocity. Schematic views of the rotor wake with the airfoil are shown in Figure 6.1 for hovering flight and forward flight at a 45 degree skew angle.

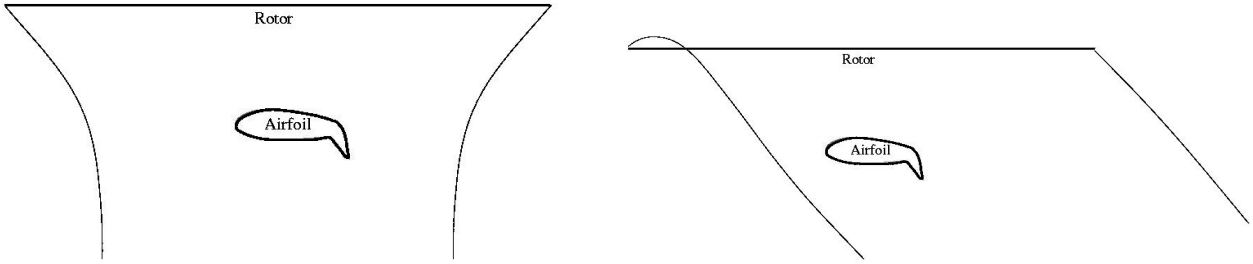

(a) Hovering Flight

(b) Skew Angle 45 degrees

Figure 6.1: Schematic view of the rotor wake interaction with the wing airfoil

.

6.1 Out of Ground Effect (OGE)

In forward flight, the downwash from the rotor starts to skew backward as the aircraft moves faster. The skewing of the downwash reduces the angle at which the flow impinges the top surface of the wings and as a result the pressure on the top surface reduces. Even at high forward speeds, the rotor downwash will not miss the wing. Flow patterns on the QTR are more complicated than those for the traditional tilt rotor because of the presence of the rear wing. The skewed downwash from the front rotor might interfere with the rear wing and lead to an increase in download on the rear wing. All of these issues will be explored in this section for the various CFD simulations.

The chord wise distribution of C_{pDL} is shown in Figure 6.2 at 0.5 R from the tip for both the front and rear wings. The pressure on the top surface of the rear wing is observed to increase as the speed or skew angle increases. The pressure on the top surface of the front wing increases initially and then starts to decrease with forward speed. Furthermore, the skew angle causes peaks in C_{pDL} to be more skewed toward the leading edge for both wings. A small pocket close to the leading edge causing an upward force for the rear wing at skew angle of 1 degree seems to disappear as the skew angle increases. Skewing of the flow is equivalent to modifying the angle of attack of the wing. Since this pocket producing upward force was missing for the front wing in hover, which is at an angle of 3 degrees relative to the

fuselage, this partially explains the disappearance of this upward force producing pocket as the flight speed increases. The pressure at the lower surface of the rear wing is drastically reduced for the highest skew angle. This is because of the interference of the downwash from the two rotors which increases the dynamic pressure below the rear wing with a consequence of reducing the static pressure. Little change in the pressure at the lower surface of the front wing is visible as the vehicle flight speed increases. The chord wise pressure plots also reveal that the trailing-edge flaps become even more effective with an increase in forward flight speed, as would be expected.

Span wise distribution of load on the front and rear wings is shown in Figure 6.3. The angle of attack of 3 degrees for the front wing relative to the fuselage results in generation of lift and this effect is clearly evident at the inner sections which do not experience any rotor downwash. As a consequence the download at the inner sections reduces, as the aircraft travels faster and the inmost portion eventually becomes lifting. There are marked differences in the span wise download distribution at the outer sections for the rear wing with forward speed, especially for the highest advance ratio case. The download on the rear wing is observed to increase as the aircraft propels forward. This effect is predominantly because of the increased influence from the downwash of the front rotor. Undulations in the distribution are observed at the ends of the flaps on both wings.

Velocity vectors at plane A and plane B, which are parallel to the symmetry plane (the position of both planes are shown in Figure 5.5), are shown in Figures 6.4 and 6.5, respectively. Plane A intersects the front wing and the front rotor, but a very small portion of the rear rotor, whereas plane B intersects the same location on the rear wing as the plane A on the front wing. It should be noted that plane B does not intersect with the front wing, hence the influence of the front wing on the rotor downwash will not be seen in this plane.

For clarity only three skew angles, namely 1 degree, 18 degrees and 43 degrees are shown in the figures. Skewing of the flow is clearly evident in these figures. In all cases the skewing of the flow is not yet large enough to completely miss the front wing. However, the download on the front wing is reduced because of the reduced angle at which the flow impinges on

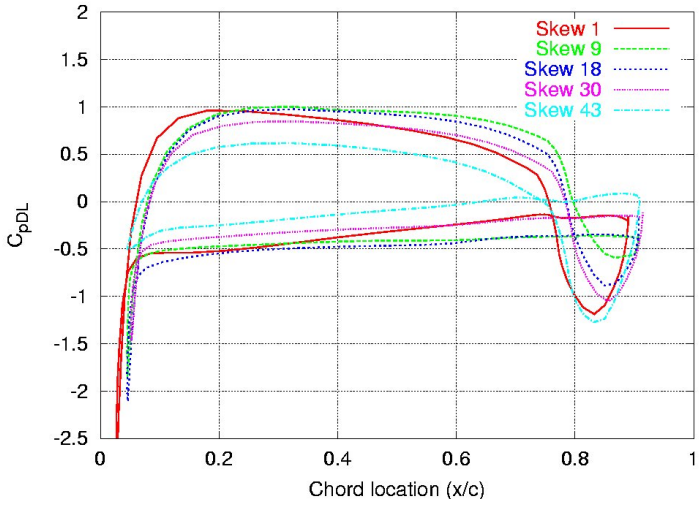

(a) Front Wing

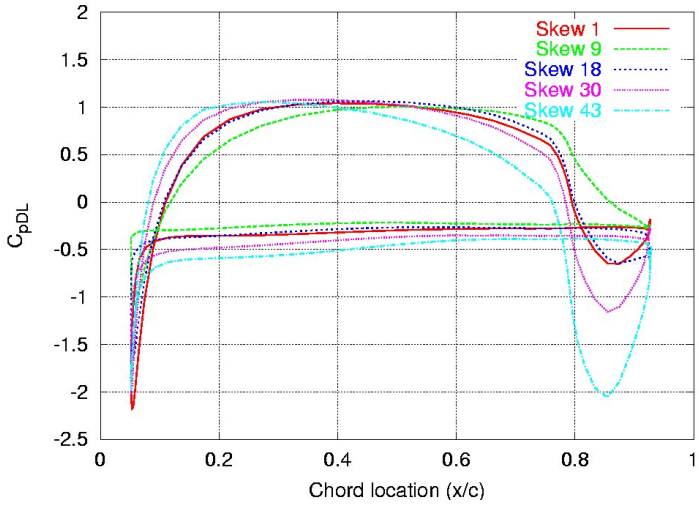

(b) Rear Wing

Figure 6.2: C_{pDL} distribution along the chord at 0.5 R from the wing tip for various skew angles (OGE)

.

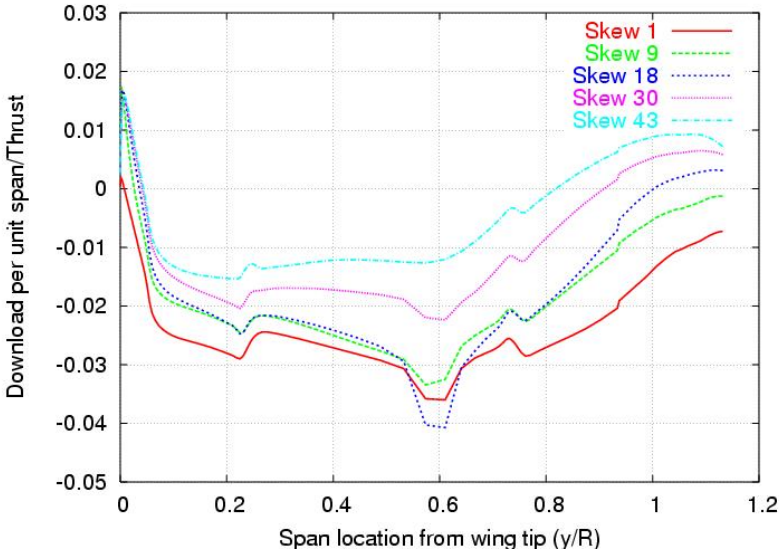

(a) Front Wing

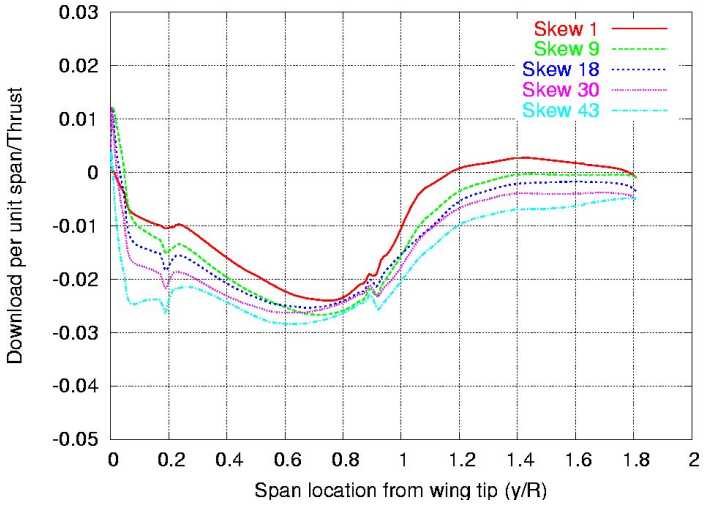

(b) Rear Wing

Figure 6.3: Span wise distribution of loads on front and rear wing in forward flight (OGE).

the front wing. The two streams emerging from the two rotor systems attract each other as they move downward. This attraction of the streams modifies the downwash incidence toward the rear wing (clearly visible for the case of a skew angle of 1 degree). It can be noted

that negative loading on the wing is equivalent to introducing an anti clockwise circulation in the flow around the wing. Evidence of this circulation is observed in all the figures at appropriate locations. At the highest skew angle (43 degrees) it becomes quite clear that the effective skew angle of the rear rotor system is less than for the front rotor system, due to the influence of the front rotor system on the rear rotor system. The highest downwash velocities are obtained below the rear portion of the front rotor system and below the front portion of the rear rotor system. The upwash region between the front and rear rotor systems is no longer visible. Furthermore, the higher flow velocity underneath the rear wing for the highest skew angle case leads to a reduction in pressure at the bottom surface and as a consequence, a high download on the rear wing is obtained for this condition.

The integrated loads on the QTR components for the various skew angles are listed in Table 6.1. The integrated loads experienced by the wings and fuselage are plotted as function of skew angle in Figure 6.6. The download on the front wing reduces rapidly with forward speed beyond 13 knots ($\mu = 0.03$), where as the increasing download trend on the rear wing continues throughout the range of forward speeds. The download reduction pattern on the front wing is very similar to that for the V-22 wing obtained in wind tunnel tests [17]. The fuselage experiences a negligible download at low speeds, but begins to generate some lift at faster speeds. The resulting total download trend is such that the download actually initially increases with forward flight speed reaching a maximum for a skew angle of around 9 degrees (equivalent to a forward flight speed of approximately 6 knots). Further increase in translational velocity results in a steep decrease in the amount of total vehicle download.

6.2 Wheels on Ground

The flow field features become even more complicated with forward speed when the vehicle operates with wheels on the ground. The downward flow that was fenced by the downwash from the four rotor systems was observed to impinge upon the ground plane and transform into an upward flow close to the middle of the aircraft in hover. This upward flow below the

Table 6.1: Loads as percentage of thrust on the QTR components in forward flight (OGE).

Skew Angle (μ)	Speed(Knots)	F. W.	R. W.	Fslg.	Total
1^o (0.0015)	0.66	-5.1	-3.7	-0.1	-8.9
5^o (0.0075)	3.32	-4.6	-4.5	-0.3	-9.4
9^o (0.015)	6.64	-4.8	-4.8	-0.1	-9.7
18^o (0.03)	13.28	-4.6	-5.4	0.6	-9.3
30^o (0.0525)	23.25	-2.6	-5.8	1.1	-7.3
43^o (0.075)	33.21	-1.6	-6.2	1.5	-6.3
64^o (0.1683)	80	2.0	-4.1	2.0	-0.1

fuselage and the wing caused an upload on the QTR in hover. This stagnated/upward flow should be expected to wash backward with forward speed and reduce the strong upload on the fuselage with increasing forward speed. The effect of forward speed on the loads on the QTR along with modification of upload producing mechanism is outlined in this section.

C_{pDL} distribution at 0.5 R from the wing tip is shown in Figure 6.7 for both wings. The flap is again observed to produce an upward force at this section for both wings and the flap becomes more effective at higher speeds. The pressure at the bottom surface of the front wing is again constant, suggesting separated flow. The pressure at the bottom surface of the rear wing is skewed and increases toward the trailing edge. The low pressure at the bottom surface close to the leading edge represents high speed flow around the leading edge because of the presence of the wake of the front rotor interfering with the rear wing. The wake of the front rotor is at a very shallow skew angle and it increases the speed of the flow at the bottom surface of the rear wing. Area inside the curves is much smaller than the area inside the curves for OGE operation. Pressure at the bottom surface of the front and rear wings decreases drastically for the maximum forward velocity condition. The span wise distribution of loading on the wings is shown in Figure 6.8. The magnitude of the load per unit span for the front wing is very small when compared to the rear wing. This observation can be directly correlated with the distance of the wings from the ground. The proximity

of the front wing to the ground leads to a more stagnated flow below the front wing. The rear wing experiences an upward flow at the inboard locations, since the rear wing is higher and the rear set of rotors are further apart and significant upwash is developed toward the root of the wing and the fuselage for all cases in ground effect. Overall the effect of forward velocity on the span wise loading distribution on the wings is small, especially for the rear wing.

Loading on the fuselage is of significant importance in this flight operation (IGE). Longitudinal loading along the fuselage at various forward speeds is shown in Figure 6.9. The upload experienced by the fuselage is seen to fade away with increasing forward speed. The curve moves downward without a marked change in the shape except for higher forward speeds. The initial peak upload on the fuselage in the region in front of the front wing is drastically reduced for the highest skew angles. The reason for this is seen in the plot of velocity vectors at a plane 2 feet above the ground plane, shown in Figure 6.10. Only three skew angles, namely 1 degree, 18 degrees and 43 degrees, are shown in the figure. The color of the velocity vectors reveals the magnitude of the upward/downward velocity (negative, or blue, being downward). The downward flow from the rotor systems impinge on the ground plane and splay in all directions, especially for the skew angle of 1 degree. As the aircraft moves faster the splaying in the upwind direction in front of the vehicle is reduced. Also, the blue vectors (depicting downward flow) move backward as the aircraft moves faster, demonstrating a gradual washing away of the stagnated flow below the fuselage. Eventually, the velocity of the aircraft becomes large enough that the flow underneath the front of the rotors cannot splay forward, but rather is also swept backward forming an almost horseshoe shaped vortex system. For the QTR aircraft with its wheels on the ground this occurs for a skew angle between 18 and 30 degrees, resulting in the loss of some of the upload on the front portion of the fuselage seen in Figure 6.9.

Velocity vectors are also shown at planes A and B in Figures 6.11 and 6.12, respectively. The presence of the ground plane forces the flow to move parallel to the ground close to the ground. Also, a smaller circulation is observed around the wings, since the wings are

less loaded in this condition when compared with OGE operation. Skewing of the flow is clearly evident in the figures, with the flow through the rear rotor skewing less than the front rotor, because the shielding of the rear rotor by the front rotor from the effect of free stream velocity. An upwash is observed in front of the leading edge of the front rotor for the highest forward velocity condition, but this upwash region is missing for the rear rotor. This is because the flow has already been partly turned in the vertical direction by the front rotor, reducing the effective skew angle for the rear wing. A high speed stream in a backward direction is observed close to the ground plane for all the three cases shown. This high speed stream is the fastest for the highest velocity condition because, the forward speed of the QTR pushes all the flow entrained by the rotors backward.

The integrated loads on various components of the QTR in slow forward flight operating IGE are listed in Table 6.2 for the given skew angles. The integrated loads are also pltted as function of skew angle in Figure 6.13. There is a continuous drop in the upload experienced by the fuselage. The front wing initially experiences an increase in download with forward speed, but it begins to reduce once the inboard portion of the wing starts to produce lift. The rear wing experiences an increase in downward force with forward speed, similar to that observed for OGE operations. Hence, the overall upload on the QTR is observed to reduce with increasing forward speed.

6.3 Wheels 10 feet off the ground

The maximum skew angle condition is simulated for the QTR with wheels 10 feet off the ground. This condition elucidates the variation of flow patterns and loading on various components of the QTR. This condition marks the transition to propeller mode of flight for the QTR and hence it is very essential to quantify the loading at this condition to understand the differences in flow patterns at the other extreme of the helicopter mode of the QTR.

Non dimensional pressure is plotted at three locations (0.3 R, 0.5 R and 0.7 R from the wing tip) on both front and rear wings and are shown in Figure 6.14. Similar to OGE and

Table 6.2: Loads as percentage of thrust on the QTR components in forward flight (wheels on ground).

Skew Angle (μ)	Speed (Knots)	F. W.	R. W.	Fslg.	Total
1^o (0.0015)	0.6642	-1.2	0.3	8.4	7.5
5^o (0.0075)	3.321	-1.7	0.1	7.8	6.2
9^o (0.015)	6.64	-1.9	0.2	7.5	5.8
18^o (0.03)	13.28	-2.0	0.1	7.1	5.2
30^o (0.0525)	23.25	-1.8	-0.8	6.5	3.9
43^o (0.075)	33.21	-1.0	-1.2	5.6	3.4
64^o (0.1683)	80	3.0	-2.2	5.2	6.0

wheels on ground condition, the flap is observed to produce an upward force in this condition, too. The upward force at the rear half of the wing almost balances the downward force at the front half of the wing for the front wing. The downward force is larger for the rear wing at these sections. This suggests an interaction between the front rotor wake and the rear wing leading to an increased download on the rear wing as compared to the front wing.

Span wise distribution of loads on the wings for this flight condition are plotted in Figure 6.15. The rear wing again experiences a larger download per unit span in the region below the rotor. However, the in-board sections of the rear wing produce a large upload which balances the download at the out-board sections. Velocity vectors a little above the QTR surface along with pressure variation are shown in Figure 6.16. Very small region of separated flow is observed at the leading edge of the front wing, where as there is remarkable separation at the leading edge of the rear wing. This observation again concludes the shielding effect of the rear rotor by the front rotor from the backward free stream velocity. It is equivalent to simulating the rear wing and rear rotor combination at a smaller skew angle.

Velocity vectors at plane A and plane B are shown for the maximum forward speed for the wheels of the aircraft 10 feet away from the ground in Figure 6.17. Turning of flow around the leading edge of the rotor is clearly visible for the front rotor, but is missing for the rear

rotor. Direction of flow below the fuselage is predominantly backward. The velocity vectors are colored by the downward velocity at those points. It can be noted from velocity vectors at plane B, that the downwash of the front rotor does not directly impinge on the rear wing, but still has an indirect effect on the loading on the rear wing. The shielding of the rear rotor from the free stream velocity by the front rotor reduces the effective skew angle of the rear rotor. This reduction in skew angle increases the download on the rear wing.

The fuselage experiences a significant upload IGE operation for the QTR. The distribution of the upload on the fuselage is of great importance and is plotted in Figure 6.18 for the hover and forward flight cases. The loading on the fuselage is almost constant between the trailing edge of the front wing and leading edge of the rear wing for the hovering condition. There are two distinct peaks for the maximum forward speed condition. First peak is observed a little ahead of the front wing and the second occurs between the front and rear wings. The peak ahead of the front wing suggests stagnation of flow, caused by cancellation of the rotor downwash splaying in the upstream direction by the free stream velocity. The peak between the two wings is caused by the cancellation of the splaying of the rear rotor downwash with the front rotor downwash. This stagnation in the horizontal plane pushes the flow in the upward direction leading to an upload on the fuselage.

The integrated loads for the highest skew angle (43^o) are compared for OGE, wheels of the QTR on ground and wheels of the QTR 10 feet off the ground in Table 6.3. The integrated loads are also plotted in Figure 6.19. Even at the highest skew angle, there are substantial differences in the download on the QTR among the three conditions. As opposed to hovering conditions where the download reduction occurred mainly on the fuselage, the download reduction on the QTR is mainly on the rear wing for the highest skew angle. The high download on the rear wing for this skew angle OGE operation is modified to a small download for the condition where wheels of the QTR are 10 feet off the ground and even smaller download for the wheels on ground condition. The download on the front wing is almost equal for the two conditions, since the skewing of flow causes the download to fade away from the front wing. There is an increased upload on the fuselage IGE when compared

Table 6.3: Loads comparison at the highest skew angle (43^o) for OGE and IGE.

Condition	F. W.	R. W.	Fslg.	Total
OGE	-1.6	-6.2	1.5	-6.3
Wheels 10 feet off ground	-1.1	-3.1	3.5	-0.7
Wheels on ground	-1.0	-1.2	5.6	3.4
Difference (OGE - 10 feet)	0.5	3.1	2.0	5.6
Difference (OGE - ground)	0.6	5.0	4.1	9.7

to OGE operation. The upload is observed to reduce with height.

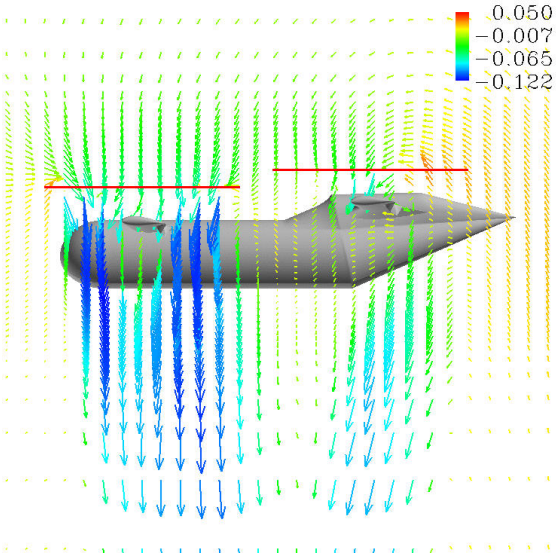

(a) Skew Angle 1^o

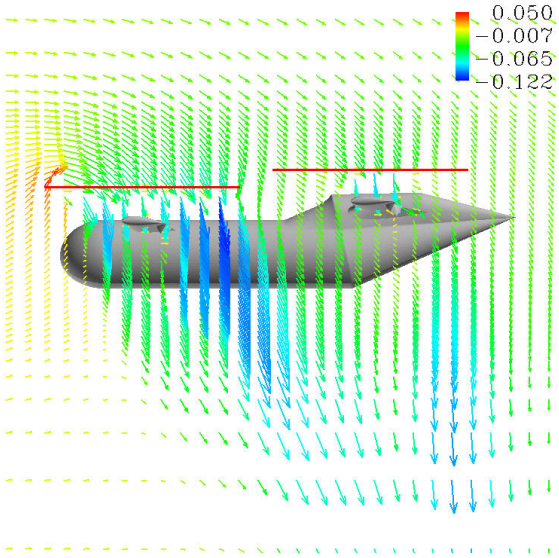

(b) Skew Angle 18^o

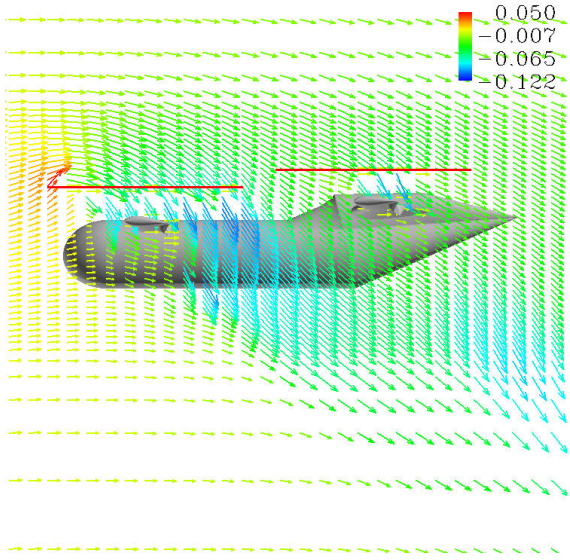

(c) Skew Angle 43^o

Figure 6.4: Velocity vectors at plane A parallel to symmetry plane in forward flight (OGE).

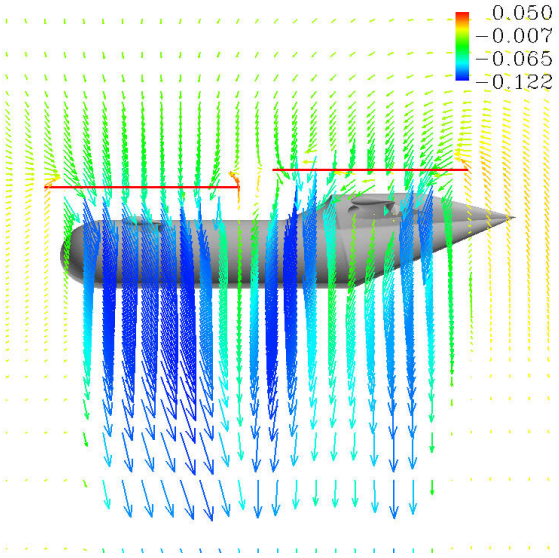

(a) Skew Angle 1^o

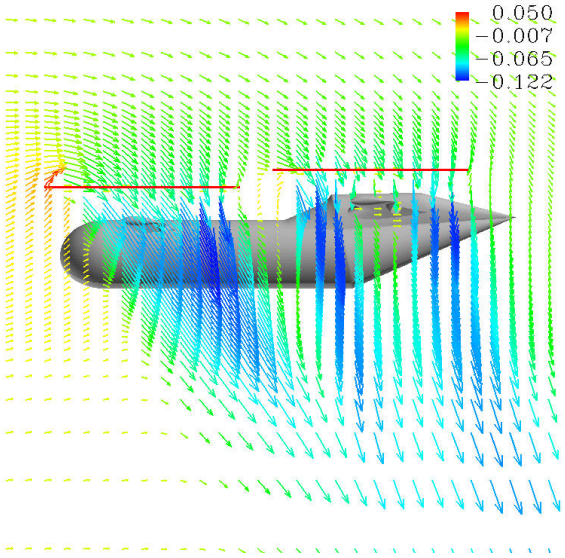

(b) Skew Angle 18^o

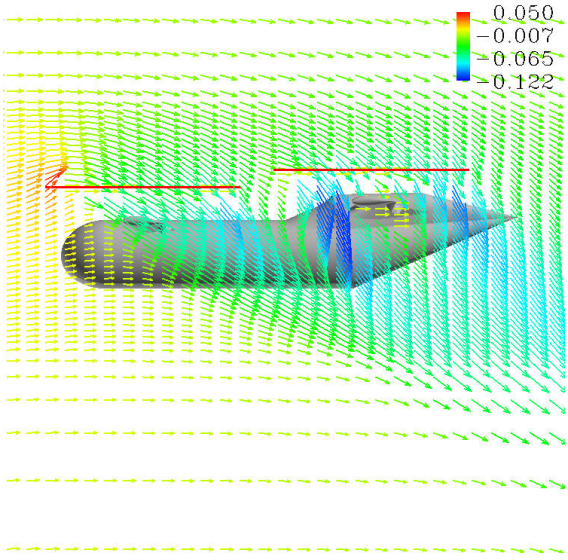

(c) Skew Angle 43^o

Figure 6.5: Velocity vectors at plane B parallel to symmetry plane in forward flight (OGE).

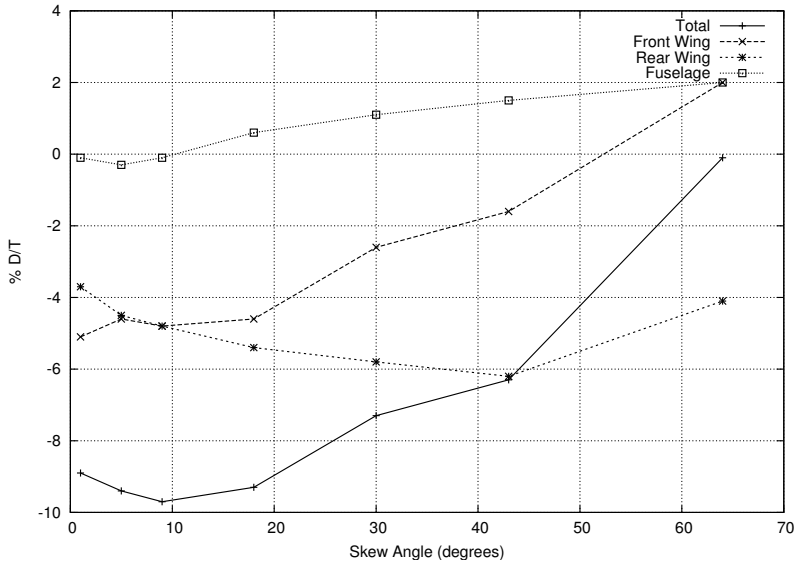

Figure 6.6: Integrated loading on the QTR (OGE) as a percentage of the total thrust at various skew angles.

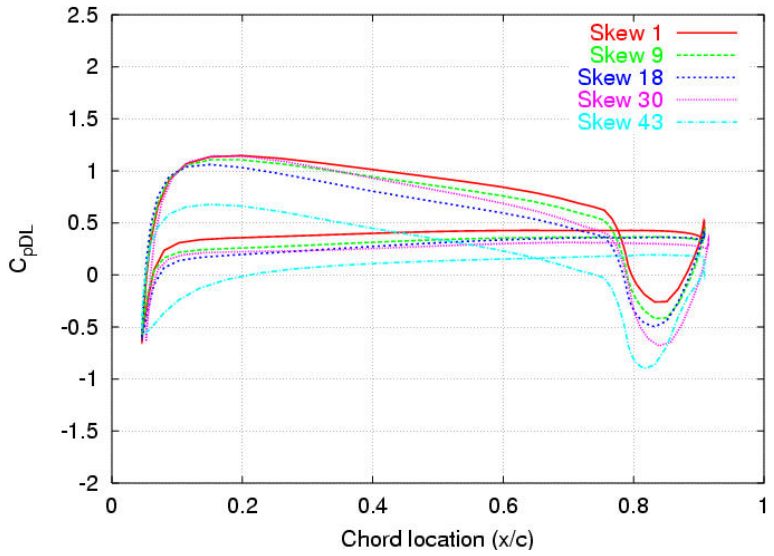

(a) Front Wing

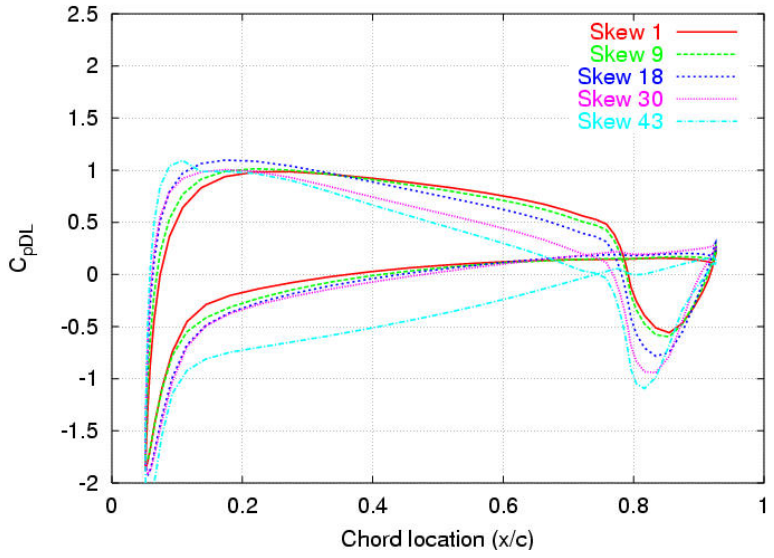

(b) Rear Wing

Figure 6.7: C_{pDL} distribution along the chord at 0.5 R from the wing tip for various skew angles (wheels on ground)

.

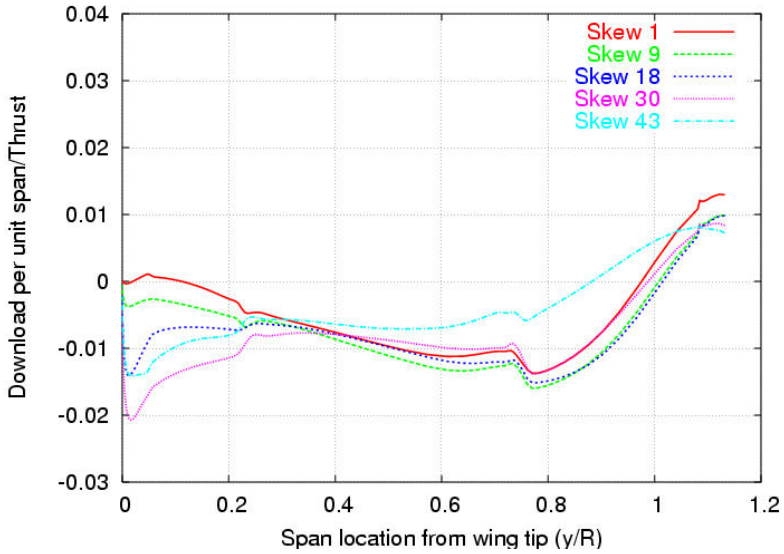

(a) Front Wing

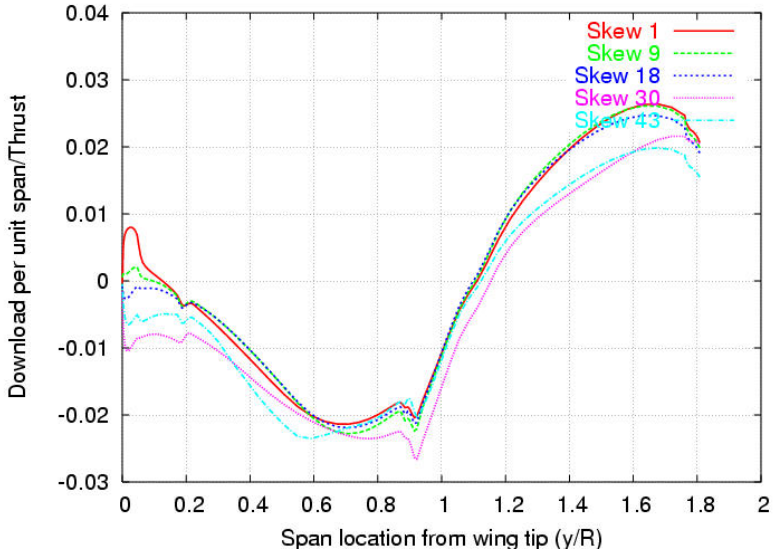

(b) Rear Wing

Figure 6.8: Span wise distribution of loads on front and rear wing in forward flight (wheels on ground).

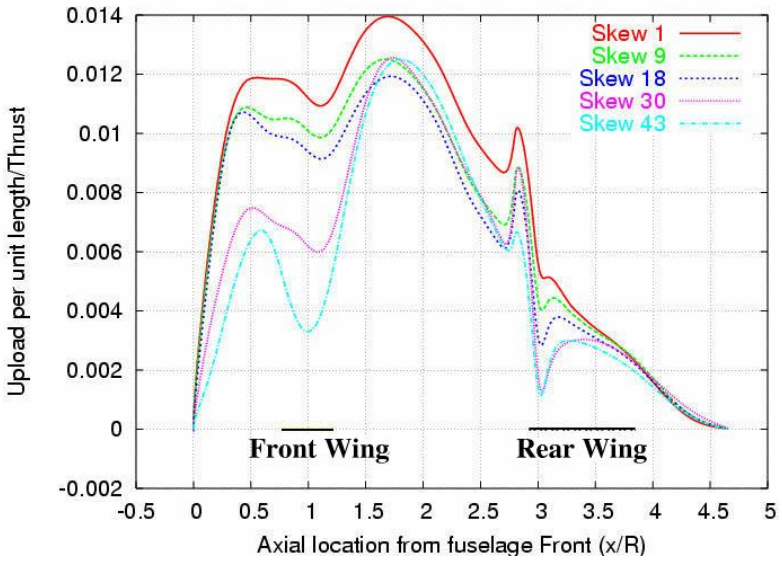

Figure 6.9: Loading on the fuselage along the longitudinal direction in forward flight (wheels on ground).

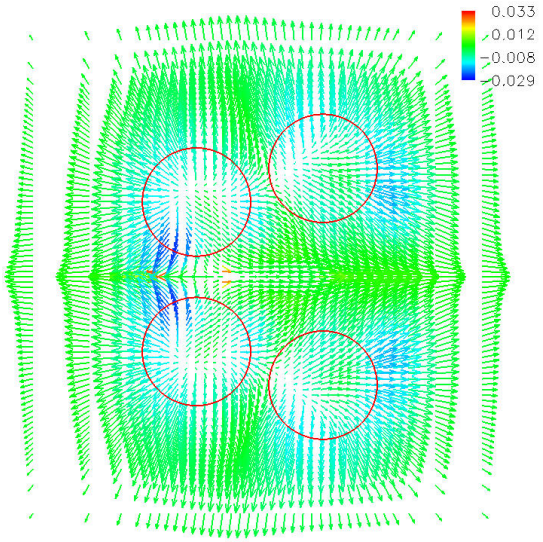

(a) Forward 1^o

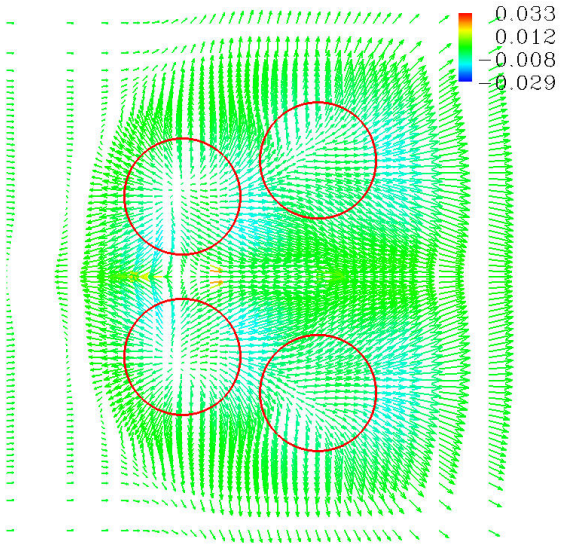

(b) Forward 18^o

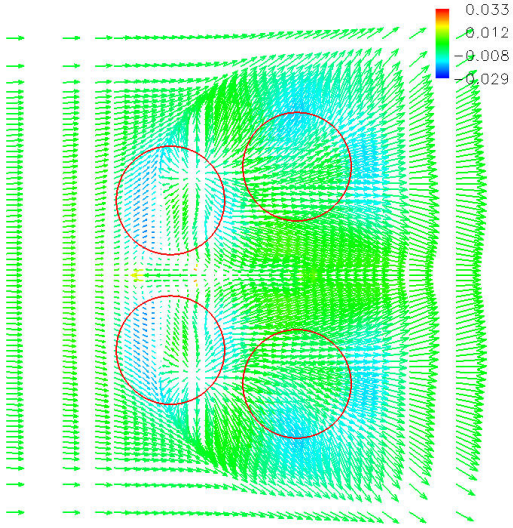

(c) Forward 43^o

Figure 6.10: Velocity vectors on a plane 2 feet above the ground in forward flight (QTR wheels on ground).

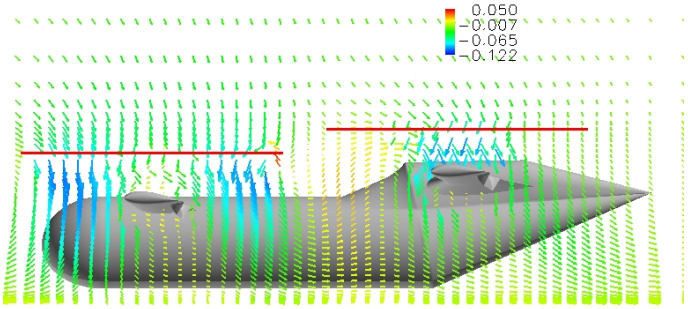

(a) Skew Angle 1^o

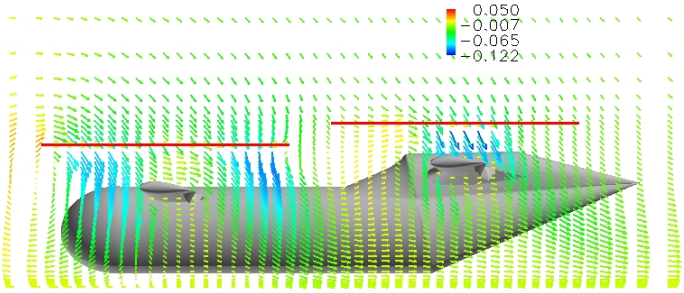

(b) Skew Angle 18^o

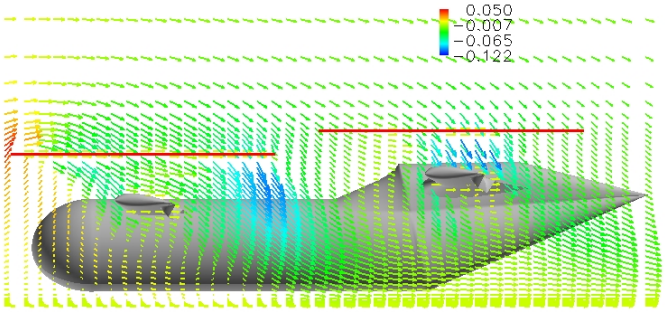

(c) Skew Angle 43^o

Figure 6.11: Velocity vectors at plane A parallel to symmetry plane in forward flight (wheels on ground).

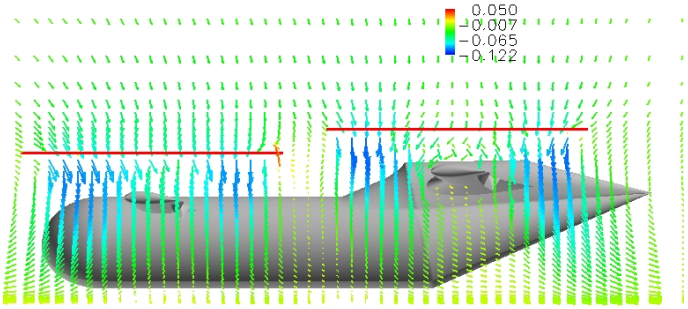

(a) Skew Angle 1^o

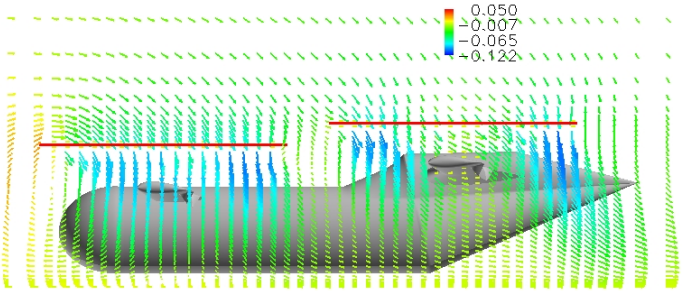

(b) Skew Angle 18^o

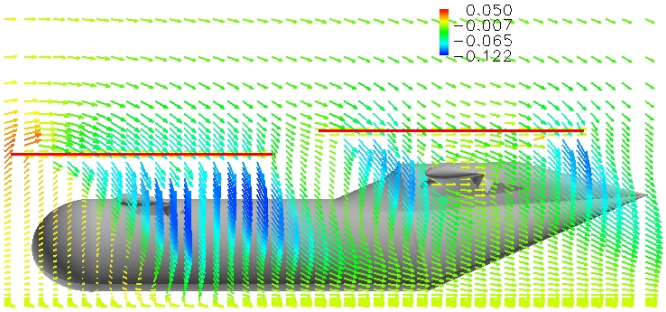

(c) Skew Angle 43^o

Figure 6.12: Velocity vectors at plane B parallel to symmetry plane in forward flight (wheels on ground).

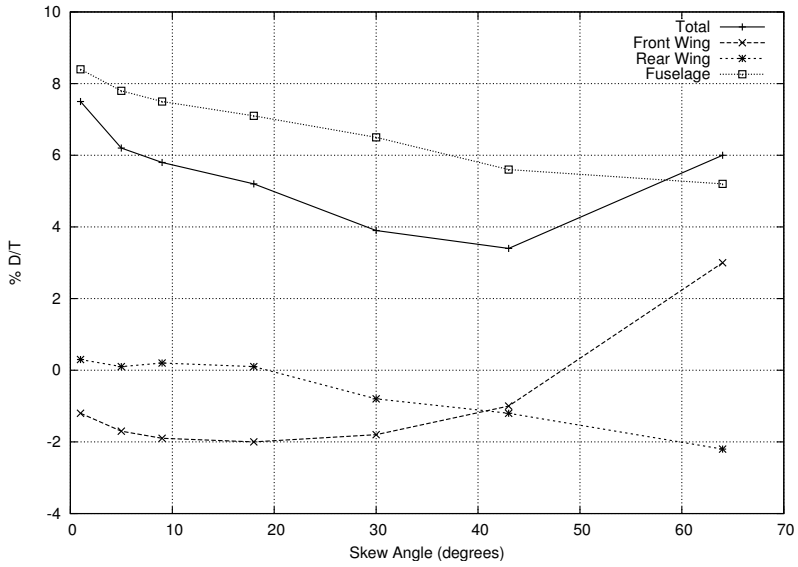

Figure 6.13: Integrated loading on the QTR as a percentage of the total thrust at various skew angles (wheels on ground).

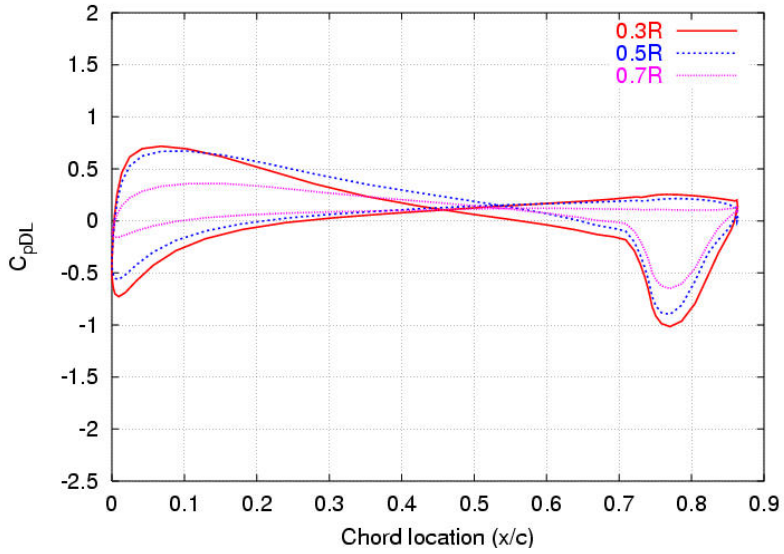

(a) Front Wing

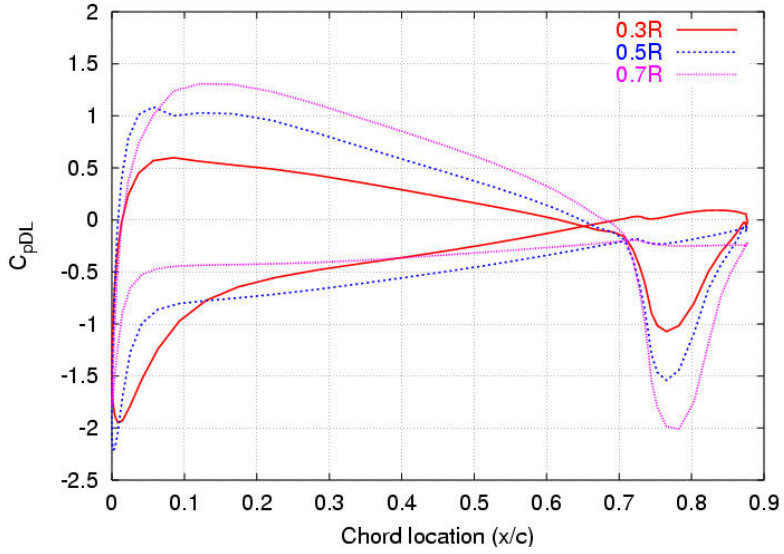

(b) Rear Wing

Figure 6.14: Pressure distribution at three span wise locations at maximum forward speed (wheels 10 feet off the ground).

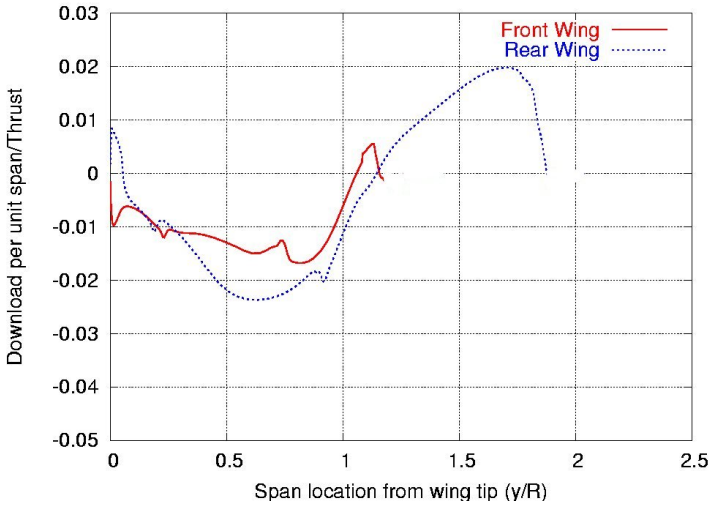

Figure 6.15: Span wise distribution of download on the wings from the wing tip at maximum forward speed (wheels 10 feet off the ground).

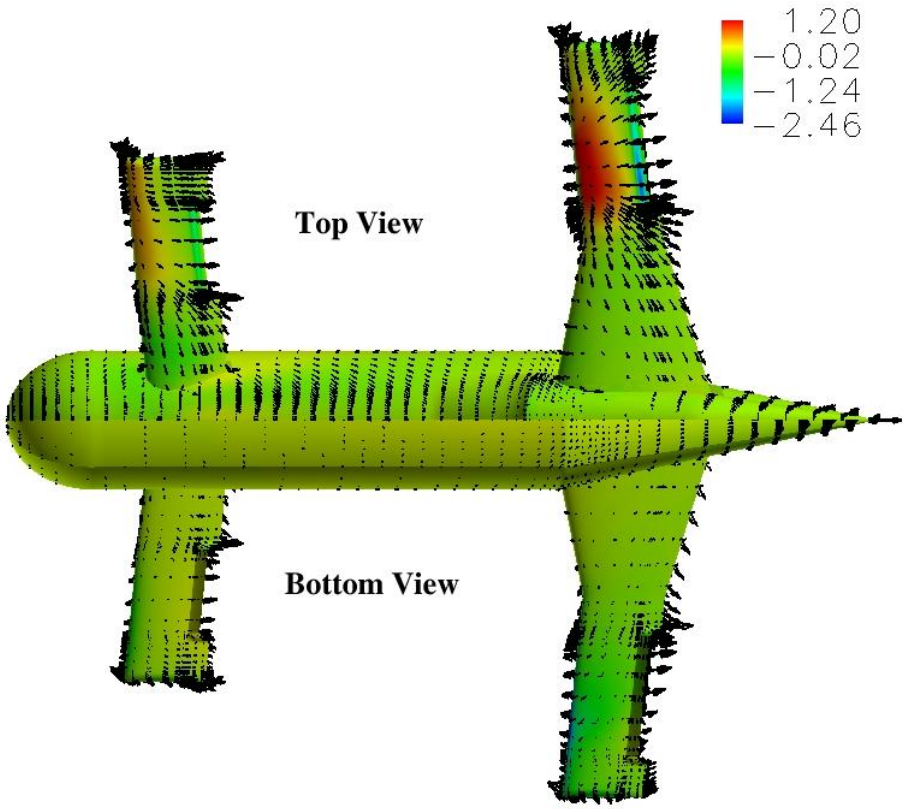

Figure 6.16: Velocity vectors at a small height above the surface along with C_{pDL} distribution (wheels 10 feet off the ground).

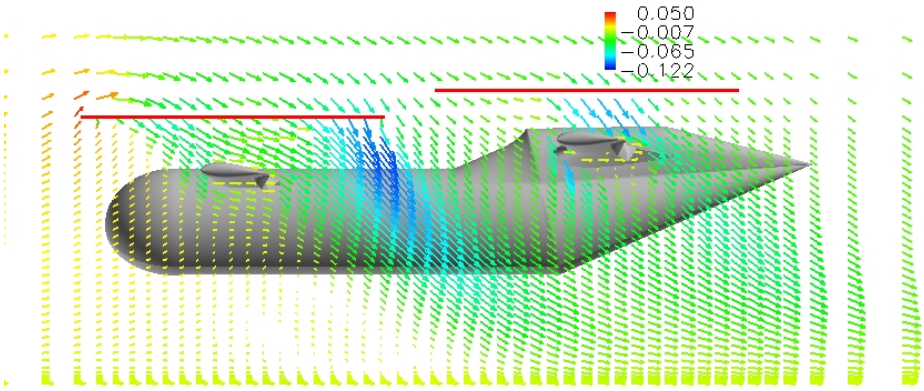

(a) Plane A

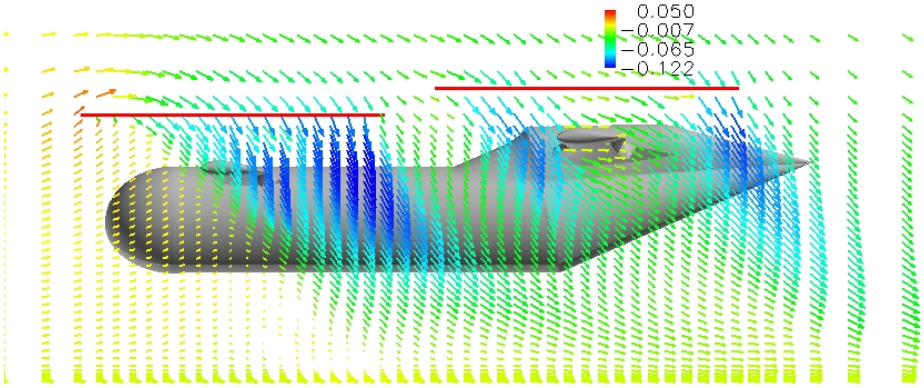

(b) Plane B

Figure 6.17: Velocity vectors at planes parallel to the symmetry plane (wheels 10 feet off the ground; Maximum Forward Speed).

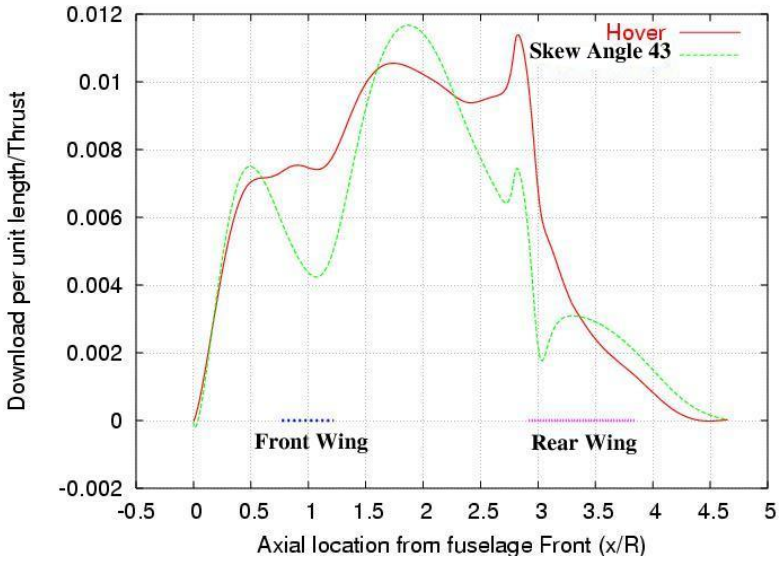

Figure 6.18: Longitudinal distribution of forces on the fuselage (wheels 10 feet off the ground; Forward Flight).

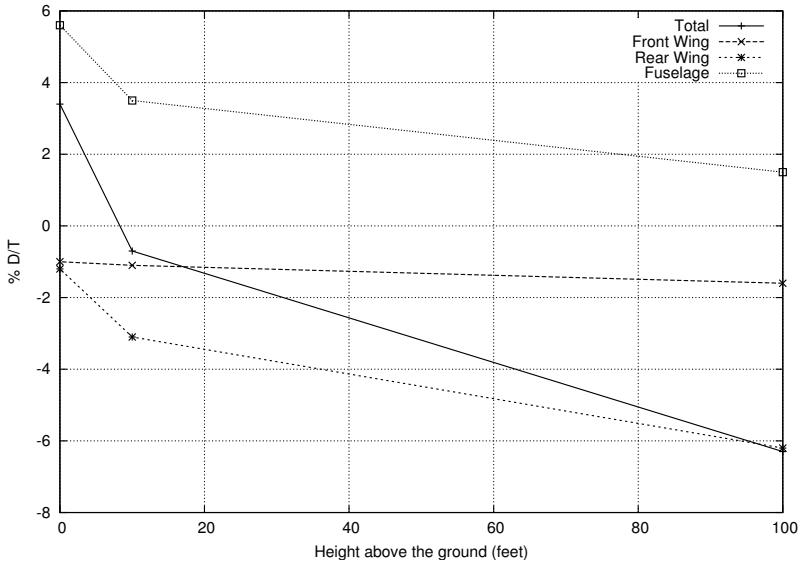

Figure 6.19: Integrated loads on the QTR in forward flight (Skew 43 degrees).

Chapter 7

Comparison with Experiment

An experimental investigation was initiated at the University of Maryland in parallel with this computational work, aiming to measure the forces on a small scale Quad Tilt Rotor (QTR) model. This combination of an experimental study with the computational work builds confidence in the combined effort in understanding the evolution of forces for various flight conditions. The experiment provides a good estimate of the forces on the QTR, where as the computational work along with estimating the loads, helps in understanding the flow patterns which lead to the changes in forces on various components of the QTR.

7.1 Experimental Setup

The experimental setup employed to measure the forces on the QTR in various flight conditions was designed by Radhakrishnan and Schmitz [19]. The labeled experimental setup is shown in Figure 7.1. The model is mounted on a frame whose height can be adjusted to model different heights of the QTR from the ground. The model is connected to the frame by two mounts. The mounts are equipped with load cells to measure the tension in the connecting rods and hence measure the vertical force on the model. The test setup is pushed by a golf cart to model forward flight of the QTR. The QTR model employed in the experiment is shown in Figure 7.2. The model is 1:31 scaled model of the QTR. Prop-rotors are used instead of the rotors from the QTR. These prop-rotors are shown to generate a sim-

ilar downwash distribution as the V-22 rotor. These prop-rotors are constant pitch rotors, hence the only method of controlling the thrust is by modifying the tip speed. To better understand this, thrust of a rotor can be mathematically expressed as the following.

$$T = \rho C_T A V_{tip}^2 \tag{7.1}$$

where C_T is the thrust coefficient and is a function of collective pitch, A is the area of the rotor disk, V_{tip} is the tip speed and ρ is the density of the fluid.

In a pitch controlled mechanism, the collective pitch of the rotor is varied to vary the thrust coefficient (C_T), which modifies the thrust of the rotor (V_{tip} is held constant). On the contrary, the tip speed of the rotor is iterated in the tip speed controlled mechanism until a constant thrust is attained for all flight conditions. In the tip speed controlled mechanism, the rotor operates at different thrust coefficients (C_T) in different flight conditions. Tip speed controlled mechanism was included in the rotor model to compare the results with experiment.

The thrust of all the rotors is maintained at 5 pounds for all the cases. Thrust level of 5 pounds corresponds to a thrust coefficient of 0.014 and a tip speed of 412 feet/second for the isolated prop-rotor in hover OGE. The thrust levels correspond to a disk loading of 4.68 pounds per sq. foot. The disk loading for the full scale QTR are approximately 22 pounds per sq. foot. This difference in disk loading can lead to some differences in download prediction between the full scale and small scale (seen by McVeigh [17] for V-22).

7.2 Computational Modeling Comparison

Efforts were made to simulate the experimental settings using the computational framework. The geometry was scaled by ratio of 1:31 to model the small scale experimental model. The geometry modeled for computations (shown in Figure 4.1)was similar to the experimental model as shown in Figure 7.2, but was not a replica of the experimental model. The airfoil section used for the wings (A821201) is the same as that on the wings of the experimental model. The dimensions of the wings are also maintained to be same as the experimental

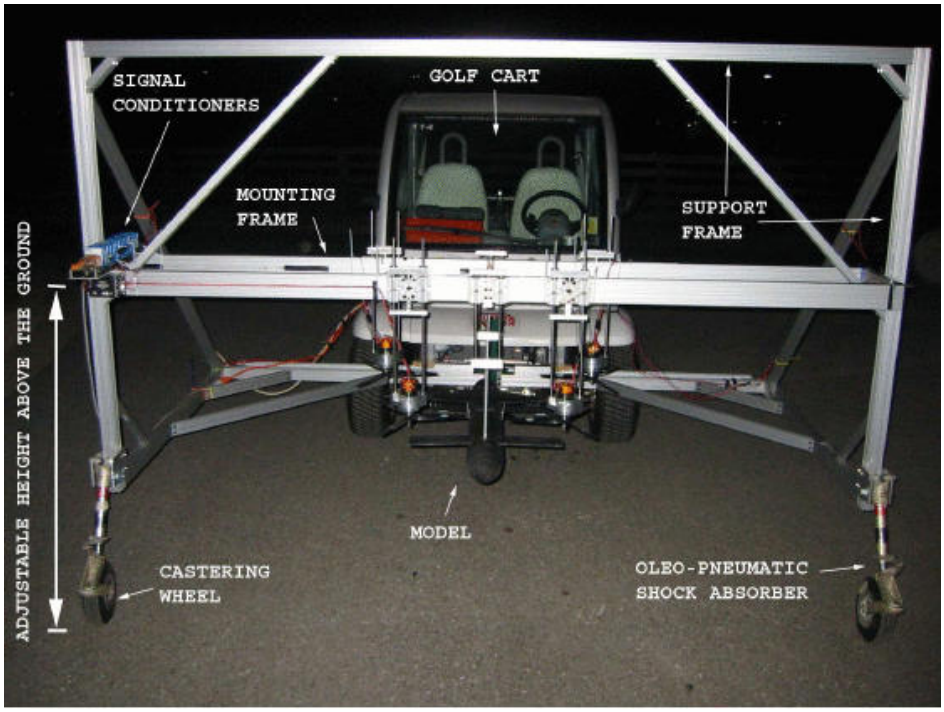

Figure 7.1: UM QTR model test setup [20].

Figure 7.2: QTR model [20].

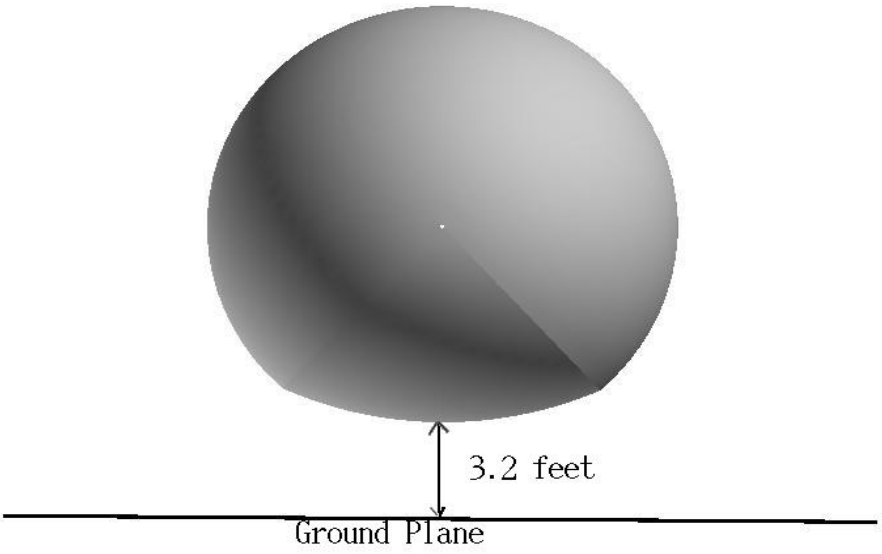

Figure 7.3: Fuselage cross-section and distance from the ground.

model. A few simplifications were made in the geometry of the fuselage. The cross-section of the fuselage along with the distance of the lowest point on the fuselage from the ground is shown in Figure 7.3. The distance of 3.2 feet between the fuselage and the ground corresponds to the full scale geometry. The distance of the fuselage from the ground was 2.2 feet. These differences in the geometry of the fuselage and its height from the ground can lead to differences in download for IGE operation.

The twist and chord distribution of the rotor blades was measured and was included in the computations. A tip speed controlled mechanism was also introduced in the computational framework. The rotor thrust was iterated in each run to achieve a constant thrust of 5 pounds by means of tip speed adjustment. No cyclic pitch was applied for these cases.

7.3 Download Distribution

A few flight conditions for the experiment model are simulated and a comparison is made with the experimental results. This comparison of download with experiment will not only build confidence in the solution algorithm , but also highlight the differences between the

full scale and small scale results.

The out of ground effect condition and wheels on the ground condition are simulated for three forward speeds 0.32, 5.95 and 13.2 knots ($\chi = 1^o$, 18^o and 36^o, respectively) and the results are compared with experiment. The download distribution over the wings for OGE operation is plotted in Figure 7.4. The distribution is plotted from the wing tip, therefore the rotor lies over the wing between the span locations 0 and 1 and the rotor downwash affects that region the most. The download on the front wing is observed to decrease with forward speed, because the front wing starts producing lift at forward speeds, especially at the in-board locations. At the fastest speed, the in-board portion of the wing beyond 0.7 R from the wing tip experiences an upward force. The forcing on the rear wing does not vary much with forward speed for the in-board locations beyond 0.2 R from the wing tip. The rear wing is at 0 degree angle of attack and does not produce any lift. Download is observed to increase very rapidly with forward speed close to the wing tip.

The span wise download distribution on the wings for the QTR operating IGE is plotted in Figure 7.5. The in-board portion of both wings experience an upward force similar to the full scale model. The upload on the in-board locations balances the download on the out-board locations. The variation in loading on the wings with forward speed is very little, since the loads experienced by the wings are very small for IGE operation.

7.4 Download Comparison

The download measured in the experiment and that obtained computationally are tabulated in Table 7.1. The download on the aircraft measured experimentally for OGE operation matches very well with the computational results (within 6%). The results for the IGE operation obtained computationally are very different from the experimental values (within 60%). There are several reasons which could cause this difference. The geometrical differences in the fuselage will contribute to these differences. Effect of the fuselage shape is very significant in wheels on the ground operation of the QTR. The stagnated flow pattern

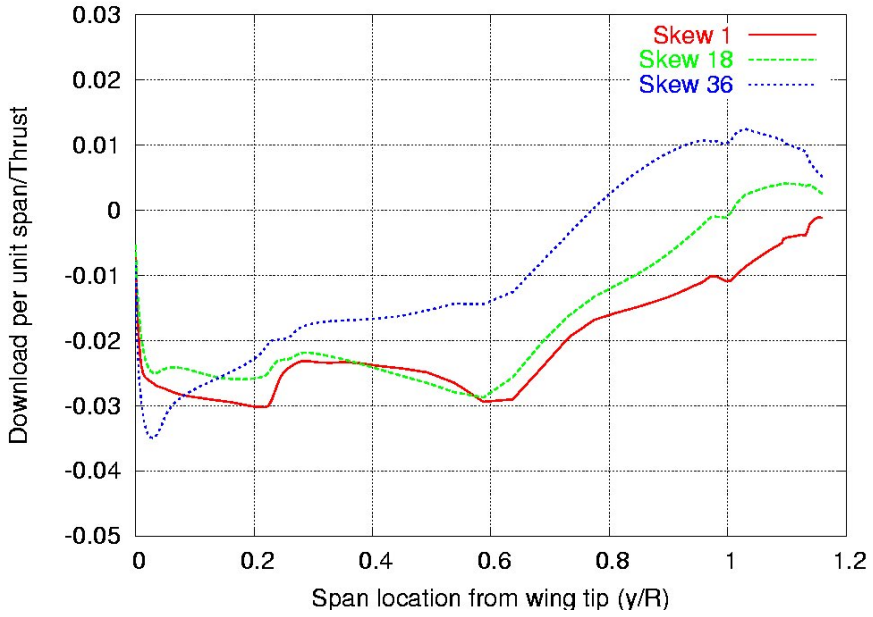

(a) Front Wing

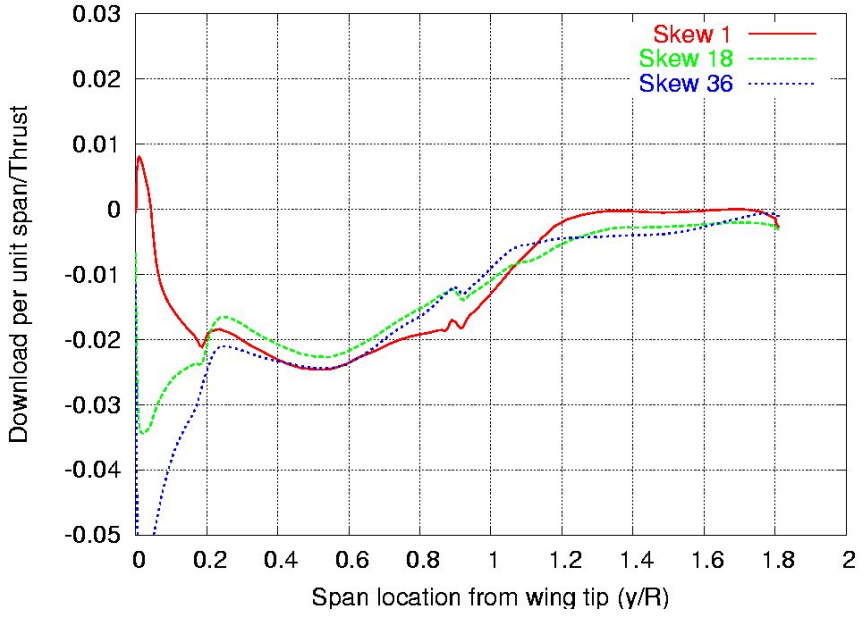

(b) Rear Wing

Figure 7.4: Span wise distribution of force on the wings for the small scale model (OGE).

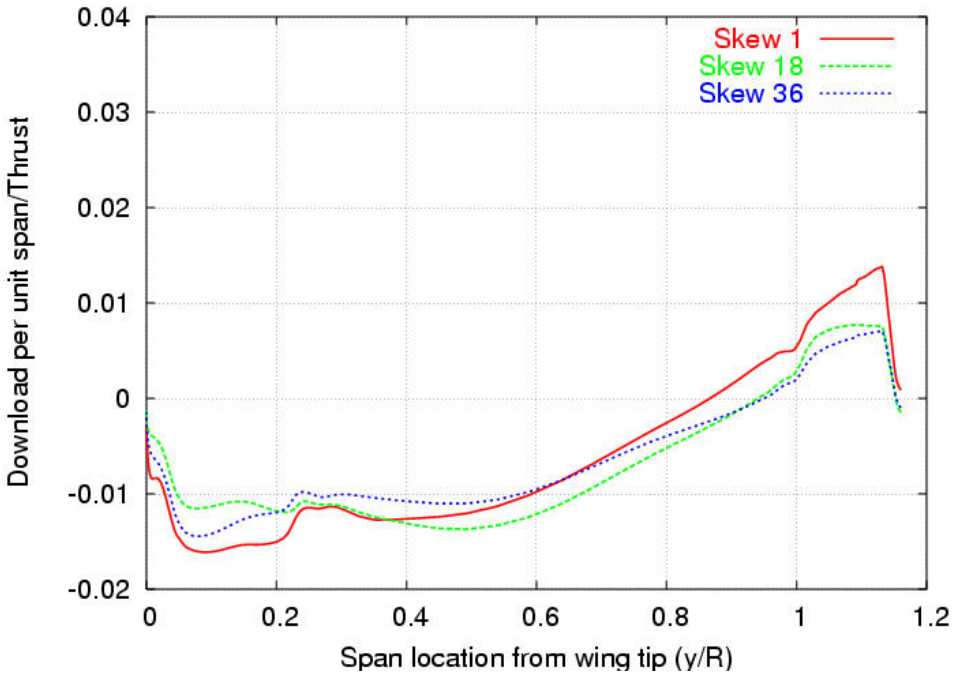

(a) Front Wing

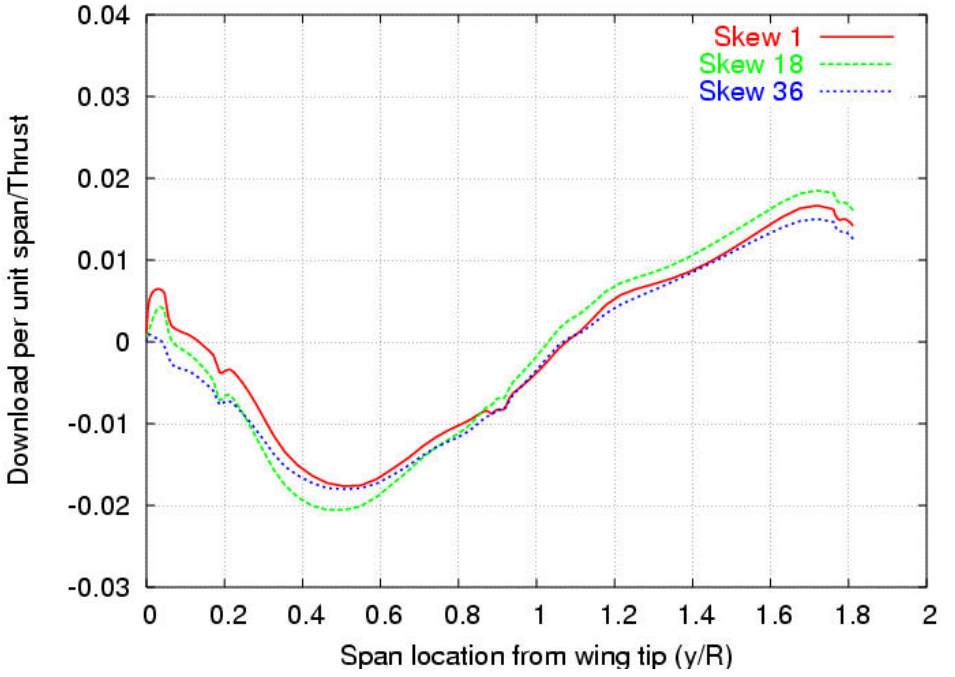

(b) Rear Wing

Figure 7.5: Span wise distribution of force on the wings for the small scale model (IGE).

Table 7.1: Loads as a percentage of thrust comparison for the QTR with experiment.

Condition	Front Wing	Rear Wing	Fuselage	Total	Experiment	Difference
OGE						
$\chi = 1^o$	-5.2	-4.6	0.3	-9.6	-9.0	0.6
$\chi = 18^o$	-4.2	-5.1	0.8	-8.5	-7.9	0.6
$\chi = 36^o$	-2.1	-5.9	1.7	-6.2	-6.4	0.2
IGE						
$\chi = 1^o$	-1.6	-0.2	6.8	5.0	8.8	3.8
$\chi = 18^o$	-1.8	-0.3	6.8	4.6	9.2	4.6
$\chi = 36^o$	-1.7	-0.8	5.8	3.3	7.5	4.2

below the fuselage is dependent on the fuselage shape and its distance from the ground. The stagnated flow pattern determines the upload experienced by the fuselage, as a result modifies the integrated load on the QTR. The computational algorithm with the turbulence model was only validated for OGE rotor-wing interaction, there might be some inherent limitations of the turbulence model in modeling ground effect operation. A combination of aforementioned factors can cause these differences for IGE operation.

The computational results obtained for the small scale model with the V-22 rotors replaced by prop-rotor are not very different from computational results obtained for the full scale model. These small differences between the loading on the small scale model and the full scale justify the employment of the small scale model to estimate the downloads on the full scale QTR for OGE operation. The effect of Reynolds number is negligible for this problem, because the flow separation is dictated by the geometry and not by the magnitude of viscous effects. It is still essential to include the viscous effects, because flow separation is a viscous phenomenon. The presence of the wing in the rotor downwash will lead to flow separation regardless of the Reynolds number. The effect of the fuselage is very small for OGE operation.

The loading on the QTR does change for small scale with respect to the full scale for

IGE operation. Fuselage becomes an important factor in this flight regime and contributes heavily to the loading on the aircraft. Almost stagnated flow between the ground plane and the fuselage will be different in the full scale and small scale cases and can be a reason for differences in loading on the aircraft. Therefore, Reynolds number can be an important criterion for IGE operation contrary to OGE operation.

Chapter 8

Closure

Tilt rotors are uniquely configured to operate in disparate conditions, ranging from vertical take off to high speed forward flight. These advantages are combined with lots of design complexities attempting to obtain a compromise between the two modes of flight (helicopter mode and propeller mode). The complexities in the proposed design of the Quad Tilt Rotor (QTR) are further enhanced by inclusion of an additional wing and two more rotors at its tip for higher payload capabilities.

The desire for high payload capability is partly foiled by the high download on the wings because of the rotor downwash impingement on the wings. There is a need for accurate prediction of this download in order to demonstrate the capabilities of this new vehicle, QTR. In this work, accurate prediction of downloads is attempted and flow features are analyzed to understand the reasons for this high download or changes in loads for different flight conditions.

Accurate prediction of download requires a sufficiently detailed grid in order to predict the complex flow field around the QTR. Chosen methodology was an amalgamation of two methodologies, which were employed in the past by other researchers. One technique provided a fast, but not-so-accurate engineering solution, whereas the other technique is highly accurate, but very time consuming and is a more scientific approach than an engineering approach. Assets of both techniques are borrowed and the resulting hybrid methodology is sufficiently accurate and a order of magnitude faster than the scientific approach. In the present

work, stationary components were modeled by employing the overset mesh technique, which involves modeling of different components of the geometry by different structured meshes and developing metrics for communication between the meshes. The rotor is approximated by body forces which are added to the Reynolds Averaged Navier-Stokes equations across the rotor plane to account for the induced velocity and swirl added to the flow across the rotor. This feature is borrowed from the engineering approach. Blade element theory is coupled with CFD to simulate the effect of the rotor flow field.

Another important feature of the current methodology is the inclusion of Low Mach number Preconditioning. The flow field around the wing involves very low velocities and adopting a compressible solver leads to slow convergence along with inaccuracies because of inappropriately high dissipation. Hence, low Mach number Preconditioning by Turkel is incorporated in the compressible solver to obtain accurate solutions at a faster turn around time.

The methodology developed is verified by simulating flow around two dimensional airfoils at low Mach numbers. Benefits in terms of accuracy and speed are realized by this practice. A model problem of rotor-wing interaction is simulated to investigate the effectiveness of the preconditioned algorithm and to assess the free stream velocity sufficient to model hovering flight. A free stream velocity of 2-3 % of the rotor induced velocity is shown to be sufficiently small to approximate hover (free stream velocity of 0). A rotor-wing interaction is simulated for this free stream velocity, but approaching the rotor-wing combination from different directions. The change in the loading of the wing is observed to be small (0.5% of the total thrust), when the direction of this free stream velocity is modified from a vertical direction to a horizontal direction (from climbing flight to forward flight). This negligible difference assured that the free stream velocity is sufficiently small to model hover.

To analyze the accuracy of the algorithm, an isolated rotor is simulated using the rotor model and the lift distribution and velocity distribution below the rotor are compared with experiment. Some differences between the computational and experimental results in the tip loading are observed, but the velocity distribution matches very well with the experimental results. The rotor installed at the tip of a wing is simulated and the pressure distribution at

four spanwise locations is compared with experiment. A reasonable agreement with experiment is obtained laying the fore ground for approaching the download prediction problem for the QTR.

In this work, the helicopter mode of the QTR is investigated. Several flight conditions, involving In Ground Effect (IGE) and Out of Ground Effect (OGE) operation, are simulated. Initially hovering conditions for OGE, wheels 10 feet off the ground and on the ground operation are simulated. High download observed OGE transformed into a strong upload on the aircraft IGE. The wings which bear most of the download OGE, experience negligible loads IGE and the fuselage which experiences negligible load OGE, experiences the maximum load IGE. This high upload IGE raises hopes for an increase in the payload capability of the aircraft, and high lifting capability was the driving force for the initiation of the QTR design.

Slow forward flight is simulated OGE and IGE in order to analyze the effect of forward speed on loading on the QTR. For OGE operation, the flow through the front rotor starts skewing with forward speed, this skewing of the flow modifies the angle at which the flow impinges on the front wing surface. The subsequent reduction in the incidence angle reduces the download with forward speed. Similar results are obtained for the V-22. Although the download on the front wing reduces with forward speed, the download on the rear wing increases with forward speed. This increase in download on the rear wing makes the drop in download of the QTR much smaller, when compared with the V-22. This increase in the download on the rear wing can be explained with more certainty by looking at the velocity vectors in the proximity of the rear wing. The velocity vectors reveal that the front rotor shields the rear rotor from the free stream velocity. This shielding reduces the skewness of the flow through the rear rotor. The wake of the front rotor also influences the flow below the rear wing. Higher velocities are observed below the rear wing for high forward speed cases, which lead to lower pressures and higher downloads. Hence, the download on the rear wing does not increase by impingement of the downwash from the front rotor, but indirectly by means of the shielding mechanism explained previously.

An experimental investigation was initiated at the University of Maryland to provide a measure of the download on a small scale QTR model (1:31) in different flight conditions. This small scale model of the QTR is simulated by modifying the Reynolds number of the flow and redefining the rotor parameters, since the rotors used in the experiment are different from those on the proposed full scale QTR. A tip speed control loop is included, instead of collective control to maintain constant thrust produced by the rotors. The results of the computational study match fairly well (within 6%) for OGE operation, but large differences (upto 60%) are observed for IGE operation. The reasons for these differences can be attributed to the geometrical differences in the shape of the fuselage and also its distance from the ground. Another reason for differences could be the applicability of the turbulence model for the IGE flight regime and might lead to some errors.

Integrated loads on the QTR components are compared for hovering flight and highest forward speed (skew angle = 43^o) simulated for OGE, wheels 10 feet off the ground and on the ground conditions. The differences in loads between the wheels on the ground and OGE condition are evaluated. The biggest source of difference in the two conditions for hover is the fuselage, where as the biggest contributor for the forward flight case is the rear wing. The difference in the loads on the QTR is reduced by approximately half for the forward flight condition when compared to the hovering flight. A similar observation is made for the wheels 10 feet off the ground condition. From these observations, it can be concluded that if an appropriate flight path is chosen, which utilizes the benefits of operating close to the ground to gain forward speed and transition to OGE, once enough forward speed is gained. Such a flight path will lead to an increment of approximately 3% in the carrying capability of the aircraft. This increase in the lifting capability will yield an approximately 8% increase in the payload capability of the QTR. Further increase in payload capability is possible, if the nacelles are tilted forward close to the ground at higher speeds.

Chapter 9

Future Work

In the current work, sufficient details of the QTR geometry are modeled, yet there is a possibility to improve the geometry. This involves inclusion of nacelles on which the rotors are mounted, generation of air gaps between the wing and flaps and a better definition of the fuselage. Higher forward speeds should be modeled for both OGE and IGE operation with nacelles tilted forward for generation of propulsive force. The QTR is simulated only for 3 heights above the ground, more intermediate conditions should be simulated for getting a better pattern. More conditions for the small scale QTR should be simulated to better understand the discrepancies IGE. If airfoil data for the rotor blades is available that information can be included in the rotor model to more accurately predict the lift distribution over the rotor blades.

Appendix A

Modeling of Viscous Terms

Viscous effects are very significant in separated flows and dictate the point of separation. Accurate modeling of boundary layer requires accurate approximation of viscous terms. The viscous terms are essentially a combination of second derivatives of velocity multiplied by the viscosity. When the two derivative are not along the same directions, the terms are called cross terms. A generalized expression for viscous terms can be written as:

$$\frac{\partial}{\partial x_j}(\mu \frac{\partial u}{\partial x_k}) \tag{A.1}$$

If x_j is not the same x_k, the terms are called cross terms, else parallel terms. In a thin layer assumption, the cross terms are ignored, that leaves only three parallel terms in the formulation. The viscous terms are dissipative in nature, hence central differencing is used to model these terms. They can be evaluated as :

$$\frac{1}{\Delta x_j}([\mu_{j+1/2}\frac{u_{k+1}-u_k}{\Delta x_k}] - [\mu_{j-1/2}\frac{u_k - u_{k-1}}{\Delta x_k}]) \tag{A.2}$$

where

$$\mu_{j+1/2} = \frac{\mu_j + \mu_{j+1}}{2} \tag{A.3}$$

In the current work, the cross derivatives are also included, since for separated flows they are very important. The contribution from the viscous terms becomes more significant for the low Reynolds number small scale cases.

Appendix B

Simulation of the V-22

The V-22 is modeled by scaling down dimensions of the fuselage of the QTR. Also the rear wing and rear set rotors are removed. This reduces the number of grids to 5, namely front rotor mesh, front wing mesh, fuselage mesh, front collar mesh and the Cartesian background mesh. This reduces the number of grid points to 4.3 million and along with that a large reduction in computational resources.

B.1 Hovering flight of the V22

Hovering flight for the V-22 is modeled both Out of Ground Effect and In Ground Effect. The modeling of the V-22 in these two modes of flight, not only helps in understanding the differences in the flow patterns for the two flight conditions, but also illuminates the differences in the loading with respect to the QTR. Analyzing the loading on the V-22 clearly elucidates the effect of the rear wing and the rear set of rotors for the QTR. In slow forward flight in the helicopter mode of the QTR, the download on the rear wing is observed to increase with forward speed, resulting in a very shallow drop in the overall download on the QTR. The absence of the rear wing and rear set of rotors will result in a sharper drop in download for the V-22. This effect needs to be accurately quantified and well understood. The differences in the two modes of flight are presented in the next two sections for the V-22.

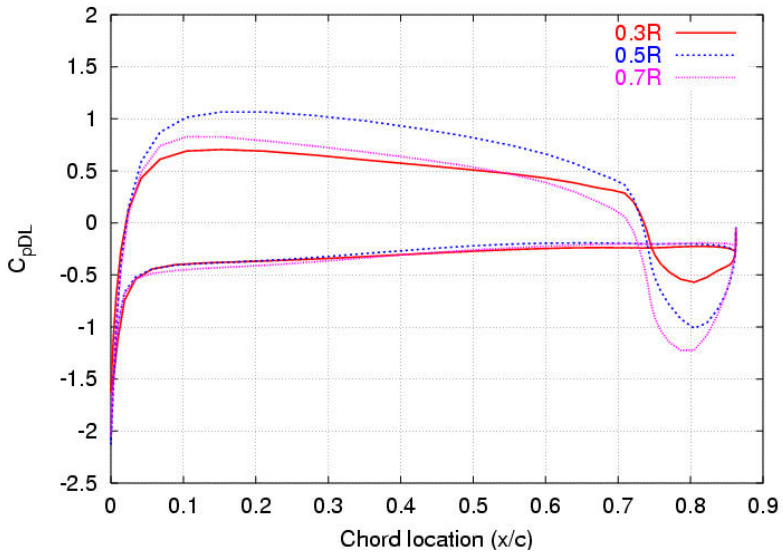

Figure B.1: C_{pDL} distribution at various spanwise locations on the wing for the V-22 in hover (OGE).

B.1.1 Out of Ground Effect

Similar to the QTR, impingement of the rotor downwash on the wing causes a download on the wing. This downward force is distributed in different ways on the wing. To elucidate the distribution, non dimensional pressure (C_{pDL}) is plotted at three spanwise locations, namely 0.3 R, 0.5 R and 0.7 R from the wing tip (rotor axis) in Figure B.1. Similar observations to those from the front wing of the QTR can be made from these pressure distributions. High negative values of C_{pDL} near the leading edge of the wing suggest rapid acceleration of flow around the leading edge. Also the constant base pressure is a clear indication of separated flow. The flaps produce an upward force and mitigate the download penalty to a certain extent. Signature of this upward force is observed at all three sections. Therefore the flap cancels some of the download produced by rest of the wing and is an extremely beneficial download reduction device. The flow features are very similar to those observed for the QTR in hover. Velocity vectors at a longitudinal plane through the wing of the V-22 are shown in Figure B.2. Fountain flow near symmetry plane is clearly evident. The two high speed streams below the rotors move towards each other. These flow patterns are very similar to

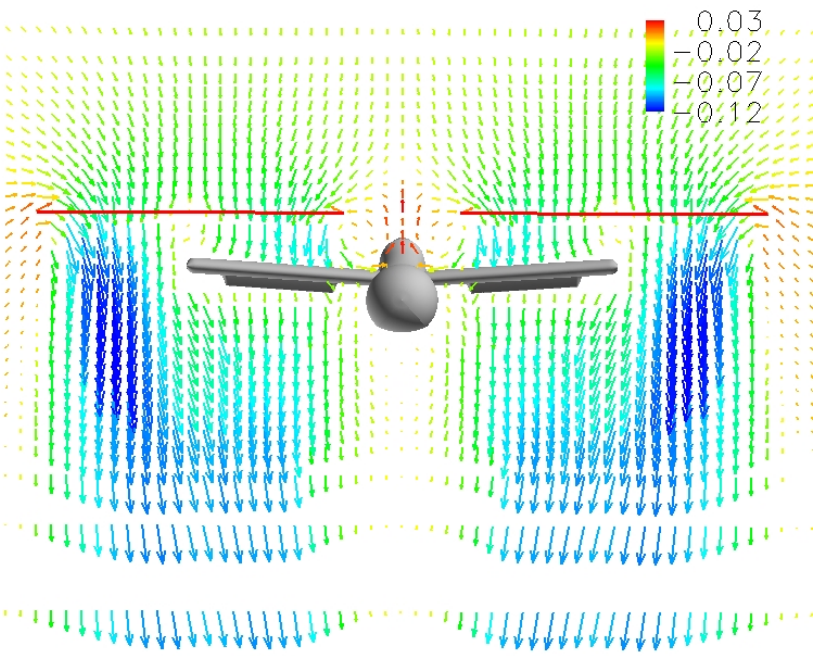

Figure B.2: locations on the wing for the V-22 in hover (OGE).

those observed for the front wing of the QTR.

B.2 In Ground Effect

Hovering flight of the V-22 is simulated and its details are presented in this subsection. Similar C_{pDL} distribution is plotted at 3 spanwise locations in Figure B.3. The base pressure for this condition is higher than the ambient pressure, which reduces the downward force at these sections. The flaps, similar to OGE, produce an upward force, further reducing the download on the wing. The area inside the curve, or in other words the download increases away from the wing tip. The download at all these sections is very small as compared to OGE operation, mostly because of the increase in base pressure. Similar mechanism for download reduction was adopted on the front wing of the QTR.

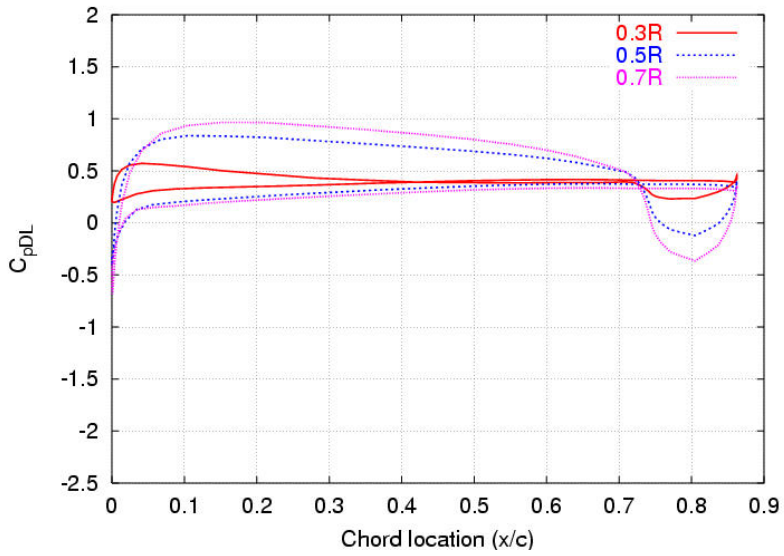

Figure B.3: C_{pDL} distribution at various spanwise locations on the wing of the V-22 in hover (IGE).

Velocity vector at a longitudinal plane through the wing are shown in Figure B.4. The comparison reveals turning of flow after it impinges the ground for IGE operation. This impingement causes an increase in pressure at the bottom of wing and the fuselage. This result is very similar to that observed for the QTR.

B.3 Forward Flight for V-22

The V-22 aircraft is simulated at a forward speed corresponding to $\chi = 43^o$. This forward speed condition corresponds to the maximum forward speed simulated for the QTR. This condition will clearly reveal the differences for the V-22 with respect to the QTR. The interaction of the front rotor wake with the rear wing prevalent for the QTR will be missing for the V-22 and hence a much lower download should be observed for this condition as a comparison to the QTR. It is necessary to simulate this condition in order to prove this hypothesis.

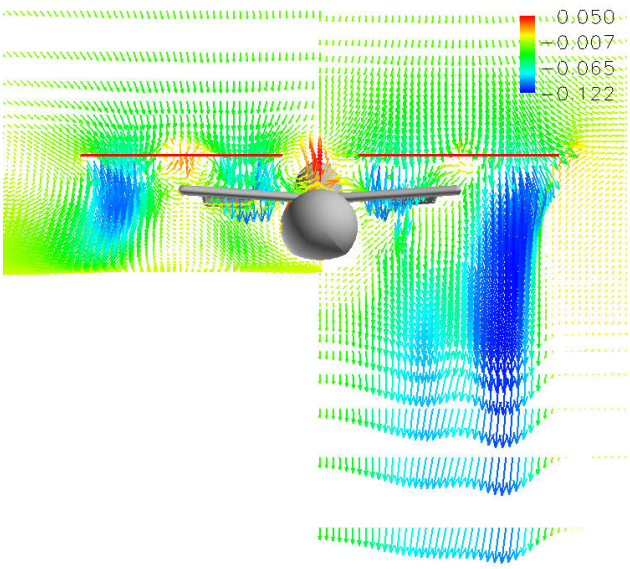

Figure B.4: Comparison of velocity vector through the wing (IGE - Left; OGE - Right)

B.3.1 Out of Ground Effect

The rotor downwash is observed to miss the wing in this condition reducing the download on the wing drastically. C_{pDL} distributions at all three spanwise locations (0.3 R, 0.5 R and 0.7 R) follow a similar pattern (Figure B.5). The flow was observed to be predominantly in the chord wise direction at these sections for all the previous cases. The forward velocity of the aircraft prevents flow separation at the leading edge of the wing. The front part of the wing experiences a download and the rear part of the wing experiences an upload, leading to a negligible download for this flight condition. The free stream velocity pushes the downwash back on the top surface of the wing, reducing the pressure in the rear section of the wing. This continuous drop in pressure on the top surface of the wing can be observed in Figure B.5. Also, a discontinuity can be observed at the location of the flap on the top surface of the wing. Velocity vectors at plane A (plane parallel to the symmetry plane) are shown in Figure B.6. The flow is almost parallel to the wing in the proximity of the wing. High downward velocity is observed behind the wing emerging from rear half of the rotor. This modification of the angle of velocity vectors emerging from the rotor plane reduces the angle

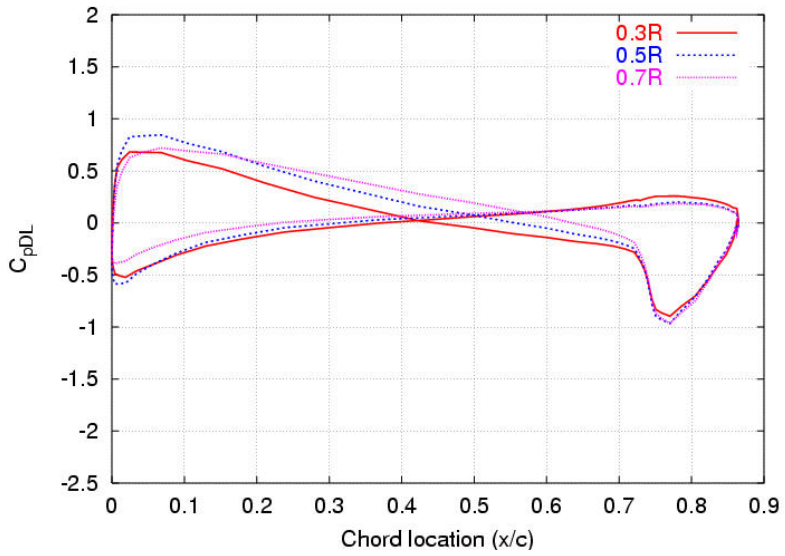

Figure B.5: C_{pDL} distribution at various spanwise locations on the wing of the V-22 in forward flight (OGE).

at which the flow impinges on the top surface of the wing, as a result reduces the pressure on the top surface, when compared with the hover condition.

B.3.2 In Ground Effect

Forward flight in ground effect is a very complex flight condition for tiltrotors. It involves the interaction of the rotor downwash not only with the wing but also with the ground. The forward speed on the aircraft pushes the stagnated flow below the fuselage backward, leading to a decrease in upload on the aircraft when compared to the hovering condition.

Non dimensional pressure distribution, shown in Figure B.7, at the same spanwise locations reveal a strong upward force on the rear half of the wing. Pressure is again observed to decrease on the top surface of the wing, suggesting skewness of the flow in the backward direction. The pressure on the lower surface increases from the leading edge to the trailing edge. Different patterns are followed at the top and bottom surfaces of the wing, leading to a cross over.

The forces on the V-22 components are integrated for the four flight conditions and tab-

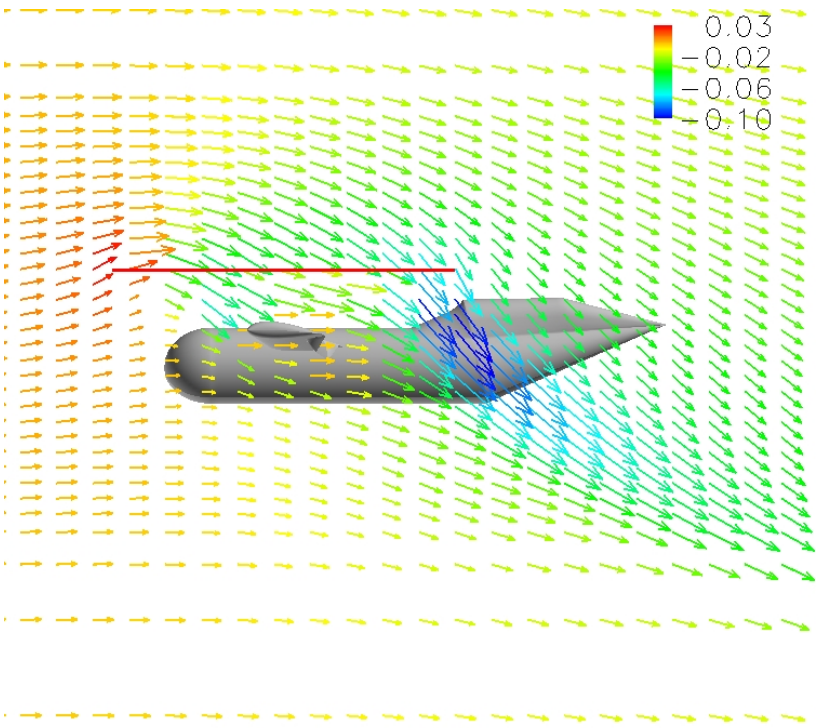

Figure B.6: locations on the wing for the V-22 in hover (OGE).

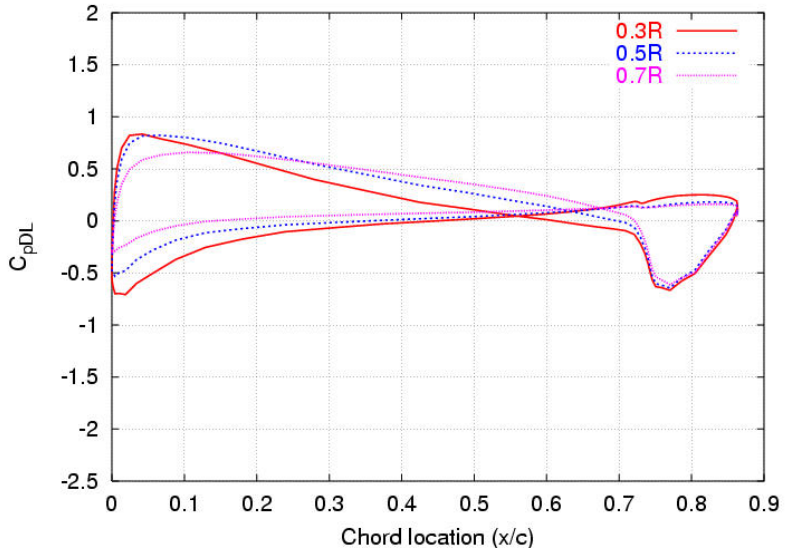

Figure B.7: C_{pDL} distribution at various spanwise locations on the wing of the V-22 in forward flight (IGE).

Table B.1: Loads comparison at hover and the highest skew angle (43^o) for the V-22.

Condition	Wing	Fuselage.	Total
Hover (IGE)	-1.4	3.6	2.2
Hover (OGE)	-9.3	0.1	-9.2
$\chi = 43^o$(IGE)	-1.9	3.9	2.0
$\chi = 43^o$(OGE)	-1.0	1.9	0.9

ulated in Table B.1. The download for the OGE hovering condition is unchanged from the QTR and the influence of the rear rotor and wing is negligible in this flight mode. V22 in hovering condition IGE experiences a much smaller upload compared to the QTR, because the fencing of flow observed in the QTR is absent in this configuration.

The effect of the rear set of rotors and wing is clearly evident in the forward flight conditions. The wake from the rotor misses the wing reducing the download drastically on it for the OGE condition. This is very different from the QTR where the wake from the front rotor never misses the front wing. The influence of the slip stream from the rear rotor prevent this from occurring.

The flow patterns in the simulate conditions are observed to very different from the QTR, except for the hovering OGE condition. The problem of simulating the QTR is much more complicated as expected. The interaction between the front set of rotors with the rear set of rotor augments the complexity of the problem and was shown in this section.

References

[1] $http://pma275.navair.navy.mil/$

[2] $http://avia.russian.ee/vertigo/bell-xv-3-r.html$

[3] $http://www.vtol.org/vertiflite/BellTiltrotors.htm$

[4] Snyder, D., "The Quad Tiltrotor: Its Beginning and Evolution," 56th American Helicopter Society, Virginia, May, 2000.

[5] Branum, L. and Tung, C., "Model Tiltrotor Hover Performance and Surface Pressure Measurement," 46th Annual AHS Forum, Washington D.C., May 1990.

[6] Yamauchi, G., Burley, C., Mercker, E., Pengel, K. and JanakiRam, R. "Flow Measurements of an Isolated Model Tiltrotor," 55th Annual AHS Forum, Monreal, Canada, May 1999.

[7] Felker, F. and Light, J., "Aerodynamic Interaction between a Rotor and Wing in Hover," 42nd AHS Annual Forum, Washington D.C., June, 1986.

[8] Felker, F., "Wing Download Results from a Test of a 0.658-Scale V-22 Rotor and Wing," 47th AHS Annual Forum, Arizona, May, 1991.

[9] Matos, C., Reddy, U., and Komerath, N., "Rotor Wake/Fixed Wing Interaction with Flap Deflection," 55th AHS Aeromechanics Specialists Meeting, Atlanta, GA, November, 2000.

[10] Funk, R., and Komerath, N., "Rotor Wake Interaction with a Lifting Surface," 51st AHS Annual Forum, Fort Worth, Texas, May, 1995.

[11] Polak, D., Rehm, W. and George, A., "Effects of an Image Plane on the Tiltrotor Fountain Flow," 2nd AHS International Aeromechanics Specialists Meeting, Connecticut, October, 1996.

[12] Woods, T. and Peryea, M., "Reduction of Tiltrotor Download," 49th AHS Annual Forum, Missouri, May, 1993.

[13] Matos, C., and Komerath, N., "Download Modification using Surface Blowing," 55th AHS Annual Forum, Montreal, Canada, May, 1999.

[14] Lee, S., "A Two Dimensional Study of Rotor/Airfoil Interaction in Hover," Joint Institute for Aeronautics and Acoustics Technical Report, No. 88, August, 1988.

[15] Felker, F., Light, J., and Faye, R., " Reduction of Tiltrotor Download using Circulation control," 55th AHS Annual Forum, Montreal, Canada, 1999.

[16] Liu, J., McVeigh, M., Mayor, R. and Snider, R., "Model and Full-Scale Tiltrotor Hover Download Tests," 55th AHS Annual Forum, Montreal, Canada, May, 1999.

[17] McVeigh, M., Grauer, W. and Paisley, D., "Rotor/Airframe Interactions on Tilt Rotor Aircraft," 44th AHS Annual Forum, Washington D.C., June, 1988.

[18] Desopper, A., Routhieau, V., Roth, G., Grunhagen, W. and Haverdings, H., "Study pf the Low Speed Characteristics of a Tiltrotor," Onera, Eurocopter, DLR, NLR, 2002.

[19] Radhakrishnan, A. and Schmitz, F., "An Experimental Investigation of a Quad Tilt Rotor in Ground Effect," 21st AIAA Applied Aerodynamics Conference, Florida, June, 2003.

[20] Radhakrishnan, A. and Schmitz, F., "An Experimental Investigation of a Quad Tilt Rotor in Low Speed Forward Flight," AHS 4th Decennial Specialist's Conference on Aeromechanics, California, January, 2004.

[21] Clark, D. and McVeigh, M., " Analysis of the Wake Dynamics of a Typical Tiltrotor Configuration in Transition Flight," 11th European Rotorcraft Forum, London, 1985.

[22] Raghavan, V., McCroskey, W., Van Dalsam, W. and Baeder, J., " Calculation of the Flow Past Bluff Bodies, Including Tiltrotor Wing Sections at α = -90 degrees," AIAA 28th Aerospace Sciences Meeting, Reno, Nevada, January, 1990.

[23] Fejtek, I. and Roberts, L., " Navier-Stokes Computation of Wing/Rotor Interaction for a Tiltrotor in Hover," AIAA 29th Aerospace Sciences Meeting, Nevada, January, 1991.

[24] Poling, D., Rosenstein, H. and Rajagopalan, G., "Use of a Navier-Stokes Code in Understanding Tiltrotor Flowfields in Hover," 52nd AHS Annual Forum, Washington D.C., June, 1996.

[25] Tai, C. and Vorwald, J., "Simulation of V-22 Rotorcraft Hover Flowfield," AIAA International Powered Lift Conference, Santa Clara, CA, December, 1993.

[26] Strawn, R. and Djomehri, M., "Computational Modeling of Hovering Rotor and Wake Aerodynamics," Journal of Aircraft, Vol. 39, 2002.

[27] Meakin, R., "Unsteady Simulation of the Viscous Flow About a V-22 Rotor and Wing in Hover," *AIAA Atmospheric Flight Mechanics Conference*, Maryland, August, 1995.

[28] Potsdam, M. and Strawn, R., "CFD Simulation of Tilt Rotor Configurations in Hover," 58th AHS Annual Forum, Montreal, Canada, June, 2002.

[29] Potsdam, M., Schaller, D., Gopalan, R. and Silva, M., "Tilt Rotor Aeromechanics Phenomena in Low Speed Flight," AHS 4th Decennial Specialist's Conference on Aeromechanics, California, January, 2004.

[30] Favier, D., Ettaouil, A. and Maresca, C., "Numerical and Experimental Investigation of Isolated Propeller Wakes in Axial Flight," Journal of Aircraft, Vol. 26, No. 9 , Sept. 1989.

[31] Witkosky, D., Lee, A. and Sullivan, J., "Aerodynamic Interaction between Propellers and Wings," Journal of Aircraft, Vol. 26, No. 9, Sept., 1989.

[32] Chiaramonte, J., Favier, D., Maresca, C. and Benneceur, S., "Aerodynamic Interaction Study of the Propeller/Wing Under Different Flow Configurations," Journal of Aircraft, Vol. 33, No. 1, Jan.-Feb., 1996.

[33] Tai, T., "Simulation and Analysis of V-22 Tiltrotor Aircraft Forward-Flight Flow-field," Journal of Aircraft, Vol. 33, No. 2, March-April, 1996.

[34] Lestari, A., Niazi, S. and Rajagopalan, R., "Preliminary Numerical Analysis of a Quad Tiltrotor Flowfield and Performance," Tiltrotor/Runway Independent Aircraft Technology and Applications Specialists Metting of the American Helicopter Society, Texas, March 2001.

[35] White, F.M., "Viscous Fluid Flow," McGraw-Hill, 1991.

[36] Baldwin, B. and Lomax, H., "Thin Layer approximation and Algebraic Model for Separated Flows," AIAA-78-257.

[37] Durbin, P., "A Reynolds Stress Model for Near Wall Turbulence," Journal of Fluid Mechanics, Vol. 249.

[38] Spalart, P. and Allmaras, S., "A One Equation Turbulence Model for Aerodynamic Flows," 30th Aerospace Sciences Meeting and Exhibit, AIAA, Reno, NV, January, 1992.

[39] Duraisamy, K., " Studies in Tip Vortex Formation, Evolution and Control," *PhD Thesis, Department of Aerospace Engineering, University of Maryland at College Park, 2005.*

[40] Pandya, S., Murman, S. and Sankaran, V., "Unsteady Computations of a jet in cross flow in ground effect," AIAA Paper Number 2003-3890.

[41] Schroeder, E., " Low Reynolds Number Validations with Computational Fluid Dynamics with Application to Micro-air Vehicles," *Masters Thesis, Department of Aerospace Engineering, University of Maryland at College Park, 2005.*

[42] Duraisamy, K. and Baeder, J., "Active Flow Control Concepts for Rotor Airfoils Using Synthetic Jets," 1st Flow Control Conference, St. Louis, Missouri, June 24-26, 2002.

[43] Anderson, W., Thomas, J. and van Leer, B., "A Comparison of Finite Volume Flux Vector Splittings for the Euler Equations," AIAA Paper 85-0122, January, 1985.

[44] Koren, B., "Upwind Schemes, Multigrid and Defect Correction for Steady Navier-Stokes Equations," *Proceedings of 11th International Conference on Numerical Methods in Fluid Dynamics*, edited by D. Dwoyer, M. Hussaini and R. Voigt, Springer-Verlag, Berlin, 1989.

[45] , Roe, P., "Approximate Riemann Solvers, Parameter Vectors, and Difference Schemes," *Journal of Computational Physics,* Vol. 43, No. 3, 1981, pp. 357-372.

[46] Steger, J. and Warming, R., " Flux Vector Splitting of the Inviscid Gasdynamic Equations with Application to Finite-Difference Methods," *Journal of Computational Physics,* Vol. 40, 1979, pp. 263-293.

[47] Van Leer, B., "Towards the Ultimate Conservative Difference Scheme," *Journal of Computational Physics,* Vol. 14, 1974, pp. 361-370.

[48] Harten, A., "High Resolution Schemes for Hyperbolic Conservation Laws," *Journal of Computational Physics,* Vol. 49, 1983, pp. 357-393.

[49] Jameson, A. and Yoon, S., "Lower-Upper Implicit Schemes with Multiple Grids for Euler Equations," *AIAA Journal*, Vol. 25, No. 7, 1987, pp. 929-935.

[50] Yoon, S. and Jameson, A., "An LU-SSOR Scheme for Euler Equations and Navier-Stokes Equations," AIAA Paper, 87-0600, January, 1987.

[51] Steger, J., "Notes on Composite Overset Grid Schemes – Chimera," Dept. Mech., Aero. and Mat. Eng., University of California, Davis, 1992.

[52] Suhs, N., Rogers, S. and Dietz, W., "Pegasus 5: An Automated Pre-processor for Overset Grid CFD," 32nd AIAA Fluid Dynamics Conference, St. Louis, MI, June, 2002.

[53] Meakin, R., "Objects X-Rays for Cutting Holes in Composite Overset Structured Grids," 15th AIAA Computational Fluid Dynamics Conference, Anaheim , CA, June, 2001.

[54] Buning, P. G. et. al, "Overflow 1.8 ," *Overflow User's Manual, Version 1.8e*, June, 1998.

[55] Benek, J., Buning, P. and Steger, J., "A 3-D CHIMERA Grid Embedding Technique," AIAA-85-1523-CP, July 1985.

[56] Steger, J., Dougherty, C. and Benek, J., "A Chimera Grid Scheme," Advances in Grid Generation, K. Ghia, and U. Ghia, eds., ASME FED-Vol.-5, June 1983.

[57] Thompson, F. J. et. al, *Handbook of Grid Generation*, CRC Press, 1999.

[58] Steger, J., "Notes on Composite Overset Grid Schemes – Chimera," Dept. Mech., Aero. and Mat. Eng., University of California, Davis, 1992.

[59] Lee, Y. and Baeder, J., "High Order Overset Method for Blade Vortex Interaction," AIAA 40th Aerospace Sciences Meeting and Exhibit, Nevada, January 2002.

[60] Chaffin, M. and Berry, J. D., "Helicopter Fuselage Aerodynamics under a Rotor by Navier-Stokes Simulation," 51st AHS Annual Forum, Texas, May, 1995.

[61] Rajagopalan, R. and Mathur, S., "Three Dimensional Analysis of a Rotor in Forward Flight," Journal of American Helicopter Society, Vol. 36, January, 1993.

[62] Nygaard, T. and Dimanlig, A., "Application of a Momentum Source Model to RAH-66 Comanche FANTAIL," AHS 4th Decennial Specialist's Conference on Aeromechanics, California, January 2004.

[63] Tadghighi, H., " Simulation of Rotor-Body Interactional Aerodynamics: An Unsteady Rotor Source Distributed Disk Model," 57th AHS Annual Forum, Washinton D.C, May, 2001.

[64] Leishman, J. G., *Principles of Helicopter Aerodynamics*, Cambridge Aerospace Press, 2000.

[65] Gupta, V., Baeder, J., "Quad Tiltrotor Aerodynamics in Ground Effect," 58th AHS Annual Forum, Montreal, June, 2002.

[66] Turkel, E., "Preconditioning Techniques in Computational Fluid Dynamics," *Annual Review Fluid Mechanics* Vol. 31, 1999, pp. 385-416.

[67] Turkel, E., "Preconditioning Techniques for Solving the Incompressible and Low Speed Compressible Equations," *Journal of Comutational Physics*, Vol. 72, October, 1987.

[68] Turkel, E., Radespiel, R. and Kroll, N., "Assessment of Preconditioning Methods for Multidimensional Aerodynamics," *Computers and Fluids*, Vol. 26, No. 6, 1997, pp. 613-635.

[69] Guillard, H. and Viozat, C., "On the Behavior of Upwind Schemes in the Low Mach Number Limit," *Computers and Fluids*, 1999.

[70] Gustaffson, B., "Unsymmetric Hyperbolic Systems and the Euler Equations at Low Mach Numbers," *Journal of Scientific Computing*, Vol. 28, 1987, pp. 123-136.

[71] Gleize, V. and Costes, M., "Low Mach-Number Preconditioning Applied to Turbulent Helicopter Fuselage Flowfield Computation," *AIAA Journal*, Vol. 41, April 2003, pp 653-662.

[72] Choi, Y. and Merkle, C., "The Application of Preconditioning to Viscous Flows," *Journal of Computational Physics*, Vol. 105, 1993, pp. 207-223.

[73] Srinivasan, G. and Baeder, J., "TURNS: A Free Wake Euler/ Navier-Stokes Numerical Method for Helicopter Rotors," *AIAA Journal*, Vol. 31 No. 5, May 1993, pp. 2371-2378.

[74] Sitaraman J., Baeder J. and Iyengar V.,, "On the Field Velocity Approach and Geometric Conservation Law for Unsteady Flow Simulations," 16th AIAA Computational Fluid Dynamics Conference, Florida, June 23-26,2003.

[75] Pulliam, T. and Chaussee, D., "A Diagonal Form of an Implicit Approximate Factorization Algorithm," *Journal of Computational Physics*, Vol. 39, 1981.

[76] Warming, R. and Beam, R., "On the Construction and Application of Implicit Factored Schemes for Conservation Laws," SIAS-AMS Proceeedings, Vol. 11, 1978m pp. 85-129.

[77] Narramore, J. C., Grauer W. K. and Farrell, M. K., "Aerodynamic Evaluation of the V-22 Osprey Wing Section," 50th AHS Annual Forum, Washington D. C., May, 1994.

[78] Gupta, V. and Baeder, J., "Investigations of Quad Tiltrotor Aerodynamics in Forward Flight using CFD," 20th Applied Aerodynamics Conference, AIAA, Missouri, June 2002.

[79] Young, L., Lillie, D., McCluer, M., Yamauchi, G. and Derby, M., "Insights into Airframe Aerodynamics and Rotor-on-Wing Interaction from a 0.25 Scale Tilt Rotor Wind Tunnel Model," AHS International Aerodynamics, Acoustics, and Test and Evaluation Specialists' Conference, California, January, 2002.

[80] Sitaraman, J. and Baeder, J., "Analysis of Quad Tiltrotor Blade Aerodynamic Loads using Coupled CFD/Free Wake Analysis," 20th Applied Aerodynamics Conference, AIAA, Missouri, June 2002.